Effective Simplified Finite Element Tire Models for Vehicle Dynamics Simulation

Yi Li

Dissertation submitted to the Faculty of the

Virginia Polytechnic Institute and State University

in partial fulfillment of the requirements for the degree of

Doctor of Philosophy

In

Mechanical Engineering

West, Robert L, Chair

Batra, Romesh C

Ferris, John B

Sandu, Corina

Taheri, Saied

July 06, 2017

Blacksburg, Virginia

Keywords:Tire Mechanics,Finite Element Method,Vehicle Dynamics

Effective Simplified Finite Element Tire Models for Vehicle Dynamics Simulation

YI LI

(ABSTRACT)

The research focuses on developing a methodology for modeling a pneumatic bias tire with the finite element method for vehicle dynamics simulation. The tire as a load-carrying member in a vehicle system deserves emphasized formulation especially for the contact patch because its representation of mechanics in the contact patch directly impacts the handling and ride performance of a vehicle. On the other hand, the load transfer from the contact patch to the wheel hub is necessary for determining the inputs to a chassis. A finite element (FE) tire model has strong capability to handle these two issues. However, the high cost of computing resources restrains its application mainly in the tire design domain. This research aims to investigate how to balance the complexity of a simplified FE tire model without diminishing its capability towards representing the load transmission for vehicle dynamics simulation.

The traditional FE tire model developed by tire suppliers usually consists of an extremely large number of elements, which makes it impossible to be included in a full-vehicle dynamics simulation. The material properties required by tire companies' FE tire models are protected. The car companies have an increasing need for a physical-based tire model to understand more about the interaction between the tire and chassis. A gap between the two sides occurs because the model used for tire design cannot directly help car companies for their purpose. All of these reasons motivate the current research to provide a solution to narrow this gap.

Other modern tire models for vehicle dynamics, e.g. FTire or TAME, require a series of full-tire tests to calibrate their model parameters, which is expensive and time-consuming. One great merit of the proposed simplified FE tire model is that determining model inputs only requires small-scale specimen tests instead of full-tire tests. Because much of the usability of a model hinges on whether its input parameters are easily determined, this feature makes the current model low cost and easily accessible in the absence of proprietary information from the tire supplier.

A Hoosier LC0 racing tire was selected as a proof of modeling concept. All modeling work was carried out using the general purpose commercial software Abaqus. The developed model was validated through static load-deflection test data together with Digital Image Correlation (DIC) data. The finite element models were further evaluated by predicting the traction/braking and cornering tire forces against Tire Test Consortium (TTC) data from the Calspan flat-track test facility. The emphasis was put on modeling techniques for the transient response due to the lack of available test data. The in-plane and out-of-plane performance of the Hoosier tire on the full-tire test data is used for model validation, not for"calibrating" the model. The agreement between model prediction and physical tests demonstrate the effectiveness of the proposed methodology.

Effective Simplified Finite Element Tire Models for Vehicle Dynamics Simulation

YI LI

(GENERAL AUDIENCE ABSTRACT)

This research aims to develop a method to build a physically-based tire model less relying on the information of products from tire providers for the purpose of vehicle dynamics simulation. The tire model is a mathematical description of the behavior of tires under various operational conditions. The model is said to be 'physically-based' if it is derived from physical laws. In contrast, if the model is termed 'semi-empirical,' it means that the model is mainly based on tire measurement data. A physically-based model usually gives more insights to and a better understanding of tire mechanics than a semi-empirical tire model. The tire as a load-carrying member in a vehicle system deserves emphasized formulation especially for the tire-road contact patch because its representation of mechanics in the contact patch directly impacts the handling and ride performance of a vehicle. Therefore, a physically-based tire model is preferred.

One kind of physically-based models are developed through the multi-body dynamics (MBD) approach. Various full tire tests are required to identify the parameters associated with the model. Since full tire tests should be conducted on professional tire test machines, the high-cost prevents many users to have a tire model of such kind. The other kind of physically-based models are developed through the finite-element method (FEM). The FEM has strong capability to describe the mechanism of tire-road contact and deformation of the tire body. Also, parameters needed by a finite element tire model are basic material properties of different components of the tire structure, which implies the possibility to acquire parameters through small-scale sample tests instead of full tire tests. However, most of FE tire models are developed for tire design with high complexity, not good for vehicle simulation.

This research made efforts to degrade the complexity of the FE tire model and tailor the FE modeling technique suitable for the purpose of vehicle simulation. In addition, the process was designed and implemented for obtaining the necessary parameters associated with the model. A Hoosier LC0 racing tire was selected as a proof of modeling concept without any tire property data provided by tire producers. This research has a practical meaning on building tire models independent of tire companies and at low cost.

Dedication

This dissertation is dedicated to my beloved parents, Xiu-chun Li and Zhi-min Song, for their all-enduring and selfless love to make me grown bravely. They stimulate my curiosity to the world and raise my patience to discover and understand it. I would never make this achievement without their continuous support.

This research work is also dedicated to my respectful advisor Professor Bob West who treats me like my father and good friend during the past five years. I will engrave his encouragement, which is quoted from Nikola Tesla, on my mind.

> **"The scientific man does not aim at an immediate result. He does not expect that his advanced ideas will be readily taken up. His work is like that of the planter – for the future. His duty is to lay the foundation for those who are to come, and point the way."**
>
> *Nikola Tesla*,
>
> *physicist, engineer and inventor*

Acknowledgments

I would like to express my sincere gratitude to my advisor Professor Bob West for his support and encouragement. His philosophy on education and attitude towards family and friends will have great influence on my remaining life. I am lucky to be his student and intimately work together for five years. He gives me the freest atmosphere to think, learn, and practice, which is a valuable pattern of education. He is always a good listener to hear my thoughts then provides constructive comments on my work.

Great thanks to my committee members, Professor Romesh Batra, Professor Saied Taheri, Professor Corina Sandu, and Professor John Ferris who helped me to build my knowledge base. I survived from two finite-element-method courses taught by Professor Brata. I learned tire and vehicle dynamics from Professor Taheri and Ferris. Professor Sandu taught me the knowledge of multi-body dynamics. They also provided me insightful suggestions and comments through several formal and informal meetings during my research.

Great thanks to FSAE Tire Test Consortium(TTC) and Calspan for the global tire force and moment data. Dr. Doug Milliken and Dr. Edward M. Kasprzak who are the director and co-director of TTC provided detailed information about their testing facility and procedure through email-based discussions back and forth.

Special thanks to Mr. Nabeel Ahsan for the enjoyable time working together and his knowledge and experience in racing vehicles shared with me. Special thanks to Mr. Hong-yu Chen for his help on acquiring viscoelastic material data.

Finally, I have to deliver my thanks to all my friends who are the essential part of my wonderful and memorable life at Blacksburg.

Contents

CONTENTS

List of Tables

List of Figures

Nomenclature

(X_E, Y_E, Z_E) Earth-Fixed Axis System

(X_T, Y_T, Z_T) Tire Axis System

(X_V, Y_V, Z_V) Vehicle Axis System

(X_W, Y_W, Z_W) Wheel Axis System

α, SA Slip angle

$\bar{\theta}$ Average surface temperature

$\bar{g}_i^P, i = 1, 2, 3, \ldots, N$ Dimensionless shear relaxation moduli in Prony series

$\boldsymbol{F}_T$ Total tire force vector

$\boldsymbol{M}_T$ Total tire moment vector

$\dot{\gamma}_{cr}$ Critical tangential slip velocity

$\dot{\gamma}_{eq}$ Equivalent slip rate/velocity (relative moving velocity between a pair of local contact spots)

LIST OF FIGURES

$\dot{\gamma}_i^v$ Tangential slip velocity or "viscous" tangential slip rate

$\epsilon_i, i = 1, 2, 3$ Nominal principal strains

γ, IA Camber/Inclination angle

γ_i^{cr} Allowable elastic tangential slip

γ_i^{el} "Elastic" tangential slip

$\hat{C}_Y$ Estimated cornering stiffness through the FE model

κ Longitudinal slip ratio

κ_s Stiffness in stick

$\lambda_i, i = 1, 2, 3$ Principal stretches

$\mathbf{C}$ Damping matrix

$\mathbf{F}^{ext}$ External applied force vector

$\mathbf{K}$ Stiffness matrix

$\mathbf{M}$ Mass matrix

$\mathbf{u}$ Nodal displacement vector

μ Friction coefficient of a local contact interface

ν Poisson's ratio

LIST OF FIGURES

Ω, ω Speed of revolution of the wheel

ω_0 Reference wheel-spin velocity

$\sigma_i, i = 1, 2, 3$ Cauthy stress on a surface normal to the i^{th} principal direction

σ_n Normal stress in a local tangential contact plane

τ_1, τ_2 Two orthogonal components of shear stress in a local tangential plane of contact interface

τ_{cr} Critical frictional shear stress

τ_{eq} Equivalent shear stress

$\tau_i^G, i = 1, 2, 3, \ldots, N$ Time constants for shear relaxation in Prony series

$C_{ij}, i, j = 0, 1, 2, 3, \ldots$ Coefficients of the polynomial strain energy potential form which could be neo-Hookean, Mooney-Rivlin, and Yeoh forms for hyperelasticity

C_Y Cornering stiffness through the test data

F_{XT} Longitudinal tire force (scalar)

F_X/F_Z Normalized longitudinal force

F_{YT} Lateral tire force (scalar)

F_Y/F_Z Normalized lateral force

LIST OF FIGURES

F_{ZT} Normal tire force (scalar)

G_0 Initial shear modulus

$I_i, i = 1, 2, 3$ The first, second, and third strain invariants

K_0 Initial bulk modulus

L Normal/vertical wheel load acting on the wheel-center

M_{XT} Overturning moment (scalar)

M_{YT} Rolling resistance moment (scalar)

M_{ZT} Aligning moment (scalar)

P Inflation pressure

R_e Effective rolling radius

R_L Loaded radius

S_X Longitudinal slip ratio defined by SAE J760-2008

SR Longitudinal slip ratio defined by Calspan

$T_i, i = 1, 2, 3$ Nominal stress on a surface normal to the i^{th} principal direction

v Translational speed of the wheel axle, or ground speed

v_0 Ground speed corresponding to a given reference wheel-spin velocity ω_0 to achieve the free-rolling condition

W Strain energy potential

Chapter 1

Introduction

1.1 Overview

This dissertation outlines the results of a research effort on developing a systematic methodology of modeling a pneumatic bias-ply tire by the finite element method (FEM) for vehicle dynamics analysis and load transfer for in-service conditions. A good tire model is an essential element in the modeling of a full vehicle. All forces acting on the chassis through a suspension system are generated from the interaction between the tire contact patch and road surface. Therefore, the characteristics and performance of a tire model will directly affect the vehicle dynamics simulation. An effective tire model defined in this work is defined as the capability of capturing the dominant mechanics associated with vehicle dynamics under different loading conditions at manageable computational cost compared to the computational cost of other vehicle sub-system models.

For the purpose of tire design, the tire construction, the contribution of different components to tire performance, and the local stress/strain state which highly relates to fatigue and wear are the primary interests. For vehicle dynamics engineering, the tire forces and moments at the wheel hub level need to be studied in terms of its reaction to various wheel motions and road interactions. The detailed FE tire model developed for tire design by tire manufactures requires a very high number of elements, which makes it impossible to be included in a full-vehicle simulation. On the other hand, vehicle companies widely adopt semi-empirical tire models which are efficient but are missing certain insights into the mechanics. There is a gap existing between tire models used for these two different purposes.

This research stems from a motivation to improve the effectiveness of a tire model

comparable to Multi-Body Dynamics (MBD) and semi-empirical models in the vehicle simulation domain. It is an attempt to minimize the gap which is stated above. The main idea inspiring this work is that because of the important role of the tire in vehicle dynamics, more computational resources should be spent on tire modeling to enhance the capability of a tire model. The detailed FE tire model can provide a more realistic description of tire mechanics. However, its complexity restricts its usage in vehicle simulation today. The research issue is how to reduce the complexity of a tire model without losing the dominant mechanics for the purpose of supporting vehicle dynamics studies. The emphasis of this research is to extend the capabilities of an FE tire model applied in the vehicle simulation domain.

The proposed methodology is exercised on an existing Hoosier LC0 racing tire to demonstrate the concept. The methodology does not rely on any tire property data provided by tire producers, thus it makes this work have a practical meaning on building tire models independent of tire companies and at low cost.

1.2 Research Motivation

The reasons mentioned below motivated this research to build an effective FE tire model with moderate scale:

- Better understanding of the tire characteristics influencing vehicle dynamic performance,
- Providing a methodology to model pneumatic bias-ply tires with low cost and acceptable accuracy compared to the existing physical-based MBD tire models for vehicle simulation, e.g. FTire and R-MODK7, which are expensive and require a series of complicated full-tire tests to calibrate the models, and
- Removing the reliance on tire properties from tire suppliers, who keep the physical properties of their products as proprietary intellectual property.

Studying the interaction between the tire and chassis is a growing demand for vehicle dynamics. "It is evident that there is a notable interaction between the vertical behavior of the tire and that of the rest of the vehicle, between transverse stiffness and cornering stiffness, and finally between vertical and lateral stiffness, because of the elasto-kinematic behavior of the suspension" [1]. Hans Dorfi from Bridgestone Americas said, "My biggest wish would be to model the full interaction between the car and tire as this would give us the best understanding of the full tire performance and how it interacts with the chassis." [2]. The demand for studying the tire and chassis as an integral unit urges the emergence of a tire model which not only represents the "full tire performance," but is also computationally efficient when integrated into a vehicle model.

The majority of chassis/suspension models are based on Multi-Body Dynamics (MBD), while a complex physical-based tire model is usually developed through FEM. It is common for MBD-type vehicle models to be implemented in ADAMS, and for FE tire models to be built in Abaqus. The cooperative simulation between ADAMS and Abaqus was an attempt to address the issue of full-vehicle simulation. The interface between ADAMS and Abaqus had been developed to enable the vehicle and tire model to be run in separate software environments, and then to communicate and transfer the results between each other at particular time steps. However, this method did not receive wide-spread adoption in the vehicle industry.

Instead, several physical-based and MBD-type tire models such as FTire, R-MODK7, and TameTire earn their places in the vehicle simulation domain compared to the long-lasting, broadly-used, semi-empirical Magic Formula tire model. Since those models are developed under the MBD framework, it is natural to include them in a MBD-type vehicle model. For example, FTire has been incorporated into ADAMS as a third-party special purpose module to facilitate full-vehicle simulation. These contemporary tire models for vehicle simulation will be reviewed in Section 2.2.

An alternative way to perform a full-vehicle simulation is within the FEM framework, but it is still a challenge to model the chassis, suspension, and tire simultaneously by FEM. The degrees-of-freedom (d.o.f) should be proportionally assigned to each vehicle subsystem. A tire model deserves the large portion of total d.o.f in a full-vehicle model because of the tire's key role in vehicle dynamics. However, a detailed FE tire model developed for the purpose of tire design is not suitable for vehicle simulation. This research aims to provide a possible solution of tire modeling for the purpose of vehicle dynamics under the FEM framework.

1.3 Research Concept

A systematic methodology of modeling an existing Hoosier LC0 tire is developed to justify the research concept. It is necessary to be aware of the available resources and constraints before any modeling work is undertaken. The tire product is given and no information is available from the tire producers. Only limited full-tire tests can be carried out at a university which commonly has no professional tire testing platform. The cost of characterizing a tire also needs to be controlled at a low level.

The model design and parameterization should be considered as a whole process. These two aspects in modeling work mutually affect each other and cannot be separately treated. Building a model via FEM relies more on small-scale and special experiments instead of large-scale full-tire tests to calibrate the model. This unique advantage of FEM makes it an ideal solution within the constraints mentioned above.

The tire modeling includes the modeling of tire structure and tire-road interaction.

The governing equations of a general rolling tire problem have the abstract form,

$$\mathbf{M}\ddot{\mathbf{u}} + \mathbf{C}\dot{\mathbf{u}} + \mathbf{K}\mathbf{u} = \mathbf{F}^{ext} \tag{1.1}$$

where $\mathbf{M}$ is the mass matrix, $\mathbf{C}$ is the damping matrix, and $\mathbf{K}$ is the stiffness matrix. The basic field variable $\mathbf{u}$ is the nodal displacement vector, then $\ddot{\mathbf{u}}, \dot{\mathbf{u}}$ become the nodal acceleration and velocity, respectively. $\mathbf{F}^{ext}$ is the external applied force vector. Equation 1.1 can be regarded as multidimensional forms of Newton's second law. The modeling problem becomes how to formulate and identify the stiffness, mass, and damping matrix. The formulation of these matrices attributes to the modeling techniques used, such as constitutive relation of materials, element type, etc, and the identification of entries of these matrices attributes to the model parameterization. Since the proposed model's response will be evaluated at the wheel hub level rather than local stress/strain state, the stiffness and mass distribution of the tire structure does not need to be so precisely described at a very local level as a detailed FE tire model. The parameterization of the model is fulfilled by functional decomposition of the different tire components based on the purpose of each component. Instead of doing full-tire characterizations, the parameters can be obtained by a series of specially designed small-scale tests of the samples cut from a tire. However, not every structural component of a tire can be extracted and directly measured, which makes the model parameterization challenging work. The model parameterization determines the model design to a certain extent.

The tire-road interaction highly depends on the property of a road. The road surface can typically be regarded as rigid on which most of the on-track racing tires normally roll. Since the test data of the rolling tire was obtained on the Calspan flat-track test facility, a portion of tire-road interaction properties are estimated based on the surface of that test platform.

A typical detailed FE tire model usually has tens of parameters related to the material properties. It is neither possible to extract so many parameters from an existing tire product nor necessary to know all of them if the objective for the model is the global response of a tire. In other words, the proposed methodology is pursuing a "minimum realization"(the term is borrowed from control engineering) of a tire system. This feature differentiates the proposed tire model from a conventional detailed FE tire model developed for tire design. In consequence, the model is computationally simplified.

With the use of a simplified FE tire model integrated into a vehicle model, more advanced issues can be explored. For example,

- The load transfer from the contact patch to the suspension and chassis can be more realistically described. The full-vehicle simulation gives us better understanding of tire behavior and highlights its role as a vehicle component.
- The loading scenario of critical structural members of the chassis can be identified, which benefits durability analysis.

- The vibration modes of the combined chassis and tire system can be simulated.
- The dynamics of the combined vehicle system can be studied.

1.4 Research Goal

The primary goal of this research is to develop a systematic methodology for modeling a pneumatic bias-ply tire with the finite element method to support a vehicle dynamics simulation. The concept will be validated by creating a nonlinear FE tire model from an existing Hoosier LC0 racing tire. This research is expected to minimize the gap between tire models used for the purpose of tire design and vehicle dynamics. This research also initiates a framework for modeling an integrated tire-suspension-chassis system (full vehicle modeling) under the framework of FEM in the public domain.

The objectives for the model design are to:

- Develop and validate the axisymmetric and full 3D models for quasi-static inflation and load-deflection response,
- Develop and validate the full 3D model for steady-state cornering (out-of-plane) and drive/braking (in-plane) response,
- Develop the full 3D model for simplified transient (constant acceleration) rolling response, and
- Develop a tire-suspension-chassis model under the framework of FEM based on the VT FSAE 2012 formula car platform.

Developing the axisymmetric model cannot be directly utilized into any vehicle simulation, but it is a necessary step as the first check on the simplest response of a tire model.

The goals for the model parameterization are to:

- Develop a method for parametric representation of the tire geometry, and
- Design experiments and processes for extracting necessary material properties to feed into the proposed FE tire model.

1.5 Research Scope

This research uses the VT FSAE 2012 formula car (Fig. 1.1) which is equipped with four Hoosier LC0 racing tires. All modeling and analysis work is subjected to this platform. The Hoosier LC0 racing tire has simple geometry and construction

with a smooth tread for a dry road surface. These features make it suitable for the concentration on mechanics and for avoiding the distraction of modeling a complex tread pattern. The size of the Hoosier LC0 tire is small and convenient for measuring and testing in our existing facilities at the university. The chassis and suspension of the vehicle are designed and fabricated by the VT FSAE team, thus the information regarding the vehicle structure is well known.

Figure 1.1: VT FSAE 2012 vehicle platform used for modeling and simulation

The scope of this research is explained through the following points:

1. The scope of the proposed tire model and its relevance to other tire models are illustrated in Fig. 1.2.

2. The validations are provided to consolidate the modeling work on the level of quasi-static and steady-state global tire response.

3. The study focuses more on modeling techniques required to support the transient tire rolling and full-vehicle simulation because transient test data were not available at the time of this research and it is difficult to acquire the transient data under operational conditions.

4. The dominant mechanics associated with each level of tire response is studied, which impacts the vehicle dynamics.

5. Initiate work on incorporating the FE tire model into a suspension and chassis finite element model.

Some notes on the research scope are as follows:

1. The tire forces are evaluated at the wheel hub level to identify the load input to the chassis. The local contact stress and body stress of the tire are not evaluated for accuracy.

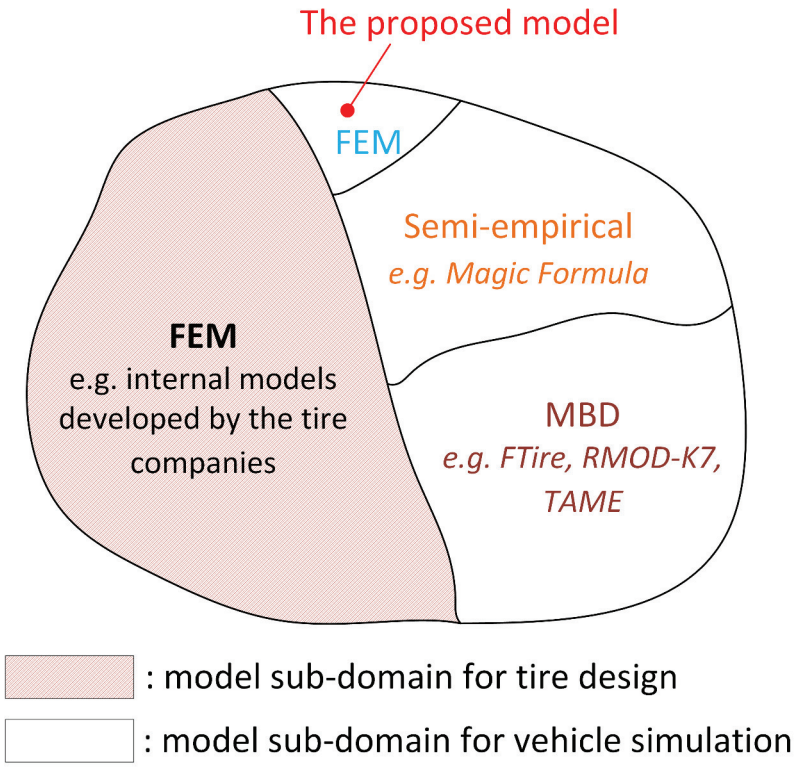

Figure 1.2: The tire model domain divided by the purpose of its usage and approach of development. The location of the proposed tire model is also labeled.

2. The tire-road interaction model influences the tire forces dramatically. The road surface is assumed to be a rigid flat surface. The interaction properties have to be estimated based on the test data of the specific surface on which the tire rolls.

3. The damping of a tire is highly associated with the time-dependent material properties of tire rubber. The testing of the viscoelasticity of Hoosier tire rubber samples had been initiated but was not completed at the time of writing this dissertation.

4. The full-vehicle model of the Formula car was built for proof of concept only. It is to demonstrate how the developed FE tire model becomes part of a full-vehicle model, but it is not ready for use in making any conclusions on a full-vehicle maneuver or ride simulation.

5. The capability of frequency prediction is determined by the mesh density for the FE tire model, given that the mass and stiffness distribution are correct. The first torsional and lateral side-to-side bending modes of the chassis are roughly

Table 1.1: Dynamic range of various tire models for vehicle simulation.

MF-SWIFT	60Hz-80Hz
FTire	up to 200Hz
RMOD-K 7	100Hz - 200Hz
TameTire	10Hz-20Hz
Simplified FE	mesh dependent

$70-80Hz$ and $80-90Hz$, respectively. It requires that the tire model can give the load excitation at the hub level no less than 100Hz for a transient response. Table 1.1 is a summary of the dynamic range of various tire models for the vehicle simulation.

The scope will NOT cover the following:

- Standing waves phenomenon on the rolling tire is not going to be included in steady-state analysis.
- Heat conduction of the tire is not going to be included in the finite element model.
- The simplified FE tire model is not going to be compared with other commercialized tire models due to the inaccessibility and extremely high cost.

The primary usage of the proposed FE tire model should be predicting dynamic forces and moments at the wheel-hub level instead of studying internal interactions among different tire components. The first priority of the modeling work is to make sure that the model represents the mechanics correctly rather than emphasizing the computational efficiency and speed.

Chapter 2

Literature Review

2.1 Background

The necessary background knowledge regarding tire and vehicle dynamics is introduced with brief comments.

2.1.1 Axis and coordinate systems

A set of axis systems are selected to provide flexibility for various modeling techniques used to represent the dynamics of vehicles as systems of multiple bodies. The axis system adopted in this work is recommended and defined by the standard SAE J760(2008) [3]. Several commonly-used axis systems are introduced below.

- "Earth-Fixed Axis System (X_E, Y_E, Z_E) is an axis system fixed in the inertial reference frame. The X_E and Y_E axes are parallel to the ground plane. The Z_E axis is aligned with the gravitational vector pointing down to the ground. The location of the origin is generally an arbitrary point defined by the user."

- "Vehicle Axis System (X_V, Y_V, Z_V) is an axis system fixed in the reference frame of the vehicle sprung mass, so that the X_V axis is substantially horizontal and points forward (with the vehicle at rest), and is parallel to the vehicle plane of symmetry. The Y_V axis is perpendicular to the vehicle plane of symmetry. The Y_V axis points to the right and the Z_V axis points downward." (See Fig. 2.1) A point fixed in the vehicle sprung mass is called a vehicle reference point. The choice of vehicle reference point is arbitrary. Commonly-used locations include the static vehicle center of gravity, the static sprung-mass center of gravity, the

mid-wheelbase point at the height of the static vehicle center of gravity, and the center of the front axle.

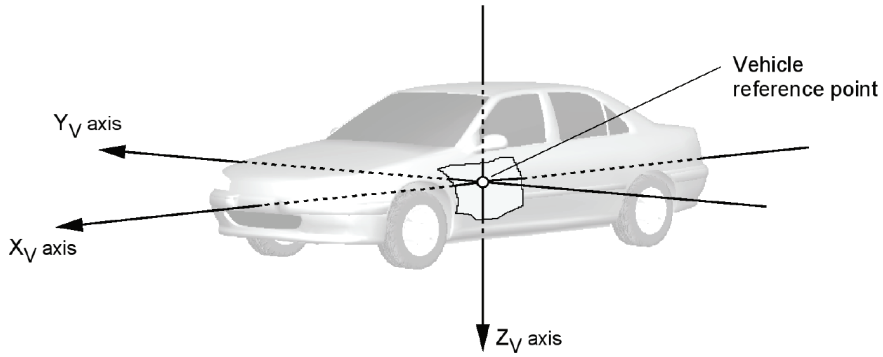

Figure 2.1: Vehicle axis system according to SAE J670. Reprinted from SAE standard J670(2008) with permission Copyright ©2008 SAE International. Further distribution of this material is not permitted without prior permission from SAE.

Before introducing the axis system for a tire/wheel assembly, some terminology should be explained first. Wheel-spin axis is the axis of wheel rotation. Wheel-plane is a plane normal to the wheel spin axis and located halfway between the rim flanges. Wheel-center is at the intersection between the wheel-spin axis and the wheel plane.

- "Wheel Axis System (X_W, Y_W, Z_W) is defined as an axis system whose X_W and Z_W axes are parallel to the wheel plane, whose Y_W axis is parallel to the wheel-spin axis, and whose X_W axis is parallel to the local road plane. The positive Z_W axis points downward. The origin of the wheel axis system is fixed at the wheel-center. A local wheel axis system may be defined for each wheel" [3]. Notice that "local road plane" instead of "ground plane" is used since "road plane" is a more local definition, which represents the road surface within each tire contact patch. For an uneven road, a different road plane may exist at each tire contact patch. The road plane for each tire/wheel assembly may or may not be parallel with the ground plane depending on whether the road surface is flat.

- "Tire Axis System (X_T, Y_T, Z_T) is an axis system in which the X_T and Y_T axes are parallel to the local road plane, with the Z_T axis normal to the local road plane (see Fig. 2.2). The orientation of the X_T axis is defined by the intersection of the wheel plane and the road plane (the intersection between the wheel plane and the road plane is also called the contact line). The positive Z_T axis points downward to the ground. The origin of the tire axis system is at the contact center which is the intersection of the contact line and the normal projection of the wheel-spin axis onto the road plane" [3]. Several comments should be made:

1) the definition of the tire axis system actually does not directly rely on a tire at all. It depends on the wheel plane, road plane, and the wheel-spin axis. 2) A contact center may not be the geometric center of a tire contact patch due to distortion of a tire produced by external forces. Thus, a contact center is instantaneous.

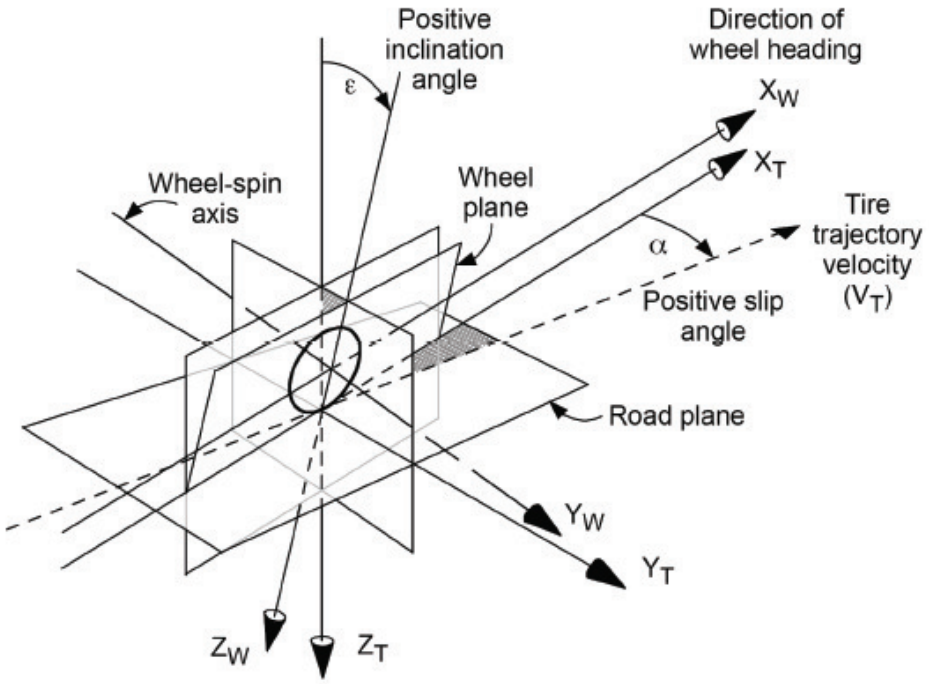

Figure 2.2: Tire and wheel axis system according to SAE J670. Reprinted from SAE standard J670(2008) with permission Copyright ©2008 SAE International. Further distribution of this material is not permitted without prior permission from SAE.

2.1.2 Inputs and outputs of a tire model

The total tire force, $\boldsymbol{F}_T$, can be defined as a vector quantity expressing the sum of the forces exerted on the tire by the road at any instant, with its line of action passing through the contact center. The longitudinal force, F_{XT}, lateral force F_{YT}, and normal load F_{ZT} are the scalar components of the total tire force projected along the tire axis direction respectively. In the same way, the total tire moment, $\boldsymbol{M}_T$, is defined as a vector quantity expressing the sum of the resultant external moments acting on the tire at any instant, consistent with the line of action of the tire force. The tire overturning moment M_{XT} , rolling resistance moment, M_{YT} (notice that it essentially has no relationship with true rolling resistance, but is easy to be misled by

its name, which is kept in use as a convention due to historical reasons), and aligning moment, M_{ZT}, are components of the total tire moment vector along the direction of X_T, Y_T, Z_T. The subscript "T" might be omitted under circumstances where only tire forces and moments are discussed. With the defined Tire and Wheel Axis System, all tire forces and moments are depicted in Fig. 2.3. Note that a negative wheel-spin velocity will induce moving forward of the wheel/tire. Following the definition, a driving torque acting on a wheel should have a negative sign. If we isolate the

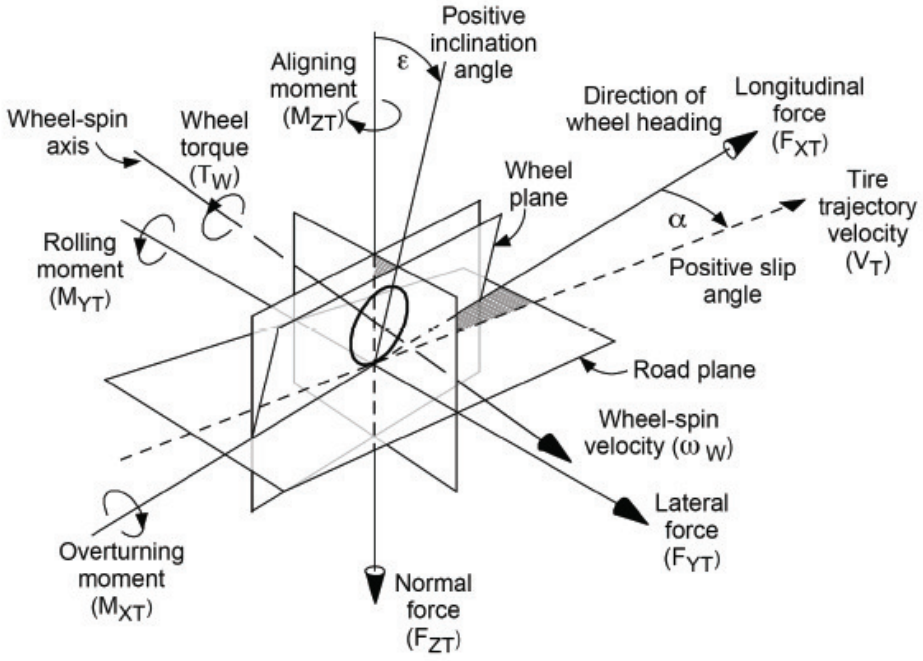

Figure 2.3: Tire force and moment nomenclature expressed in Tire and Wheel Axis System. Reprinted from SAE J670(2008) with permission Copyright ©2008 SAE International. Further distribution of this material is not permitted without prior permission from SAE.

wheel/tire assembly from the remaining components of a vehicle and treat it as an independent system, it is necessary to define the inputs and outputs for this system. The inputs stem from motions of the wheel relative to the road. Therefore, these quantities are mainly kinematic quantities, e.g. longitudinal slip ratio and lateral slip angle, etc. The tire forces and moments are considered as output quantities (see Fig. 2.4). It is common in the literature that the normal load is seen as an input and the loaded radius is treated as an output. In Fig. 2.4, the tire is assumed to be uniform and to move over a flat road surface. When the road is uneven, the height of a contact center will change and will require an additional input.

It is necessary to distinguish between in-plane and out-of-plane modes of opera-

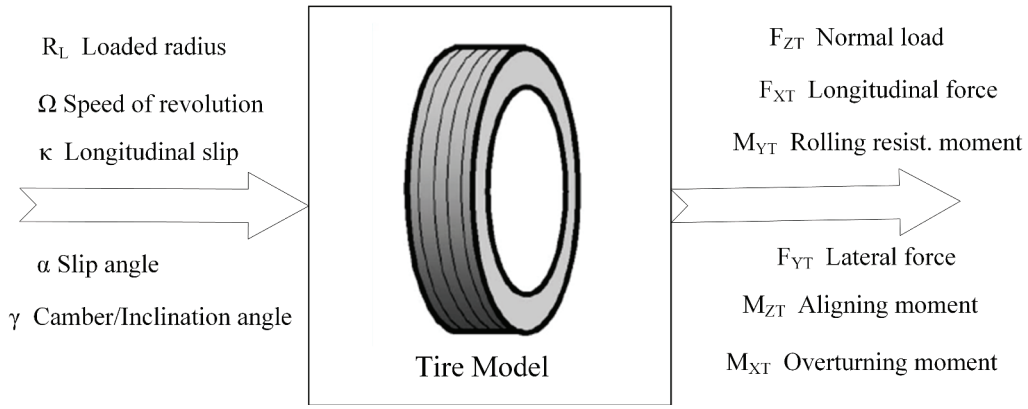

Figure 2.4: Typical inputs and outputs of a tire model (road surface considered flat)

tion. The tire is used to support the weight of the vehicle, cushion the vehicle over surface irregularities, and transmit sufficient traction and braking force from the road to the wheel in the in-plane mode of operation. The tire generates lateral force when cornering occurs to steer the vehicle and is the out-of-plane mode of operation. The in-plane mode of operation is associated with ride performance of the vehicle, while the out-of-plane mode is highly related to handling performance.

2.1.3 Tire model as a subsystem in a vehicle model

A tire/wheel assembly is a subassembly to the suspension corner and interacts with the steering and suspension subsystem. The interaction embeds complex mechanics which considerably influences the overall performance of a vehicle. To understand the role of a tire as a component of a vehicle, the first step is to figure out the relationship between a tire and the remaining vehicle subsystems. Figure 2.5 depicts the interaction among different vehicle subsystems affecting vehicle dynamics. The inputs and outputs of the tire become internal "state variables" in a full vehicle system. This framework applies to any full vehicle model in a general sense, but it is not necessary to implement every aspect for a given vehicle model.

From a driver's perspective, one can control a vehicle through the throttle, brake pedal, and steering wheel. The throttle controls the driving torque output to the wheels via the power train. The driving torque, T_P, can be seen as one input. In the same way, the brake pedal can exert brake torque on the wheels to stop the rotation of the wheel; so the brake torque, T_B, becomes a second input. Steering wheel angle, δ_{SW}, dictates the angle of the front wheels by displacing the tie rod and is deemed as a third input. A combination of these inputs determine the position and spin mode of the wheels. Some of the kinematic quantities of the tire can be determined. For example, a loaded radius, R_L, is defined as the distance from the wheel center to the contact center at a particular operating condition; a slip angle, α, is defined as the

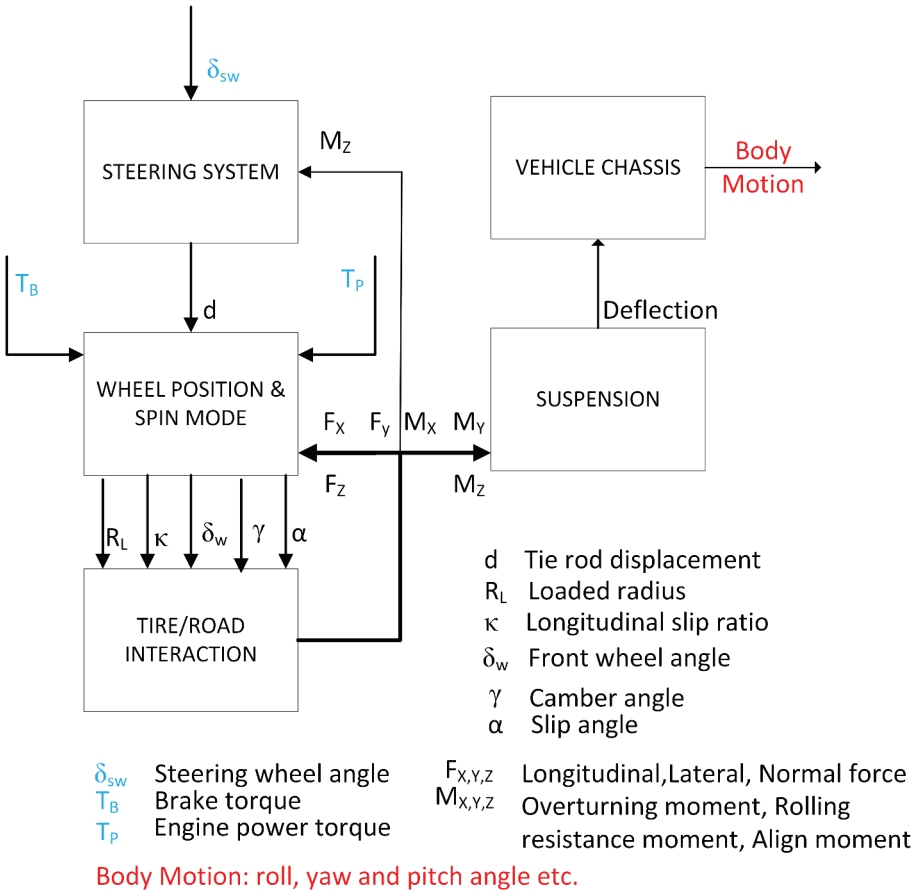

Figure 2.5: Tire model as a subsystem in a typical full vehicle model. The inputs are highlighted in blue, and outputs are highlighted in red in the illustration.

angle from the X_T axis to the normal projection of the tire contact center trajectory velocity on the $X_T - Y_T$ plane. (Note: This general definition of slip angle is not constrained by a flat road surface scenario). Referring to Fig. 2.5, a loaded radius and slip angle are the inputs for a tire model. Then the resultant forces and moments generated through the tire-road interaction in a contact patch provide feedback to the wheels via tire-rim contact to influence the position and spin mode of the wheels. One typical example occurs when a driver puts effort in turning the front wheels (changing the kinematics of the front wheels) in order to make a turn. The aligning moment, M_Z, then feedbacks through the steering system from the contact patch to the driver, who can feel the tendency of M_Z to align the wheels' heading with its path. At the same time, tire forces and moments transferred to a suspension system cause the deflection of suspension members, e.g. the structural components connecting the tire/wheel to the vehicle chassis. Since the suspension is connected to the chassis, the load transfer results in the motion of a vehicle body. More precisely, roll, yaw,

and pitch will occur. Usually, these kinematic quantities used to describe the vehicle body motion are regarded as the outputs of a full vehicle system.

2.1.4 Brief review of full vehicle models

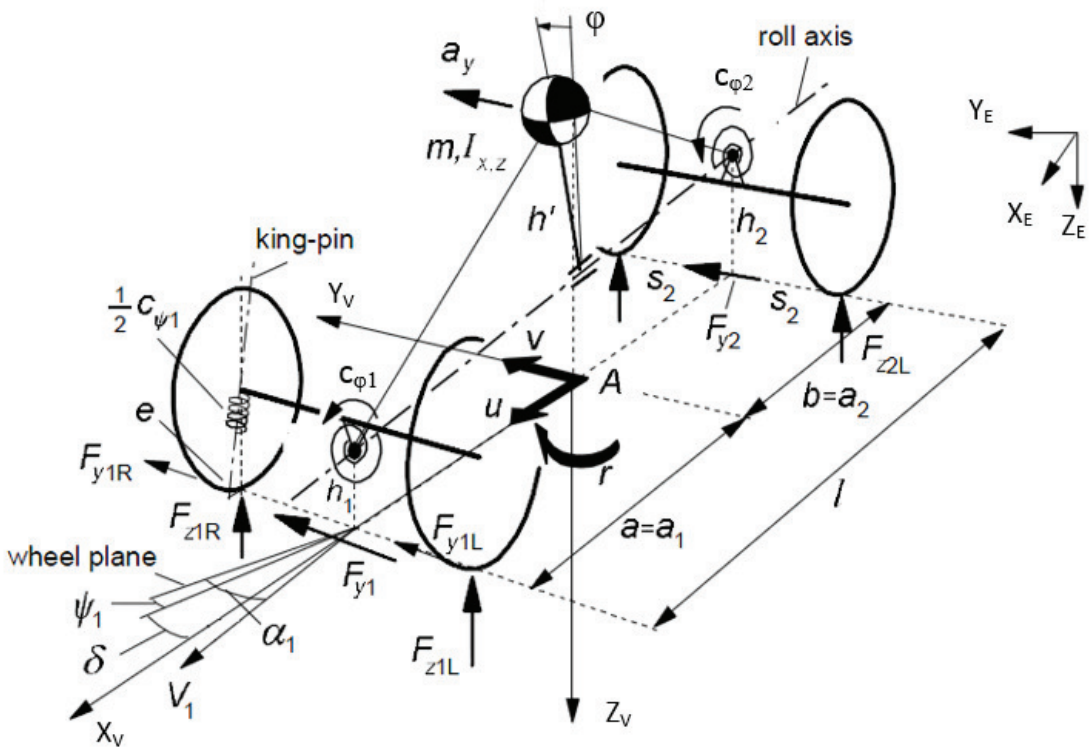

Figure 2.6: A parameter-type full vehicle model with four degrees of freedom: longitudinal, lateral, yaw, and roll (Reprinted and Modified from Tire and Vehicle Dynamics by Pacejka with permission of the Butterworth-Heinemann)

A tire model has to be incorporated into a vehicle model to fulfill the purpose of vehicle dynamics simulation. This section discusses some essentials of a vehicle model. Generally, vehicle models fall into two categories. One type is the so-called lumped-parameter model. Vehicles are represented by their mass, mass moments of inertia, dampers, springs, stiffness values, and all relevant kinematics and compliance characteristics. An example of a lumped-parameter vehicle model is shown in Fig.2.6, and its detailed description can be found in Pacejka [4]. Equations of motion for this type of vehicle model can be derived based on Newtonian mechanics. The second type is the so-called component-type full vehicle model which builds equations of motion involving parts of the suspension and chassis to get a realistic description of kinematics

and dynamics, as shown in Fig. 2.7. Each member of the vehicle system (excluding tires) is usually treated as a rigid body. The members are connected through different types of joints. Lagrangian mechanics is a better way of formulating the constrained multi-body system than classical Newtonian mechanics.

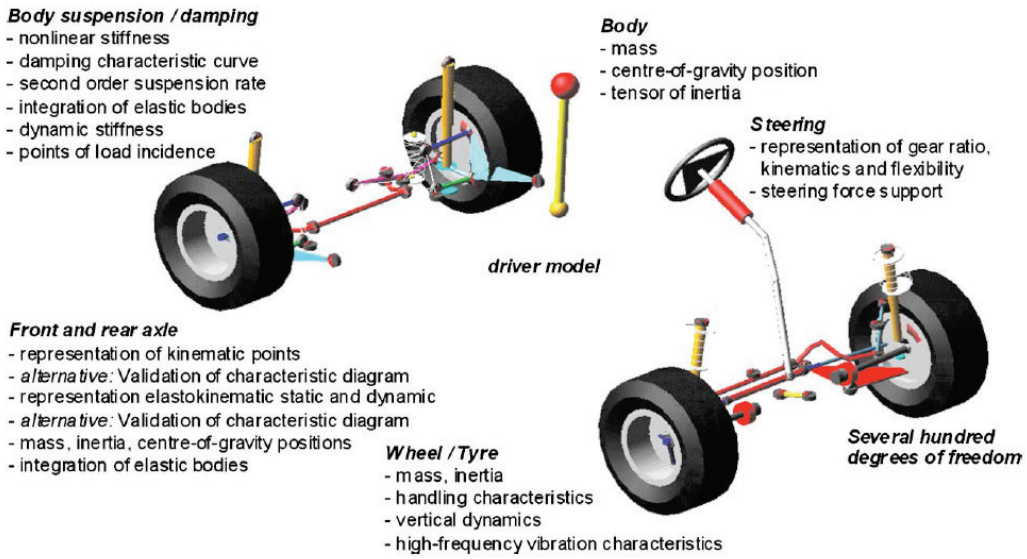

Figure 2.7: A component-type full vehicle model. An ADAMS/Car model with main components of chassis and suspension that have to be considered in order to obtain a realistic representation of a real world vehicle. One important component is the tire model. (Reprinted from Hüsemann [5] with permission of the Allen Press).

If a tire is simply treated as a rigid cylinder in a vehicle model, the majority of the tire mechanics are lost. The magnitude of stiffness of a tire is around ten times smaller than a chassis and suspension component. The flexibility of the tire structure causes complex deformation modes of the tire and interaction with the road surface. The tire as a load-carrying member transferring loads to chassis through the suspension members greatly impacts the overall response of a vehicle. Therefore, from a computational point of view, ideally proportional degrees-of-freedom should be spent on modeling a tire compared to the system of a suspension and chassis.

2.2 Contemporary Tire Models for Vehicle Simulation

Considerations of tire modeling vary depending on different application purposes. The physical-based tire models for an application in vehicle simulation are mainly MBD-type models. When the tire is regarded as a functional component of a vehicle,

the tire-road interaction becomes more important. An example would be the classic brush tire model which frequently appears in various textbooks. In the brush model, the rubber volume between the tire and the road surface is partitioned and abstracted into infinitesimal elements in the form of elastic bristles. These bristles can deflect in both lateral and longitudinal directions. The compliance of the bristles represents the elasticity of a combination of the tire carcass, belt, and tread. The focus of the brush model is to describe the major physical course in the contact zone between the tire and road, while the deformation is ignored for remaining part of the tire body. The contact interaction is characterized by two parameters, the lateral stiffness and longitudinal stiffness of the bristle in the brush tire model.

In contrast, a finite element tire model conventionally is more suitable for the analysis of detailed tire performance in the tire design domain where almost every aspect of tire construction has to be taken into account. Rarely is a tire model developed under the FEM framework for the purpose of vehicle simulation. This may be due to the difficulty in acquiring the material properties to feed into an FE tire model. Overcoming this difficulty is one of the novelties of this research. A published work, "FIAT FE tire model" has the most relevance to the tire model proposed in this dissertation. Even though both models are developed in the FEM framework, the approaches are very different. A detailed review is given in Section 2.2.5. The FIAT FE tire model is much less mature than the FTire, RMOD-K, and TameTire models, which have been commercialized for several years.

The following models will be reviewed: FTire, RMOD-K, and TameTire. They all belong to the MBD-type, but are much greater in complexity than the brush tire model. The Pacejka Magic Formula model is a semi-empirical model. Since the Magic Formula model is still the most widely used tire model in the vehicle industry, it is also briefly reviewed. The review will be developed according to the research scope shown in Fig. 1.2.

Since most of the tire models for vehicle simulation are the MBD-type, there is no direct help to the proposed tire modeling work. However, the basic concepts of modeling a tire according to the mechanics of tire components inspires the current work. The lesson learned from these MBD-type tire models is summarized in Section 2.4.

2.2.1 Magic Formula and MF-SWIFT tire models

The Magic Formula, developed through the cooperative effort of Bakker et al., Pacejka et al. [4], and Bayle et al., is the most widely used tire model to calculate the steady-state tire forces and moments under various slip conditions. Its typical field of application is for vehicle handling studies. The Magic Formula tire model is a semi-empirical function with a general form $y = y(x)$, where the independent variable x can be $tan\alpha$ or κ; and y is the output variable F_X, F_Y or possibly M_Z. The

semi-empirical function produces a curve to match measured curves for the lateral force and the fore-and-aft force as functions of their respective slip quantities. The Magic Formula requires a series of extensive full-tire tests covering a certain range of vertical tire loads, slip ratios, and slip angles to calibrate the model.

The Magic Formula tire model has evolved to a full set of equations when a scaling technique was brought into enhance its performance. As the demand on the tire model is more capable of describing the transient tire behavior, the development of the MF-SWIFT, which stands for the Short Wavelength Intermediate Frequency Tire model, enables the model to handle frequencies up to 60-80Hz and wavelengths of 0.1-0.2 m.

The Netherlands Organisation for Applied Scientific Research TNO (Toegepast Natuurwetenschappelijk Onderzoek) turned these two models into commercial software packages known as MF-Tire and MF-SWIFT, which became an industry standard for modeling passenger car tires in the late 1990's.

2.2.2 FTire model

FTire (Flexible Ring Tire Model), developed by Gipser [6,7], is a full 3D physical-based tire model for both vehicle comfort and handling studies. FTire can deal with a frequency up to 200Hz induced by road irregularities even with extremely short wave-lengths. Moreover, it has full integration with a digital road library to support both rigid and deformable road surfaces. The computing time of the FTire model simulation is "no greater than 20 times real time" [7] and is faster than explicit FE models. These features make FTire competitive in the tire model market.

2.2.2.1 Sub-models of FTire

The FTire model consists of five elements: mechanical model, thermal model, tread wear model, air volume vibration model, and flexible rim model. The core is the mechanical model.

In the core mechanical model, the most essential component is the flexible ring which is used to describe the belt. The ring is discretized by a finite number of so-called 'belt elements or segments' where each belt element has degrees of freedom to allow belt translation, belt torsion (rotation angle about the circumferential axis), and belt bending. These belt elements are elastically connected to the wheel rim by nonlinear force elements in the radial direction consisting of springs, dampers, Maxwell elements, and spring-friction series connections ('elastoplastic' elements). A number of belt elements span the circumferential and transverse directions over the space to form the carcass. The belt elements are also connected through springs and dampers. Inflation pressure as an 'operating condition' affects all the stiffness values. The overall flexible ring structure mainly deals with tire compliance of the in-plane and out-of-plane responses.

To model the tire-road interaction, a number (typically 5 to 50) of mass-less 'tread elements' are associated to each belt element. These tread elements not only carry additional stiffness and damping, but also interaction properties determined by the sliding velocity on the ground and the local contact pressure. The tread blocks are arranged along several parallel lines, such that both longitudinal and lateral resolution can be optimized according to the wave-length of road. The road tangential plane is computed individually for each contact element; therefore, FTire is able to cope with even sharp-edged obstacles on road.

The remaining sub-models enhance the base mechanical model. For example, the thermal model takes into account tread rubber temperature as a factor to further influence the frictional property.

2.2.2.2 Parameterization of FTire

As stated in the FTire documentation, "parameterization of FTire, as for all comparable physically based tire models, is not easy and clearly needs some experience" [8]. The whole process contains a series of tests including:

- identification of static properties,
- identification of steady-state rolling properties,
- identification of dynamic cleat test,
- identification of foot print, and
- identification of friction characteristics.

To complete those tasks, users are assumed to be able to access a professional tire test facility, which sets barriers for many users. The process is time consuming and costly. As an example, the FTire staff quotes about $30,000 U.S. dollars for parameterization of the Hoosier LC0 racing tire.

2.2.3 RMOD-K tire model

The RMOD-K tire model, developed by Oertel et al. [9, 10], is a family of models that predict tire response over a wide range of driving maneuvers and ride performances. The latest version is RMOD-K 7.

The rigid-belt model RMOD-K 7 RB covers the frequency area to 100Hz, simplifying a tire belt as a "rigid belt" which is defined by a radius and belt width. The rigid belt can be connected to the rim in several ways: 1) using a fixed joint, 2) a planar joint and bushing, and 3) a bushing element between belt and rim. Each type of connection constrains different degrees-of-freedom of the rigid belt, all representing

a special mode of the tire. The contact region is determined by cutting a parameterized tire geometry with a ground surface. The tangential behavior in the contact is defined by two coupled first-order partial differential equations [11]. The normal contact stress is assumed to be distributing quadratically only on the longitudinal direction.

The flexible belt model RMOD-K 7 FB has a larger applicable range when road disturbances such as cleats or other small wavelength obstacles are taken into account. The tire structure is represented by specially designed rebar elements to focus on the compliance of the belt and sidewall structures. Contact is realized by so-called 'gap sensors' on top of the belt-node grids. The location of these gap sensors can be arbitrarily chosen, while the actual position and velocity of the sensors are calculated using the positions and velocities of belt nodes as boundary conditions. The normal force distribution comes from the gap sensor information. The tangential contact force results from the sticking or sliding state of the gap sensors. The contact algorithm is based on the penalty method.

The RMOD-K FEM model was withdrawn from the RMOD-K 7.x model family and is no longer under development. RMOD-K FEM was a single-purpose nonlinear finite element model. It ever severed as a tool for parameter identification to feed input parameters of RMOD-K 7 FB together with HOPSPACK (Hybrid Optimization Parallel Search PACKage).

Similarly, a static tire test, dynamic modal test, and steady-state test have to be carried out in order to calibrate the RMOD-K model.

2.2.4 TameTire model

The TameTire model developed by the R&D department of Michelin [12] is a physical-based model for both steady-state and transient vehicle handling dynamics, and emphasizes the thermal effect. Michelin has identified that the thermal behavior of a tire impacts the transient response significantly. Given an example, the Magic Formula model of an F1 racing tire obtained by indoor tests does not apply well to the real environment when the tires experience on the track. Michelin recognized that one solution to improve the robustness and accuracy of a tire model is to strengthen its thermal behavior representation. TameTire pursues reconstruction of a wider range of track tests and test conditions.

TameTire consists of three base models: 1) the mechanical model, 2) the rubber material model, and 3) the thermal model. The mechanical model has a similar concept with the brush tire model. It uses the "brush element" for modeling the belt-tread interface, in which the total force is assumed to be the sum of the shear forces of the tread elements in the adhesion and sliding areas of the contact patch. Furthermore, the stiffness of the belt and sidewall are taken into account rather than rigid as in the traditional brush model. The material model is mainly for the

tire-road interface. The rubber properties, such as the shear modulus and glass transition temperature, govern the tread stiffness, the friction properties, and the heat generation. The thermal model calculates the contact temperature profile and heat flux from the tread to the track as well as the viscous heat generated in the tread. This thermal phenomenon finally changes the stiffness of the brush element and the tire-road interface property, then causes a impact on the global tire frictional force.

The TameTire model provides an improvement in the prediction of the tire response to a wider scope of testing maneuvers than other tire models. It has recently been made commercially available by IPG Automotive [13] as a fully integrated model in CarMaker. Static, steady-state, and dynamic tests are required to characterize the TameTire model, and users must register the service with Michelin.

2.2.5 FIAT FE tire model

In 2015, Bartolozzi et al. [14] from the vehicle company FIAT, published a preliminary result of an in-house developed FE tire model to be used in a full vehicle NVH simulation. Bartolozzi [14] cited the major drawback of an FE tire model used by tire suppliers as having such a large number of degrees-of-freedom that it is impossible to be included in a full vehicle simulation. On the other hand, a model that can have a proper representation of tire behavior and at the same time directly connect to the tire physical properties is needed. Bartolozzi's work is the only published work to be found by the author with similar motivation as this dissertation under the FEM framework. However the key difference between this dissertation and Bartolozzi's work is the approach used for model parameterization.

The physical properties included in Bartolozzi's model, e.g. the rubber Young's modulus, are "not supposed to be known or measured, but are determined by means of an optimization process which tunes the numeric inertances of the inflated tire model with a few measured point inertances" [14]. The multiple objective functions are minimizing the root-mean-square errors between experimental and numerical Frequency Response Functions. The model simulation was conducted numerically in Nastran software. The optimization is completed using the commercial software modeFRONTIER, and the optimization algorithm is chosen to be the MOGA-II [15]. There were twelve physical parameters to be estimated through the optimization process with a plausible range set for each parameter as constraints. The methodology was exercised on two passenger tires, 185/55R15 and 225/50R17. The optimized sets of tire properties are summarized in Table 2.1.

The absolute values of the parameters were concealed by the paper's author, and only relative values were published. It is important to note that some parameters vary significantly between the two tires, e.g. the Nylon Young's modulus highlighted in the second row of the table. The Young's modulus of Nylon fiber in the tire

Table 2.1: Optimized sets of tire properties (relative values) in a table reprinted from Bartolozzi's paper [14] with permission Copyright ©2015 SAE International. Further distribution of this material is not permitted without prior permission from SAE.

Variable name	Initial values	185/55R15	225/50R17
Steel Young's modulus	100 %	96.5 %	90.5 %
Nylon Young's modulus	100 %	288.5 %	29.8 %
Polyester Young's modulus	100 %	178.0 %	195.0 %
Rubber Young's modulus	100 %	83.2 %	220.0 %
Steel volume fraction	100 %	63.6 %	36.4 %
Nylon volume fraction	100 %	135.2 %	135.2 %
Polyester volume fraction	100 %	153.2 %	114.8 %
Steel cord layer thickness	100 %	104.0 %	78.4 %
Nylon cord layer thickness	100 %	192.3 %	115.4 %
Polyester cord layer thickness	100 %	81.0 %	123.7 %
Steel cord orientation angle	100 %	156.8 %	157.3 %
Rubber density	100 %	104.0 %	124.0 %

185/55R15 is almost ten times as much as in the tire 225/50R17, while the remaining parameters' values are roughly on the same scale. The paper's author did not give a sound explanation for the difference. One interpretation would be that the optimized set of parameters only satisfies an equivalent overall response of the model, but that the actual physical values cannot be guaranteed.

Some comments to Bartolozzi's model are 1) so many parameters are involved in one optimization process that is difficult to pick out a unique and interpretable solution; 2) the FRFs should always contain an amplitude-frequency part and phase-frequency part together. The author only used amplitude-frequency response to formulate the problem thus neglecting the phase-frequency information; and 3) the tread pattern of the tire models was not considered, which further affects the tire-road interface. Therefore, the tire forces in a rolling condition might not be accurately predicted.

2.3 Finite Element Method in Tire Modeling

The Finite Element Method (FEM) has been widely adopted in analyzing stress and strain of complicated structures since 1970, which cannot be easily accomplished by traditional measurements. In the tire industry, FEM has been used in the field of tire design by dealing with typical questions on local stress and strain analysis which

involves constitutive, geometric, and boundary nonlinearity. The FE tire models developed by tire companies 1) are based on complex physical models, e.g. material models and contact models; and 2) can fulfill the real-world boundary conditions in a more sophisticated way than other MBD-type tire models. However, these kinds of FE tire models traditionally can hardly be used for a vehicle simulation. Consequently, only a small portion of tire models which belong to the tire design category will be reviewed.

It is also difficult to guarantee the state-of-art modeling techniques applied to tire modeling by the FEM through publications because many models are proprietary to tire manufacturers and are not public. The following review is based on the published work, but most of the models are for the purpose of tire design, which deviates from the main theme of the current dissertation. Relevant to the current dissertation is the understanding of functional components of a tire and guidelines for decomposition of the structure in both modeling and physical experiments. The mechanics associated with each component are discussed in Section 4.1.2. The focus here is on how to properly represent the tire mechanics and model each tire structural component by the FEM.

2.3.1 Tread modeling using FEM

The tread is the only part of the tire that contacts the road surface directly under normal operations. The tread provides the frictional force required to transmit driving, braking, and cornering forces. The tread is a bulk component of rubber designed to carry compression and transverse shear loads when interacting with the road no matter its geometry, such as no tread pattern [16], simple groove pattern [17], or very complex pattern [18]. The complexity of the tread pattern dramatically increases the difficulty of model generation. The Hoosier LC0 racing tire used in this study has no tread pattern.

Despite the difference in tread geometry, 3D solid brick elements are widely used for the tread modeling. Tetrahedron elements may induce inaccurate contact stress used in the contact modeling, but tetrahedron elements may be necessary, particularly for complex tread pattern modeling. The influence of element type on the contact solution has been studied by Surendranath [19]. The 3D solid brick element is adopted for our simplified FE tire model, and reduced integration instead of full integration for elements is commonly preferred [17]. The nearly incompressible property of rubber material also requires reduced integration for easy convergence of the numerical solution.

2.3.2 Sidewall modeling using FEM

Since the ratio of thickness over the circumferential or meridian dimension of a tire sidewall is below 0.05, discretization of the sidewall using shell elements [20,21] is a popular approach to reduce the number of degrees-of-freedom. The formulation of thin shell element assumes that Kirchhoff hypothesis holds. Because of the Kirchhoff hypothesis, the transverse deformation effect, which is the relative shear between the top and bottom surface of a shell element, is not allowed. The formulation based on thick shell theory can handle transverse shear. The composite shell formulated with thick shell theory was historically used for sidewall modeling. A guideline given by Gall et al. [22] stated that "although the use of shell elements is justified to quickly predict trends and perform certain comparative analyses, it is not suited to predict absolute values" of the local strain and stress.

Today, the sidewall is commonly modeled using 3D solid elements in tire design modeling because the computational resources are no longer stringent. The author has attempted to use thick shell elements and continuum shell elements for modeling the sidewall to save computing time. The static wheel load vs. deflection response shows no significant difference in the derived tire spring rate between the model using shell elements and 3D solid elements. However, for dynamic rolling simulation, the model using shell elements for the sidewall has the convergence problem caused by the hourglass effect of shell elements. Therefore, this work will use 3D solid elements for modeling the sidewall.

2.3.3 Carcass and Belt modeling using FEM

A typical carcass or belt is a stack of reinforced rubber layers. Each layer is a thin rubber sheet reinforced by a series of unidirectional fibers or steel cords. The rubber matrix of such a sheet offers strength in-plane, but typically has negligible out-of-plane bending stiffness. The layers are mainly subjected to tensile loads rather than compressive or any other out-of-plane loads. Membrane elements [23] can be used to discretize this kind of structure. Membranes have zero bending stiffness and constant stress distribution across the thickness, and need no numerical integration in the thickness direction. However, for some kinds of tire belt subsystems, the bending stiffness of layers is considerable, and shell elements that can represent bending must be used [17, 24].

In addition to the rubber matrix of layers, the embedded reinforcement fibers contribute more to the in-plane stiffness of layers. The fiber-reinforced rubber elasticity is a subject studied by many researchers. Papers in this subject started to appear in 1955 by Adkin and Rivlin [25] for the mathematical models of hyperelastic materials reinforced by inextensible cords. A mathematical model of the rubber reinforced with extensible cords is studied by Pósfalvi [26]. Their studies were for membrane effects only. More advanced treatment of this topic was developed by Helnwein et al [27]

and will be further discussed in Section 4.4.2.1.

Helnwein's theory leads to a popular modeling technique referred to as the "rebar layer" technique. This dissertation adopts the rebar layer technique together with membrane elements as the discretization method because the carcass of the Hoosier LC0 6.0/18.0-10.0 tire has small bending stiffness.

2.3.4 Bead coil modeling using FEM

Tire beads are made of hard-drawn steel wires encased in rubber which is called "bead filler." The purpose of the bead bundle is to anchor the carcass plies and help a tire to be seated firmly on the wheel rim. This is a special branch of pneumatic tire research, and its function and application scenarios determine how to model the tire beads. If the focus is studying whether a debead phenomenon may occur under a low inflation pressure and high speed for a rolling tire, the bead coils have to be modeled in detail by 3D solid elements [17]. If the main consideration in the model is concerned with global tire forces and moments, the bead coil can be further simplified as a curved beam and discretized by beam elements.

This dissertation is not interested in the interaction between the tire beads and the wheel rim. We assume the tire is well-seated on the wheel rim all the time, and we use " tie" constraint to deliberately simplify this tire-rim interaction. Therefore, modeling the bead coil with beam elements satisfies the needs of this research.

2.3.5 FE tire model size vs. computing power

The relationship between the size of the FE tire model and the computing power deserves attention in a chronological order. Due to computational limitations, most of the tire simulations by the finite element method have been limited to quasi-static analysis and were mainly in the form of axisymmetric models before the 1990s. Until the emergence of 3D FE tire models, it was impossible to achieve general tire rolling and vibration analysis using FEM. It was not until the late 1990s that transient responses had been studied using an explicit FEA code. Figure 2.8(a) shows the size of FE tire models varying with time from the year 1982 to 1996 reprinted by Gall [22]. The trend of change in the model size positively correlates with the trend of change in the capability of computer power over the same time period as in Fig. 2.8, which indicates that the model size is mainly constrained by the available power of the computer.

Since 1996, the increase in computing power together with dramatically refined FE codes can support investigation of very subtle phenomenon using FE tire models, such as debonding effects of reinforcement fiber from rubber matrix, or strain concentration on the edge of belts. A full-vehicle simulation does not need a code to resolve these local behaviors of the tire. Thus, it is reasonable to save computing resources by

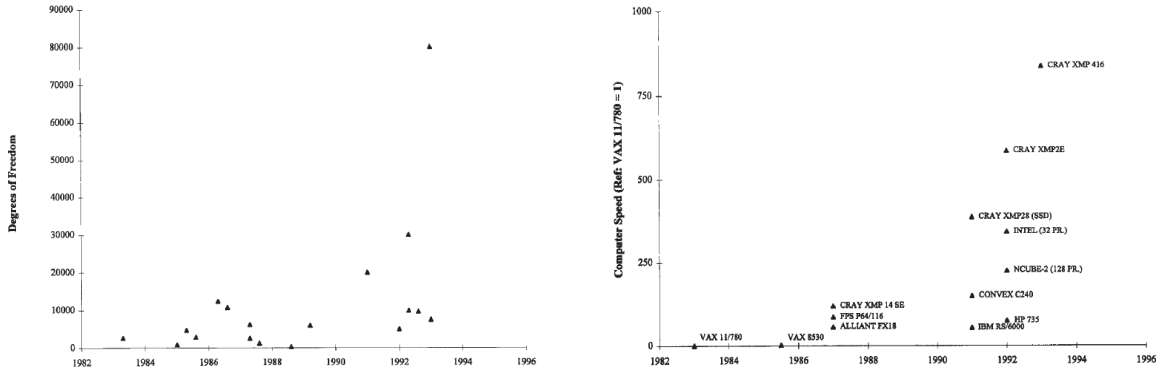

(a) (b)

Figure 2.8: Positive correlation between the size of FE tire models and computing power: (a) power of computers vs. time (the time axis reflects the date the computers were benchmarked by the authors, not the date when they were first available); (b)size of finite element models vs. time. Reprinted form Gall [22] with permission of the Allen Press.

creating an FE tire model focusing on high fidelity global responses. The saved computing power is used to resolve the degrees-of-freedom of a vehicle model, which is one of the motivations for this dissertation. The increasing computing power and refinement of computing algorithm make it hard to deny that the FEM can be applied to the domain of vehicle simulation. There is a developing opportunity for using FEM in elastodynamic vehicle simulations in the future.

2.4 Summary

In the summary, different types of tire models are categorized by Pacejka as shown in Fig. 2.9 which shows the big "picture" of tire modeling. The author attempts to spot the location representing the proposed simplified FE tire model in this picture.

There are four categories of tire models in Fig. 2.9 distinguished by their approaches of development. Measured tire characteristics are described through curve fittings and interpolation schemes for the models in the far left category. The models have a given type of formula and a set of parameters that are usually assessed with the help of a regression procedure to yield the best fit to the experimental data. A well-known empirical model is the Magic Formula. The models developed by the similarity approach in the second category are based on the typical tire behavior characteristics obtained from the measurement, then off-nominal characteristics were derived through distortion, rescaling, and multiplication of the original characteristic curve. Relatively simple physical models of the third category, such as the brush

tire model, rely on simple physics and strong assumptions. Some early MBD-type tire models, e.g. string models, ring models, and beam-on-elastic foundation models, belong to this category. These early tire models generally considered the tread to be a pre-stressed string or a ring and the sidewalls to be elastic foundations supporting the tread structure. These models include a set of equivalent lumped parameters that requires multiple full-tire tests to determine. They can be easily incorporated to a lumped parameter-type vehicle model in Section 2.1.4. The value of models in this type is providing a fundamental understanding of tire behavior in simple form. The finite element model for tire design belongs to the fourth category and is based on complex physical models.

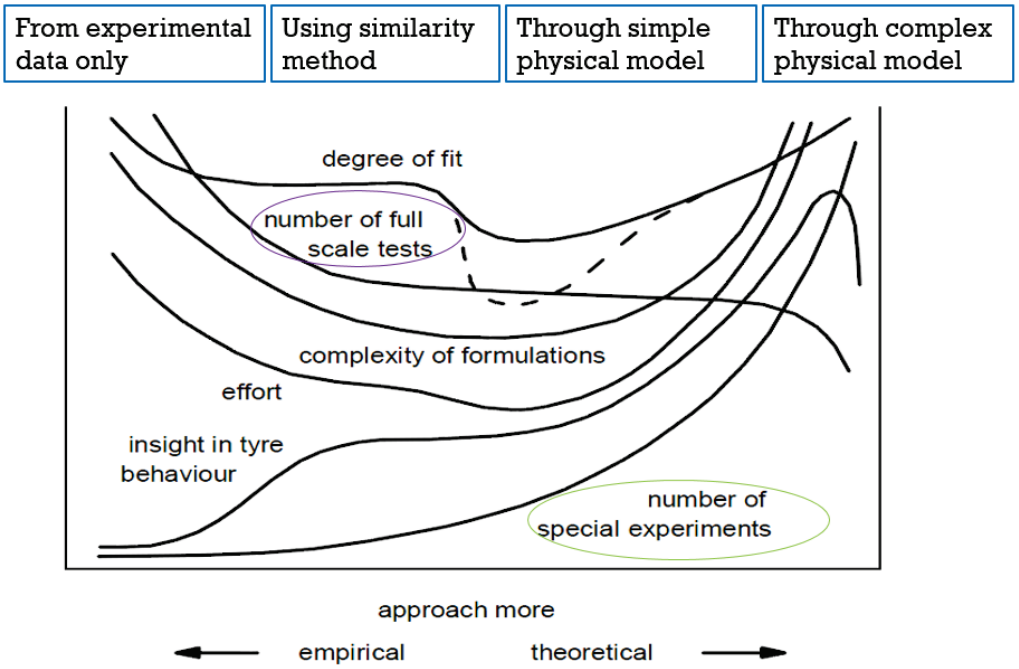

Figure 2.9: Categories of tire models developed by various approaches for different purposes. (Reprinted and Modified from Tire and Vehicle Dynamics by Pacejka [4] with permission of the Butterworth-Heinemann.)

Figure 2.9 also illustrates characteristics of different types of tire models. From left to right, the complexity of the formulation becomes higher, and provides more insight into tire behaviors. The model is less dependent on full-scale experiments and more dependent on theory of the physical structure of the tire. However, the number of small scale and special experiments required to calibrate the model increases. Tire models in the middle region will be simpler but less detailed than models on far right. The models in the left region are regarded to be more suitable for an application of vehicle simulation, whereas models in the right region may be more appropriate for

the analysis of detailed tire performance.

Researchers are making efforts to develop tire models that belong to the third or fourth categories with an emphasis on their applications in vehicle simulation. All of the models of this type reviewed in Section 2.2 are not open to the public. It is hard to use and quantitatively evaluate the performance of those models for researchers in both academia and industry without being a customer.

The current work will develop a tire model in the middle of the third and fourth categories and will offer the methodology to the public domain. Since we are pursuing a physical-based model, any empirical method to describe the tire behavior is abandoned. The common issues that need to be solved for any physical-based model are:

1. The compliance of the tire carcass which determines the deformation of a tire under various operational conditions. It further impacts the resultant forces transmitted from the road to the wheel center. The identification of wheel axle loads is a key step for vehicle dynamics simulation.

2. The compliance of tire tread rubber which influences the shape of the contact patch and distribution of normal contact pressure. For example, even the simple brush tire model has a 1D line-section contact patch and quadratic distribution of normal pressure as its basic assumption. In contrast, an FE tire model has a 2D contact patch and distribution of normal pressure.

3. The interaction between the tire and the road. The frictional property of the tire tread-road interface determines the generation of tire forces to maneuver a vehicle.

All the models in this literature review have solutions to those issues by various approaches. The proposed model by this dissertation addresses those issues in two parts. One part is tire structure modeling ,which includes points 1) and 2); while the other part is tire-road contact modeling which covers points 2) and 3). The concept and strategy are expanded in Chapter 3.

Chapter 3

Basic Considerations of Tire Modeling Using FEM for Vehicle Simulation

3.1 Why Finite Element Model

The modeling work started from a given tire product, the Hoosier LC0 tire, and no information is available from the tire provider. The resource and cost limitations for building a tire model also have to be taken into account.

The whole modeling work consists of two aspects, model design and parameterization. These two factors cannot be dealt with separately. Model development needs to consider how to acquire parameters associated with it. A series of test plans are developed to identify the model parameters. Much of the usability of a model hinges on whether the input parameters are easily determined.

According to Pacejka's map of tire models in Fig. 2.9, building a model by the finite element method relies more on small-scale and special experiments instead of large-scale full-tire tests to calibrate the model. This feature lowers the cost to acquire the required data and makes it practical to complete the tasks without tire companies' support.

A tire model developed through the finite element approach has several inherit

merits: 1) it possesses physical insights into the tire mechanics, 2) it can handle more complicated real-world boundary conditions for contact than other MBD-type tire models and offer more detailed information about contact pressure, and 3) it has great potential for expansion (illustrated in Fig. 3.1) by including more sophisticated sub-models, e.g. adding a thermal model into the basic elastic material model or adding an advanced friction model into the basic contact model.

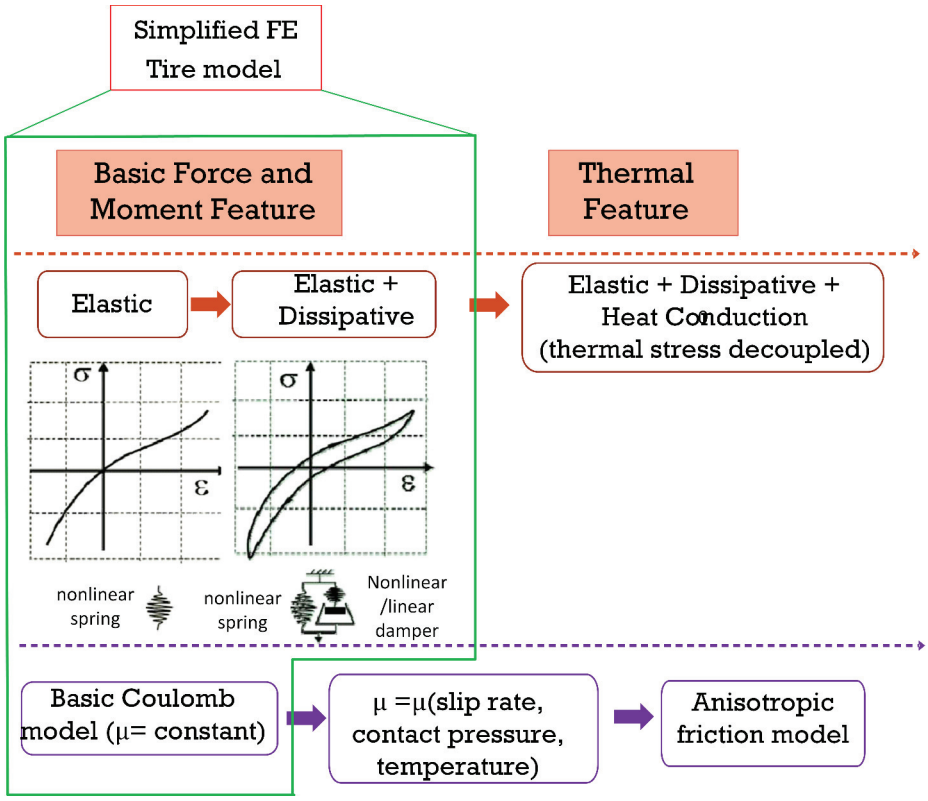

Figure 3.1: Potentials of expansion for an FE tire model

Based on the requirements and constraints mentioned in Section 1.3, the finite element method seems to be a preferable approach towards the goals of this tire modeling work. Two fundamental aspects of the model development need to be investigated, which are modeling the tire structure and modeling the tire-road contact in the framework of FEM.

3.2 Tire Structure Modeling

The structure of the bias-ply racing tire can be simply described as a rubber toroid, which is reinforced by a fiber net with balanced stacking angles underneath the rubber. The mass and stiffness distribution are the most critical factors of the

structure. The description of mass and stiffness distribution is required to satisfy the global response. If the prediction of local strains/stresses is pursued, the mass and stiffness distribution needs to be more accurately described.

The saved computational resources from the structure modeling can be used for contact modeling, which plays the most important role for the generation of tire forces and moments.

3.2.1 Considerations on material models

The material constitutive relationships essentially determine the model's representation of inherent mechanics of different tire components. For example, the stiffness of the carcass layers dictates the compliance of the tire body. The stiffness of the tread rubber directly influences the contact stress in a contact patch.

- Hyperelasticity and viscoelasticity of the rubber compound

  The hyperelasticity of rubber in the scope of this research mainly considers the nonlinear elastic stress-strain relationship without referring more advanced rubber behavior such as the Mullins effect or Payne effect.

  The time-dependent property, viscoelasticity, is another significant characteristic of rubber. The influence of viscoelasticity on global tire forces and moments is limited, and it relates the energy dissipation of a rolling tire to the hysteresis loss of rubber. Modeling heat generation is not an immediate objective of this research, so viscoelasticity has not been included in the model yet. However, the Dynamic Mechanical Analysis (DMA) test of the Hoosier tire rubber samples has been started.

- Fiber-reinforced rubber elasticity

  The carcass-ply or belts are fiber-reinforced structures, thus the elastic properties vary depending on the orientation and arrangement of embedded fibers or steel cords. The Halpin-Tsai formulae with Classic Lamination Theory (CLT) is a candidate to deal with this kind of problem by representing the laminate layers as one homogeneous, orthotropic thin shell. Equivalent elastic properties along different principal directions are derived accordingly. The application range of this modeling method is only good for linear and small-strain problems. Before the emergence of new constitutive theories, the Halpin-Tsai formulae with CLT was widely used in tire modeling [28]. After that, the so-called "rebar layer" theory became prevalent. The basics of the "rebar layer" modeling approach will be further discussed in Section 4.4.2.

3.2.2 Considerations on nearly incompressible property of rubber

The element type with complex formulation may reflect the mechanics more precisely but costs more computing resources. For example, to model the tread rubber compounds, the hybrid formulation of 3D brick elements may capture the nearly incompressible property of rubber (which implies that the bulk modulus approaches infinity and the Poisson's ratio is 0.5). Whereas the complexity of formulation may be cut down if the incompressible property is not strictly required, an alternative approach is to take the "normal way" of 3D element formulation with Poisson's ratio being slightly smaller than 0.5. A trade-off always exists between the effectiveness which associates the formulation of elements and the efficiency which associates with the number of degrees-of-freedom. The element type is also constrained by the solver. For example, Abaqus/Explict does not support the hybrid formulation of nearly incompressible 3D elements.

3.3 Tire-Road Contact Modeling

There is no argument that a contact algorithm is critical to the numerical modeling of tire-road contact because all the tire forces are developed from the interaction in the contact patch. The counterpart of the tire structural modeling is the tire-road contact model. The road surface can be flat or irregular, and hard or soft. If the road surface is hard, it is commonly treated as a rigid surface in simulation, while if the road surface is soft, which is commonly called "off-road," it has to be regarded as a deformable body and opens a completely different research area. In this research, the road surface is reasonably modeled as a flat rigid surface since the race track or Calspan flat-track machine has a flat and hard road surface.

A contact algorithm is to detect penetration between two objects, and then calculate a response that eliminates or minimizes the penetration. There are two types of contact algorithm: general contact algorithm and contact pairs algorithm. The general contact algorithm is more widely used for self-contact of a single deformable body. An example of such a problem is a rubber seal that folds over on itself [29]. The contact pairs algorithm is more common for solving contact between two deformable bodies, and contact between a deformable body and a rigid body. A rolling tire on a hard road is such a typical application case. Although the implementations of the general contact algorithm and contact pair algorithm in Abaqus share many underlying algorithms, the pairwise specifications of contact interactions is often more efficient and robust for an analysis compared to an all-inclusive self-contact approach to defining contact. For a tire-road contact simulation, the contact pairs algorithm is preferred. Both Abaqus/Standard and Abaqus/Explicit support the contact pairs algorithm.

The formulation of contact and numerical methods in Abaqus includes a choice of a contact discretization method, a tracking approach, and assignment of "master" and "slave" roles to the pair of contact surfaces.

A traditional "node-to-surface" (or "slave node-to-master segment" in other environments) and "surface-to-surface" are two ways of discretization. The "node-to-surface" discretization results in two major characteristics [30]:

- "The slave nodes are constrained not to penetrate the master surface; however, the nodes of the master surface can, in principle, penetrate the slave surface."
- "The only information needed for the slave surface is the location and surface area associated with each node; the direction of the slave surface normal and slave surface curvature are not relevant. Thus, the slave surface can be defined as a group of nodes – a node-based surface."

The "surface-to-surface" discretization has two key characteristics [30]:

- "The surface-to-surface formulation enforces contact conditions in an average sense over regions nearby slave nodes rather than only at individual slave nodes."
- "The contact direction is based on an average normal of the slave surface in the region surrounding a slave node."

In general, surface-to-surface discretization provides more accurate stress results than node-to-surface discretization. The "surface-to-surface" discretization is used because it avoids numerical stress concentration on a single contact node and typically gives more accurate contact stress distribution. The pay-off is increasing the computing cost since it involves more nodes per constraint. Surendranath [19] provided a study of performance when using the surface-to-surface discretization for tread pattern modeling.

The contact tracking approaches account for the relative motion of two interacting surfaces. The finite-sliding tracking approach allows for arbitrary relative separation, sliding, and rotation of the contacting surfaces, whereas the small-sliding tracking approach assumes that small displacement occurs between two surfaces. There is no doubt that only finite-sliding tracking can be used for contact of a rolling tire and road.

The rigid road surface must be assigned as the "master" surface, and the tire tread surface is assigned as the "slave" surface.

3.3.1 Considerations on normal contact

For normal contact behavior, "hard" contact is the most common contact pressure-overclosure relationship, as shown in Fig. 3.2. In contrast,"softened" contact relationships are also available where a linear law or an exponential law is employed to the pressure-overclosure relationship.

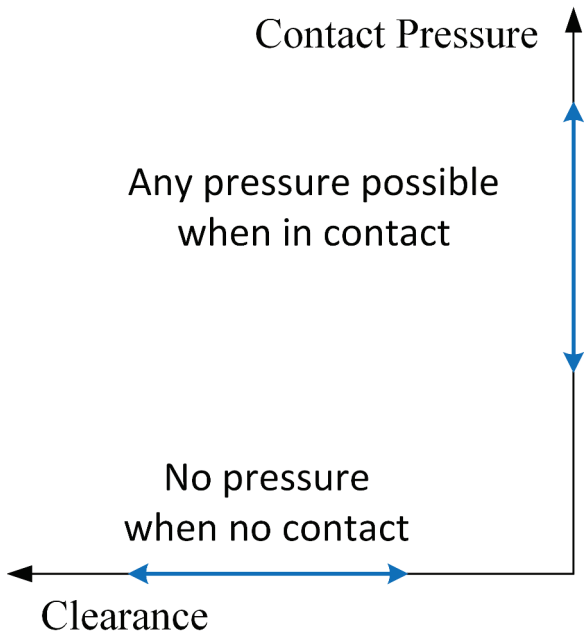

Figure 3.2: "Hard" contact pressure-overclosure relationship

Two common techniques for imposing normal constraints are the penalty method and the Lagrange multiplier method in Abaqus/Standard. The penalty method is a stiff approximation of the ideal hard contact, and the augmented Lagrange method uses the same kind of stiff approximation as the penalty method but also uses augmentation iterations to improve the accuracy of the approximation. In addition, the direct method, which strictly enforces a given pressure-overclosure behavior per constraint without approximation, is also available in the latest release of Abaqus. When "softened" contact relationships are adopted, using the direct method is necessary. For "hard" contact, all three enforcement methods of normal constraints can be used. The computing efficiency decreases in the order of penalty method > augmented Lagrange method > direct method, whereas the accuracy is in the reverse order. In Abaqus/Explicit, two methods to enforce contact constraints are the kinematic contact method and the penalty method. The kinematic method uses a kinematic predictor/corrector approach to strictly enforce contact constraints, while the penalty method allows for treatment of more general contacts which imposes a weaker enforcement.

3.3.2 Considerations on tangential contact

The relationship of interaction between contact surfaces in the tangential direction, known as the friction between the contacting bodies, is usually expressed in

terms of the shear stress at the interface of the bodies. Abaqus supports several friction models, from a simple Coulomb model to an anisotropic friction model and even user-defined models. The current work adopts the simple Coulomb model due to its capability of capturing the dominant mechanics and ease of obtaining the required parameter.

For a three-dimensional simulation, two orthogonal components of shear stress, τ_1 and τ_2, are in a local tangential plane of interface between the two bodies. This is called "equivalent shear stress," τ_{eq}, defined as $\tau_{eq} = \sqrt{\tau_1^2 + \tau_2^2}$. In a similar way, the "equivalent slip rate/velocity," $\dot{\gamma}_{eq}$, combines two components of slip velocity (relative moving velocity between a local contact spot) $\dot{\gamma}_1$ and $\dot{\gamma}_2$ into $\dot{\gamma}_{eq} = \sqrt{\dot{\gamma}_1^2 + \dot{\gamma}_2^2}$. The basic Coulomb model assumes isotropic friction which indicates that the direction of the slip and the frictional stress coincide. In math, it is expressed as $\frac{\tau_i}{\tau_{eq}} = \frac{\dot{\gamma}_i}{\dot{\gamma}_{eq}}, (i = 1, 2)$. The basic Coulomb model states that no relative motion occurs if the equivalent frictional stress is less than the critical stress,

$$\tau_{eq} < \tau_{cr} \tag{3.1}$$

where τ_{cr} is proportional to the contact pressure, σ_n, in the form

$$\tau_{cr} = \mu \left(\sigma_n, \dot{\gamma}_{eq}, \bar{\theta} \right) \sigma_n \tag{3.2}$$

Notice that μ is the friction coefficient that can be a function of the normal contact pressure, σ_n, the equivalent slip rate,$\dot{\gamma}_{eq}$, and the average surface temperature, $\bar{\theta} = 1/2(\theta_A + \theta_B)$, at the contact point where θ_A, θ_B are the temperature at point A on the slave surface and point B corresponding to the nearest point on the opposing master surface. The user can even make μ depend on other average field variables at the contact point. If $\tau_{eq} > \tau_{cr}$, slipping of the contact point occurs. The process called "stick/slip calculations" determines when a point transitions from sticking to slipping or from slipping to sticking. For tire-road contact, the contact patch can be accordingly divided into the sticking region and slipping region as illustrated in Fig. 3.3. The pattern of sticking and slipping region varies dramatically depending on different tire operational conditions.

The ideal relation of shear stresses versus elastic slip is a threshold model which can be described by a step function, but it cannot be realized in numerical simulation. The numerical implementation of the relation of shear stresses versus elastic slip relies on a concept called "elastic" tangential slip, γ_i^{el}, which is defined as the reversible relative tangential motion from the point of zero shear stress. The "elastic" tangential slip is allowed to occur even though the current frictional state is sticking. Then the "elastic" tangential slip is related to the interface shear stress in a curve shown in Fig. 3.4 The slope in the relationship of frictional shear stress versus total slip is finite instead of ideally infinite while in the sticking state, in the form of

$$\tau_i = \kappa_s \gamma_i^{el}, \quad when\ \gamma^{el} < \gamma_{cr} \tag{3.3}$$

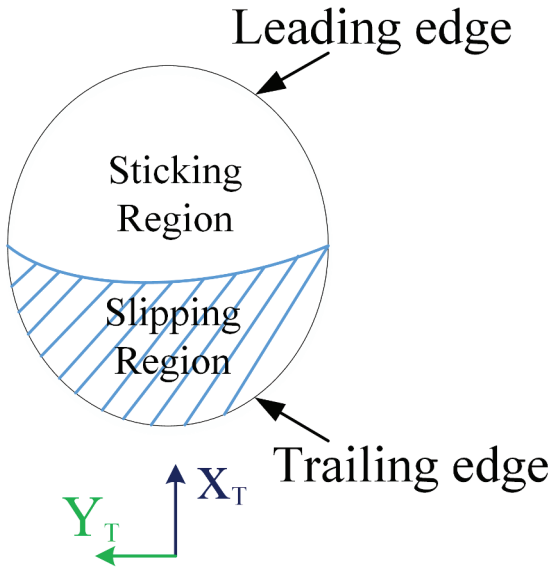

Figure 3.3: A schematic plot of a contact patch which can be divided into a sticking region and a slipping region.

When in the slipping state, the frictional shear stress achieves and stays at τ_{cr}. The slop κ_s, called the "stiffness in stick," is a characteristic of the constraint enforcement method. Frictional constraints are enforced with the penalty method by default in Abaqus/Standard and Abaqus/Explicit. An infinite stiffness in stick can be approximately satisfied by the Lagrange multiplier method in Abaqus/Standard, or the kinematic constraint method in Abaqus/Explicit, but sacrifices the efficiency. It is also required for users to specify an allowable elastic slip, γ_{cr}. The default value of γ_{cr} is automatically selected by Abaqus, providing a balance between efficiency and accuracy.

Special attention should be paid to steady-state transport analysis, which is an analysis procedure in Abaqus/Standard, because the no-slip condition is no longer concerned with γ_i^{el} but $\dot{\gamma}_i^v$, which is a shear strain rate called tangential slip velocity or "viscous" tangential slip rate. In math, it reads

$$\tau_i = \kappa_s \dot{\gamma}_i^v, \quad when\ \dot{\gamma}^v < \dot{\gamma}_{cr} \tag{3.4}$$

in the sticking state.. Here, κ_s is the "stick viscosity" and is expressed as

$$\kappa_s = \frac{\mu \sigma_n}{2 F_f \omega R} \tag{3.5}$$

where R is the radius of a cylindrical-shaped rotary body; ω is the angular velocity of revolution; and F_f is the slip tolerance and is automatically set by Abaqus by default.

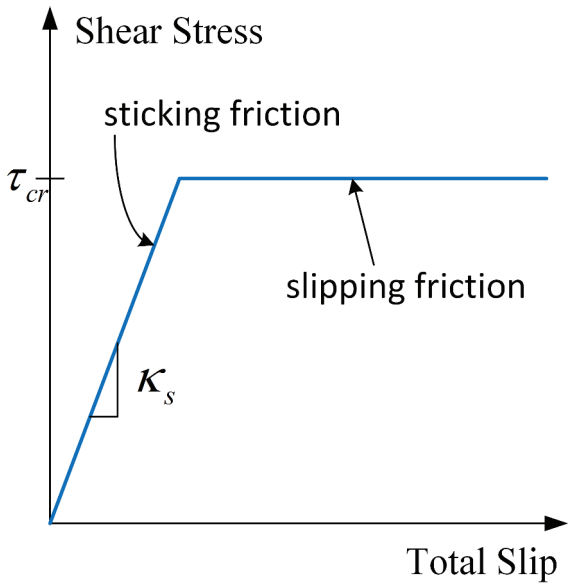

Figure 3.4: Shear traction versus elastic slip relationship for sticking and slipping friction.

If slip-rate-dependent data, contact-pressure-dependent data, or temperature-dependent data were available, the more sophisticated friction model could be calibrated.

3.4 Global vs. Local Response

Tire forces and moments are regarded as a global response, which is more meaningful than a local response for the purpose of a vehicle dynamics study. The stress/strain at certain material points in a tire structure, or the force in reinforcement cords, are treated as a local response. It usually requires finer mesh to obtain converged solutions for a local response than for a global response. In other words, a coarse mesh may be adequate to evaluate global results of a tire model, although the mesh is insufficient to obtain the local response. For example, the loss of accuracy of computed deformation in the bead and sidewall region does not compromise the evaluation of tire reaction forces at the wheel-hub [22]. The mesh of a model can be coarse to a certain extent to reduce the degrees-of-freedom. A trade-off between requirements for the global and local response needs to be balanced.

In summary, the strategy of tire modeling using FEM needs to be tailored and adapted for the purpose of vehicle simulation. The next chapter discusses the development and implementation of the proposed modeling methodology.

Chapter 4

Modeling and Parameterization

The basic philosophy behind the structural model of the Hoosier tire is not pursuing one-to-one mirroring between a real structure component and computer model, but rather an appropriate representation of the stiffness and mass distribution in space. The following sections expands the basic philosophy into the modeling and parameterization. The modeling strategy needs to take the parameterization into account. The modeling method determines what parameters required as input, and not every parameter can be obtained from the given tire. So the developed model must make sure its required parameters can be measured or estimated practically.

4.1 Hoosier LC0 Racing Tire Construction

4.1.1 Introduce the construction of Hoosier LC0 Racing Tire

The Hoosier LC0 6.0/18.0-10.0 tire is a bias-ply racing tire with simple geometry. The basic dimensions include the tread width, overall diameter, section width, and aspect ratio, which are 6 inches, 18 inches, 8.5 inches, and 45 percent respectively. The aspect ratio is defined as the ratio of the tire section height to the tire section width multiplied by 100. The Hoosier LC0 tire has a low aspect ratio as most other racing tires to improve the out-of-plane performance. A wheel with 10 inches rim diameter should be used correspondingly. The rim width of the wheel used in this research is 7 inches. The maximum vertical load limit for the Hoosier LC0 6.0/18.0-10.0 tire is

$250lbf$. Its recommended inflation pressure ranges from $8psi$ to $14psi$.

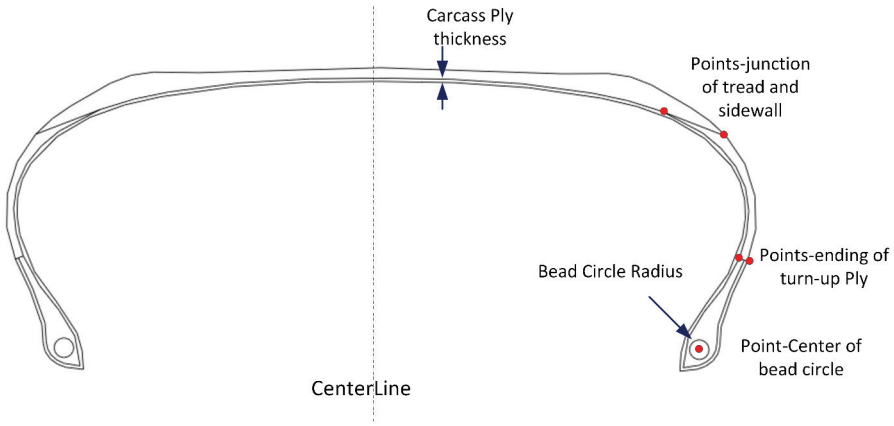

Figure 4.1: The schematic cross-section of a Hoosier LC0 6.0/18.0-10.0 racing tire. Different components are delineated.

The basic components of the tire include the carcass-ply which forms the skeleton of the whole tire structure, the tread, the sidewall, the bead filler, and a pair of beads. Figure. 4.1 depicts the cross-section of the Hoosier LC0 tire. The two-layer carcass-ply turn around and wrap up the bead fillers at two ends. A pair of beads are embedded in the bead fillers to help the tire installed on the rim flange together with a help of inner pressure. The tread is on top of the carcass-ply. The thin tread without any tread pattern is designed for good grip on dry road. The sidewalls are nothing but a thin layer of rubber compound attached on the two exterior side-faces of the carcass-ply and symmetric with respect to the tire center plane. The boundary between the tread and sidewall is not clear. There is no steel belt underneath the tread, which makes the tire flexible. Detailed structure for each component will be discussed in the following sections.

4.1.2 Mechanics associated with the construction of Hoosier LC0 tire

The Hoosier tire has several essential structural elements.

- Carcass

  The first component is the carcass which is formed by two stacked layers. Each layer is a sheet of rubber matrix with parallel cords/fibers evenly spaced and embedded in it. The cords are typically made of natural fiber, synthetic polymer, or steel. The cords are natural textile for the carcass of the Hoosier tire. Two layers are placed with a balanced crown angle which is defined as the angle

between the cords and the circumferential center line of a tire. After curing (a step in the process of tire manufacturing), the carcass forms the toroidal shape of the tire from a planar sheet. One of the functions of the carcass is holding a certain volume of pressured air. An inner lining integrated to the interior surface of the carcass is necessary to diminish its permeability. The carcass layers are turned around bead coils and folded up to a certain location of the tire sidewalls. By this way, the two ends of each single cord in a carcass are anchored on the pair of bead coils. The Hoosier tire is based on the short turning-up design as shown in Fig. 4.2(a). The other two common designs are illustrated in Fig. 4.2(b) and Fig. 4.2(c). Since the elastic modulus of the carcass cords is

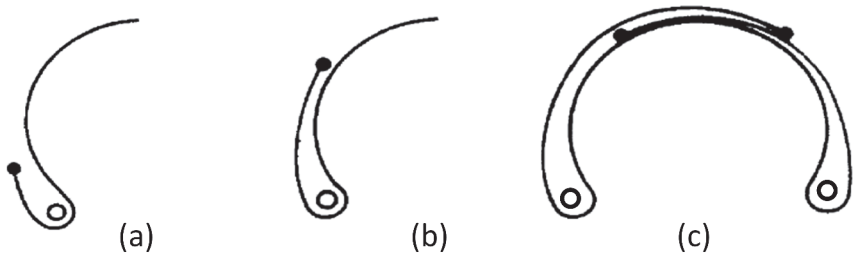

Figure 4.2: Usual forms of turn-up of a carcass. (a)Low turn-up construction; (b)High turn-up construction; (c)Overlap construction. (Reprinted courtesy of the National Institute of Standards and Technology, U.S. Department of Commerce. Not copyrightable in the United States)

typically hundred times as of the rubber matrix, the compliance of the carcass is mainly determined by the network of cords/fibers rather than the rubber. Notice that the turn-up ply does contribute extra stiffness of the sidewall.

- Bead

  The multiple-wire bead coil of the Hoosier racing tire is made from a number of turns of one-length wire as shown in Fig. 4.3. The bead coils have the wires embedded in hard rubber which is usually called bead filler, to achieve a bond within bead filler. The bead coil is stretched over the rim flange when the tire is initially installed on the wheel. This is like a bolt preload for the bead against the wheel rim. When the tire is inflated, the bead coil is further stretched reducing the preload in the radial direction on the wheel rim. At the meanwhile, inflation does push the side of bead coil laterally against the side of the rim to form an airtight seal. This mechanism is essential and a great help for a tire seating on a wheel. Also, it provides some flexibility for a tire to fit a wheel with different rim width. For example, the Hoosier LC0 tire can be seated on a 7 in or 6 in rim width wheel as long as the wheel diameter is $10in$.

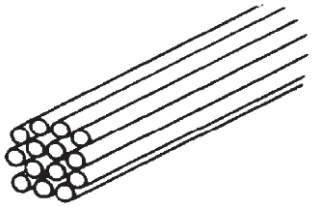

Figure 4.3: Bead coil type of Hoosier LC0 racing tire

The traction and braking forces are transmitted by the friction generated in the interface from a wheel rim flange to a tire through the function of bead coils.

- Tread

  The tread is bulk rubber on top of the crown region of a carcass and performs several functions. It is the only part having contact with the road surface for most of tires except motorcycle tires. The interaction of a tread and road surface provides all frictional forces transmitting driving, braking, and cornering forces to a vehicle. Another function of tread is to enclose and envelope small irregularities on a road surface. Extra layers of belts can be added underneath the tread of a tire to increase the bending stiffness of a carcass. There is no belt in the design of the Hoosier LC0 tire.

- Sidewall

  The sidewall is a thin layer of rubber attached to both side-faces of the tire carcass. This extra layer of rubber provides protection to the carcass plies but itself has insignificant contribution of stiffness to the whole tire structure. The dominate mechanics of tire sidewall subjected to a static vertical wheel load was studied by Hall [17]. Researchers employed special techniques to physically measure the deformation of tire sidewall under the in-plane braking [31] and out-of-plane cornering [32] conditions. These studies provided valuable information about the deformation mode of tire sidewall and associated mechanics.

The term "sidewall" in some literatures is used to refer the integrated part including both sidewall rubber and carcass plies beneath. To avoid the ambiguity, the term "sidewall section" is adopted to refer the combined part in this dissertation. The similar rule also applies to the term "tread section" and "bead section".

4.2 Geometry of the Hoosier LC0 Tire

The geometry of Hoosier LC0 tire is assumed to be 1) axi-symmetric with respect to the revolving axis and 2)reflectional symmetric to the tire center plane. The profile of a tire cross-section should be obtained from an unloaded and un-mounted tire. The method to parametrically represent the tire profile is developed based on the Hoosier racing tire but can be applied to other tires in general.

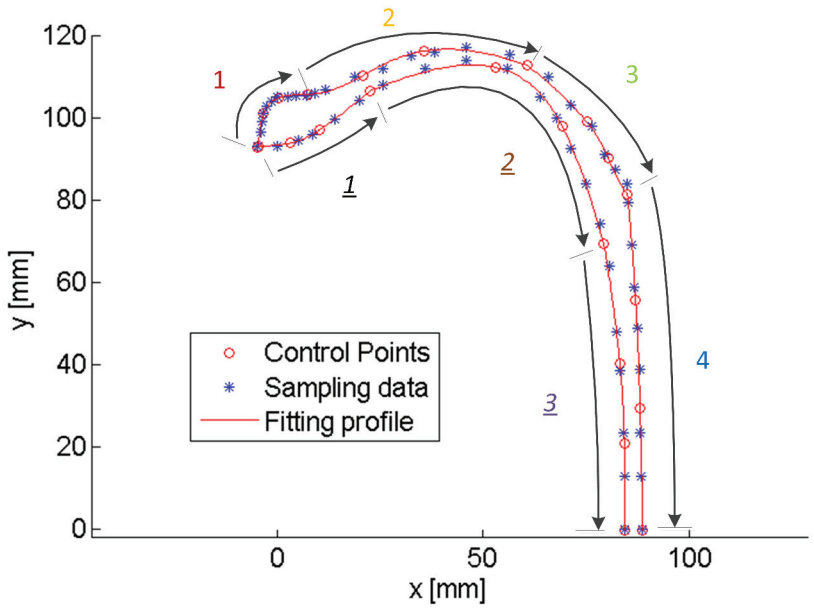

Figure 4.4: The parametric representation of the Hoosier LC0 racing tire profile

As shown in Fig. 4.4, the upper half of tire cross-section is projected on a drawing $x - y$ plane. Only half of the cross-section needs to be considered because of the reflectional symmetry. Let the x-axis lie in the tire center plane. The tire profile consists of an outer profile and inner profile. The raw description of the profile is using a series of points (x_n, y_n) which are named as "sample points" with straight line connection in between to form a curve. Mathematically, two arrays are used to store the coordinates of these sample points. One for the outer profile and the other for the inner profile. The density of sample points should be large enough to capture the curvature. The basic idea of a parametric representation of the profile is to use a few (much less than the number of sample points) of "control points" together with a third-order Lagrange interpolation polynomial to approximate the profile curves. The curve segment $C(x, y)$ is parameterized by the natural parameter $\xi \in [-1, 1]$ in

the form:

$$x(\xi) = N_1(\xi)X_1 + N_2(\xi)X_2 + N_3(\xi)X_3 + N_4(\xi)X_4 \tag{4.1}$$
$$y(\xi) = N_1(\xi)Y_1 + N_2(\xi)Y_2 + N_3(\xi)Y_3 + N_4(\xi)Y_4 \tag{4.2}$$

where $N_i(\xi), i = 1, 2, 3, 4$ refer to the four Lagrange shape functions and are visualized in Fig. 4.5. The (X_i, Y_i) are desired coordinates of the four control points to define

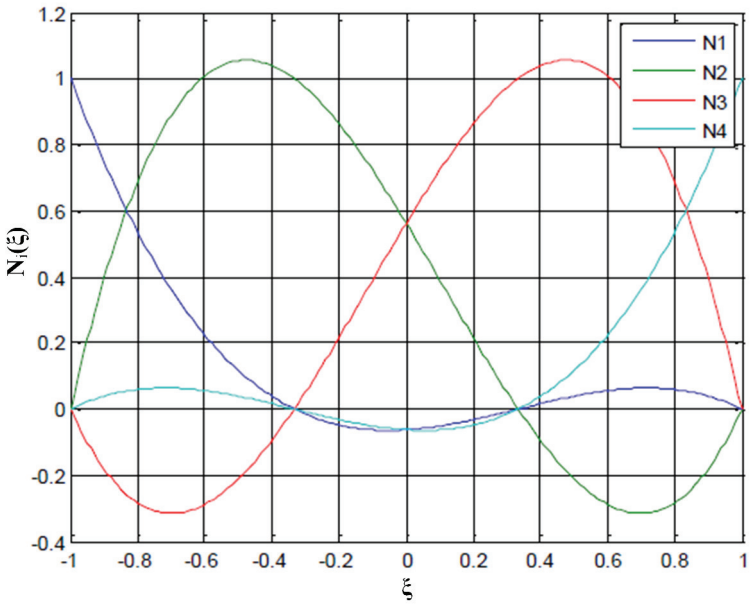

Figure 4.5: Lagrange shape functions in terms of natural coordinate ξ

the curve segment. The position of control points is determined by original sample points (x_n, y_n) under least of squares error constraint. The corresponding third-order Lagrange polynomial $C(x(\xi), y(\xi))$ to represent the curve segment can be obtained by a linear combination of the set of shape functions $N_i(\xi)$ as in Eqn. 4.1 and 4.2. Usually, it is not always accurate enough to represent the whole outer/inner profile curve with only one Lagrange polynomial. In consequence, it is appropriate to cut the whole curve into several pieces, or sub-curve, with simpler curvature. For example, in Fig. 4.4, the outer profile is divided into four pieces; and the inner profile is divided into three pieces. Each piece is parameterized by one third-order Lagrange polynomial which required four control points. The adjacent two pieces of sub-curve share one common control point. In this case, four pieces of sub-curve result in spending $13(= 4 \times 4 - 3)$ control points. Similarly, three pieces of sub-curve use $10(= 3 \times 4 - 2)$ control points. One important thing is that the control points for junction of outer and inner profiles at the bead tip should be forced the same. The control point at the intersection between the outer profile and the center plane must

be provided, the same to the intersection between the inner profile and the center plane . In addition, the y-coordinate of these two control points in the center plane should be set to zero.

A MATLAB function is developed to automatically calculate the coordinates of control points if the sample points are provided. The function prototype is

$$Function \quad [x\_bar, y\_bar] = ProfileFitting\_v2(varargin)$$

As seen from the argument list of the function, variable number of inputs can be fed into the function. Since a user already divided the outer/inner profile into several pieces, an array of the coordinates of all sample points can be correspondingly grouped into several sub-arrays. Each sub-array is a $m \times 2$ matrix that stores the x and y coordinate of sample points, where m is the number of sample points on a given sub-curve. For example, in the case of Fig. 4.4 one uses four sub-curves to represent the outer profile. Thus four sub-arrays, from *subArray1* to *subArray4*, should be prepared as inputs. Then the function is called in a form as below

$$[x\_bar, y\_bar] = ProfileFitting\_v2(subArray1, ..., subArray4)$$

The output *x_bar* and *y_bar* are x and y coordinates of all control points needed to represent the outer profile. The corresponding interpolation functions are determined at the same time in the same MATLAB function. By the same way, one can run the function again for the inner profile. Finally, the coordinates of these control points can be fed into Abaqus CAE as input parameters for geometry generation.

4.3 Functional Decomposition of the Hoosier LC0 Tire

The stiffness distribution of the tire structure affects almost every aspect of full tire performance. The stiffness matrix in the equation of motion plays a key role for a good representation of the stiffness distribution. The Hoosier LC0 tire was divided into several sections such as tread section, sidewall section, and bead section as illustrated in Fig. 4.6. Each section defined here includes all structural components(rubber and reinforcement layers). This decomposition is based on the stiffness distribution and the components' function in tire mechanics as discussed in Section 4.1.2.

It is noted that the construction of the sidewall section is neither uniform over its meridian nor does it exhibit constant thickness. Therefore, the sidewall section can be further divided into three sub-sections as illustrated in Fig. 4.7. The top sidewall sub-section has the similar structural arrangement as the tread section but with thinner on-top coated rubber. The middle sidewall sub-section compared to the top sidewall sub-section is strengthened by extra reinforcement layers coming from

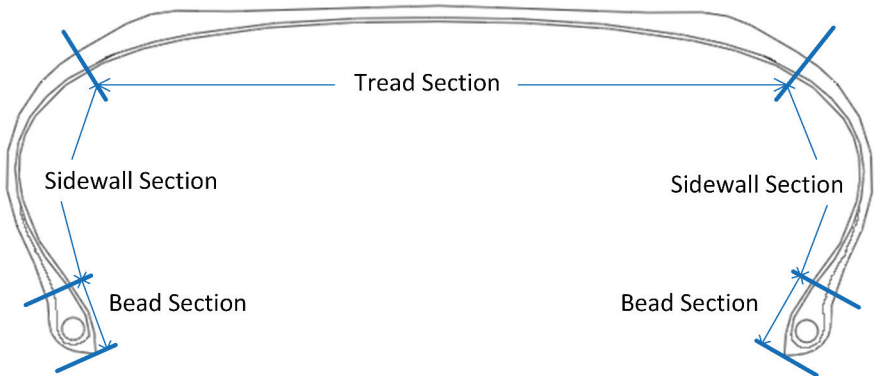

Figure 4.6: Functional decomposition of the Hoosier LC0 tire structure

the folded up carcass-ply. The root sidewall sub-section is further stiffened by the appearance of bead filler which is a kind of hard rubber in the root region of sidewall. The stiffness of the bead section is dominated by the bead coils. The elastic modulus of hard-drawn steel wires is thousands times as of bead filler rubber.

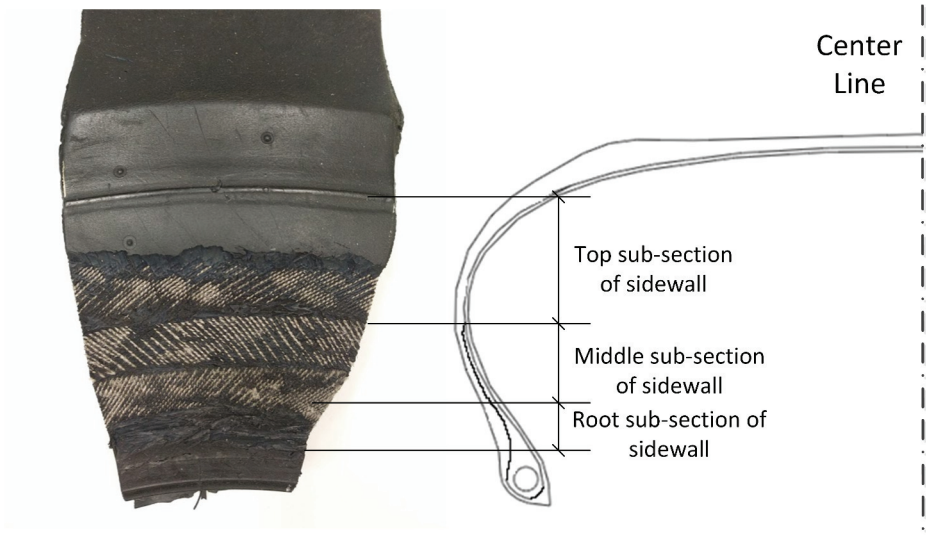

Figure 4.7: Anatomy and division of sidewall according to the stiffness distribution for Hoosier LC0 tire

The remaining work is designing a method to measure or estimate the elastic property of different tire sections, which will be discussed in Section4.4.

4.4 Hoosier LC0 Racing Tire Structure Parameterization

The representation of stiffness distribution starts from two basic questions on how to describe the elasticity of rubber and the fiber-reinforced rubber. Several constitutive models are available. It needs to be decided which one is suitable for the Hoosier tire materials and how to acquire those parameters associated with the selected model, which is a "system identification" problem. Consequentially, considerations have to cover both theory and engineering practice.

4.4.1 Model and parameterization of rubber compound

Most rubber-like materials are isotropic and have very little compressibility compared to their shear flexibility. The ratio of initial bulk modulus K_0 to initial shear modulus G_0 is used to assess the relative compressibility. This ratio K_0/G_0 can also be connected to Poisson's ratio ν by

$$\nu = \frac{3K_0/G_0 - 2}{6K_0/G_0 + 2} \tag{4.3}$$

when $K_0/G_0 \to \infty$, $\nu = 0.5$ indicates the ideal incompressibility. The numerical simulation can hardly fulfill the ideal incompressibility. Abaqus/Standard can use a hybrid formulation for almost incompressible materials with initial Poisson's ratio greater than 0.495 (i.e. $K_0/G_0 > 100$) to avoid potential convergence problems. Whereas enough compressibility must be given for the Abaqus/Explicit code to work knowing that this makes the bulk behavior of the model softer than that of the actual material. By default, Abaqus/Explicit assumes $K_0/G_0 = 20$ corresponding to Poisson's ratio of 0.475. Larger ratios cause excessively small time increments and high frequency noise into the dynamic solution in Abaqus/Explicit.

Several tread rubber samples were extracted from the Hoosier LC0 tire and prepared as in Fig. 4.8(a) for the standard uniaxial tensile test according to ASTM-D412-06a(2013). The samples are rubber material only without any reinforcement layer attached. Four samples labeled as "TR-1", "TR-2", "TR-3", and "TR-4" were tested in several sessions for various conditions. The raw data of nominal stress vs. nominal strain subjected to quasi-static cyclic loading is shown in Fig. 4.8(b) for all test sessions. Session3 was a repeat of session2 and the strain level was up to 10% for both sessions. The tested strain level was increased to 70% in session4. The overlapping of curves demonstrated a good repeatability and reliability of the testing procedure. A rich set of material behaviors appeared such as permanent set, hysteresis, and progressive damage.

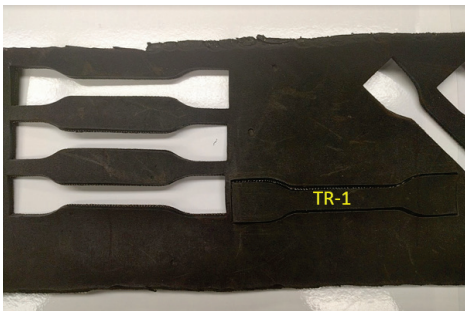

(a)

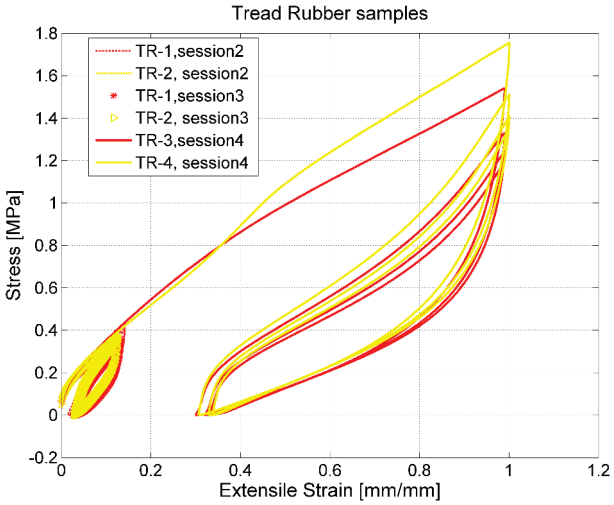

(b)

Figure 4.8: (a) One of tread rubber samples labeled in "TR" and (b) stress vs. strain behaviors.

- permanent set. For the first cycle of load and unload, upon the load return to zero the strain never goes back to zero and causes a permanent set.

- hysteresis. The mechanical behavior of rubber-like materials is known to be rate-dependent and to exhibit hysteresis upon cyclic loading. It can be observed that after a few of cycles the stress-strain curve is stabilized in a loop after initial exercising. The region enclosed by stable cycled curves represents the hysteresis. It should be noted that the hysteresis still appears even under very low rate of strain as in the present case (quasi-static, 0.0001/s). J. S. Bergstrom and M. C. Boyce developed a constitutive model to describe this nonlinear rate-dependence and relaxation behavior [33]. The dynamic viscoelasticity addresses hysteresis occurred under high rate of strain based on linear small-strain theory and is usually measured through Dynamic Mechanical Analysis. Abaqus describes the viscoelasticity in time domain by Prony series expansion of the dimensionless relaxation modulus. The large-deformation behavior of rubber is defined by a hyperelastic material model which will be fully discussed in following. And the rate-dependent behavior is defined by incorporating the relaxation coefficients into the strain energy function for hyperelastic material.

- progressive damage. The material is softened after the initial loading. The energy dissipated in the first cycle before rubber-like material getting into a stable state is caused by so-called progressive damage. Progressive damage is also associated with Mullins effect. The Mullins effect is a particular aspect of the mechanical response in filled rubbers in which the stress-strain curve

depends on the maximum loading previously encountered. The phenomenon can be idealized as an irreversible softening of the stress-strain curve that occurs whenever the load increases beyond its prior all-time maximum value under quasi-static cyclic loading. A number of constitutive models have been proposed to describe the effect. For example, the Ogden-Roxburgh model [34] is used in several commercial finite element codes including Abaqus. An idealized Mullins effect ignores the phenomenon appeared in real practice e.g. some permanent set upon unloading and/or viscoelastic effects such as hysteresis.

By so far there is no such a theory can handle all these phenomenons by an uniform model. As the current interest, we consider more about its hyperelasticity in a consistently stable material state. Therefore a single curve of stable state along the load path was selected for each sample for hyperelasticity modeling as shown in Fig.4.9.

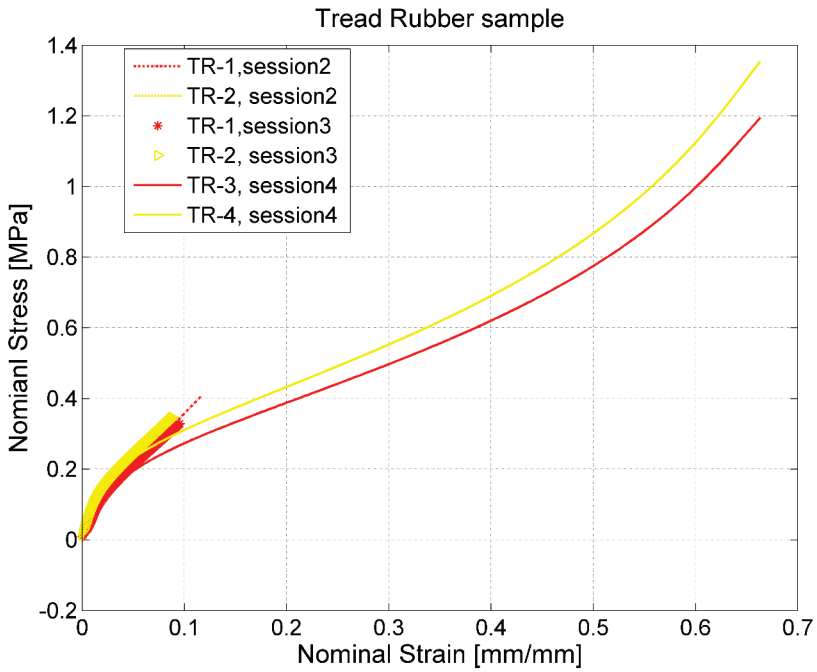

Figure 4.9: Single stress vs. strain curve for hyperelasiticity modeling. Again, the strain level for TR-1 and TR-2 up to 10%; for TR-3 and TR-4 up to 70%

The hyperelasticity formulation starts from the representation of the strain energy potential instead of direct stress-strain relationship to accommodate the highly nonlinear and nearly incompressible characteristics of rubber material. The strain energy potential, which defines the strain energy stored in the material per unit of reference volume (volume in the initial configuration) W as a function of the strain at that point in the material, is expressed in terms of three strain invariants assuming perfect incompressibility (In some references, the strain energy is formulated in

terms of deviatoric strain invariant and allows some compressibility.) In this way, the formulation becomes coordinate-system independent.

$$W = W(I_1) \quad or \quad W(I_1, I_2) \quad or \quad W(I_1, I_2, I_3) \tag{4.4}$$

in which the first strain invariant I_1 is defined as

$$I_1 = \lambda_1^2 + \lambda_2^2 + \lambda_3^2 \tag{4.5}$$

where $\lambda_i, i = 1, 2, 3$ are the principal stretches. The second and third strain invariant are

$$I_2 = \lambda_1^{-2} + \lambda_2^{-2} + \lambda_3^{-2} \tag{4.6}$$

$$I_3 = \lambda_1 \lambda_2 \lambda_3 \tag{4.7}$$

A general stress-strain relationship can be derived from the strain energy form of Eq. (4.4) for various deformation modes. Assuming a homogeneous rubber cube with unit dimensions, the difference between any pair of principal stresses can be derived. Let σ_i are the Cauthy stress on a surface normal to the i^{th} principal direction, then the change of strain energy of that cube dW is

$$\begin{aligned} dW &= \sigma_1 \lambda_2 \lambda_3 d\lambda_1 + \sigma_2 \lambda_3 \lambda_1 d\lambda_2 + \sigma_3 \lambda_1 \lambda_2 d\lambda_3 \\ &= \sigma_1 d\lambda_1/\lambda_1 + \sigma_2 d\lambda_2/\lambda_2 + \sigma_3 d\lambda_3/\lambda_3 \end{aligned} \tag{4.8}$$

with an ideal incompressibility assumption that

$$\lambda_1 \lambda_2 \lambda_3 = 1 \tag{4.9}$$

Also, because of Eq.(4.9) $d\lambda_i$ are not mutually independent but subject to a relation

$$d\lambda_1/\lambda_1 + d\lambda_2/\lambda_2 + d\lambda_3/\lambda_3 = 0 \tag{4.10}$$

We may set one of $d\lambda_i$ equal to zero, say

$$d\lambda_1 = 0 \tag{4.11}$$

And the total differential dW is

$$\begin{aligned} dW &= \frac{\partial W}{\partial \lambda_1} d\lambda_1 + \frac{\partial W}{\partial \lambda_2} d\lambda_2 + \frac{\partial W}{\partial \lambda_3} d\lambda_3 \\ &= \frac{\partial W}{\partial \lambda_2} d\lambda_2 + \frac{\partial W}{\partial \lambda_3} d\lambda_3 \end{aligned} \tag{4.12}$$

By comparing to Eq.(4.8) under the same condition of $d\lambda_1 = 0$, we arrive

$$\frac{\partial W}{\partial \lambda_2} d\lambda_2 + \frac{\partial W}{\partial \lambda_3} d\lambda_3 = \sigma_2 d\lambda_2/\lambda_2 + \sigma_3 d\lambda_3/\lambda_3 \tag{4.13}$$

Applying Eq.(4.10) and (4.11) into Eq.(4.13), it is found the difference between a pair of principal stresses

$$\sigma_3 - \sigma_2 = \frac{\partial W}{\partial \lambda_3}\lambda_3 - \frac{\partial W}{\partial \lambda_2}\lambda_2 \tag{4.14}$$

Instead of Cauthy stress, a nominal stress T_i is usually expressed as force per unit area relative to the initial undeformed state. Considering the force acting on the i^{th} normal surface, we have $\sigma_i\lambda_j\lambda_k = T_i \cdot 1 \cdot 1$ $(i \neq j \neq k)$ which leads to

$$\sigma_i = \lambda_i T_i \tag{4.15}$$

Substitute Eq.(4.15) to Eq.(4.14), we arrive

$$\lambda_3 T_3 - \lambda_2 T_2 = \frac{\partial W}{\partial \lambda_3}\lambda_3 - \frac{\partial W}{\partial \lambda_2}\lambda_2 \tag{4.16}$$

Similarly, by setting $d\lambda_2 = 0, d\lambda_3 = 0$ respectively two remaining relations are

$$\lambda_2 T_2 - \lambda_1 T_1 = \frac{\partial W}{\partial \lambda_2}\lambda_2 - \frac{\partial W}{\partial \lambda_1}\lambda_1 \tag{4.17}$$

$$\lambda_1 T_1 - \lambda_3 T_3 = \frac{\partial W}{\partial \lambda_1}\lambda_1 - \frac{\partial W}{\partial \lambda_3}\lambda_3 \tag{4.18}$$

The term $\partial W/\partial \lambda_i$ can be further expanded via chain rule (using index notation)

$$\frac{\partial W}{\partial \lambda_i} = \frac{\partial W}{\partial I_p}\frac{\partial I_p}{\partial \lambda_i} \tag{4.19}$$

Furthermore, after using the relationship between stretches and nominal strains $\lambda_i = 1 + \epsilon_i$, the nominal stress versus nominal strain relationship is obtained. The term $\partial W/\partial I_p$ in Eq. (4.19) has various expansions for different strain energy potential forms.

The most common strain energy potential forms include the neo-Hookean, Mooney-Rivlin, and Yeoh form. The following analysis focuses on determining the most suitable hyperelastic form for Hoosier LC0 tread rubber compound.

4.4.1.1 Neo-Hookean form

The neo-Hookean form features simplicity of phenomenological formulation by just involving the effect of first strain invariant in its first order as

$$W(I_1) = C_{10}(I_1 - 3) \tag{4.20}$$

where C_{10} is a constant. The importance of the neo-Hookean form lies in the coincident relation to the Gaussian statistical model based on the cross-linked network of rubber which leads to the Eq. 4.21.

$$W = (1/2)NkT(I_1 - 3) \tag{4.21}$$

where N is the number of network chains per unit volume, k and N are the Boltzmann constant and temperature respectively. By comparing Eq. (4.20) and (4.21), they addresses the same form as $C_{10} = (1/2)NkT$.

For uniaxial tension or compression deformation modes, let the load along the first principal direction thus $T_1 \neq 0$ but $T_2 = T_3 = 0$. The consequent kinematics says $\lambda_1 = \lambda$, and $\lambda_2 = \lambda_3 = 1/\sqrt{\lambda}$ since the incompressibility. Substituting these expressions into Eq. (4.17), it reads

$$T_1 = 2(\lambda - \lambda^{-2})\frac{\partial W}{\partial I_1} = 2(\lambda - \lambda^{-2})C_{10} \tag{4.22}$$

Notice that for the neo-Hookean form $\partial W/\partial I_1 = C_{10}$. Equation (4.22) is the stress-strain relationship. Later, we will see it is just a special case of the stress-strain relationship derived under the Mooney-Rivlin form.

4.4.1.2 Mooney-Rivlin form

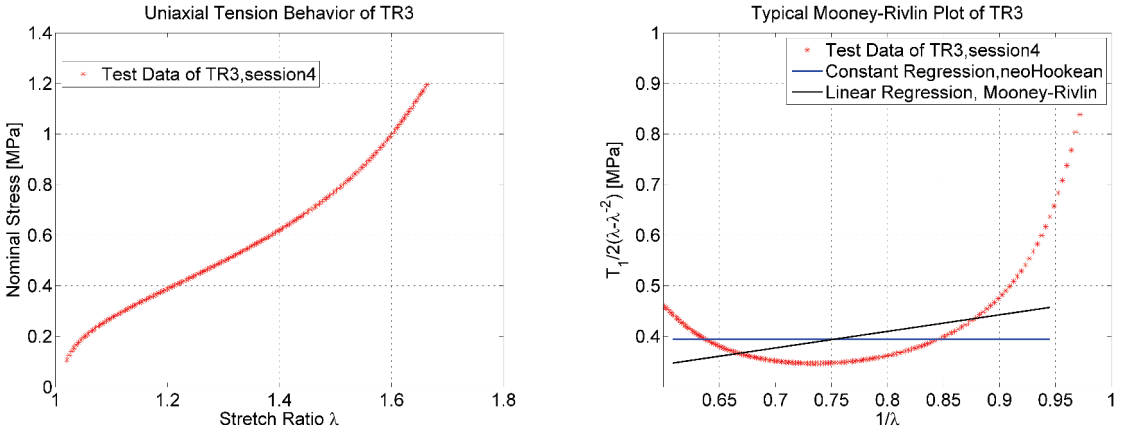

(a) (b)

Figure 4.10: Neo-Hookean and Mooney-Rivlin form representation in a typical Mooney-Rivlin plot. (a) Original nominal stress vs. stretch test data of tread rubber sample TR-3. (b) Regressions of neo-Hookean and Mooney-Rivlin form in a typical Mooney-Rivlin plot.

The Mooney-Rivlin form considers both the contribution of I_1 and I_2 to the elastic strain energy up to their first order.

$$W(I_1, I_2) = \frac{\partial W}{\partial I_1}(I_1 - 3) + \frac{\partial W}{\partial I_2}(I_2 - 3) = C_{10}(I_1 - 3) + C_{01}(I_2 - 3) \tag{4.23}$$

For uniaxial tension or compression mode, the stress-strain relationship is

$$T_1 = 2(\lambda - \lambda^{-2})(\frac{\partial W}{\partial I_1} + \frac{1}{\lambda}\frac{\partial W}{\partial I_2}) = 2(\lambda - \lambda^{-2})(C_{10} + \frac{1}{\lambda}C_{01}) \tag{4.24}$$

The constants C_{10}, C_{01} need to be estimated from real test data in uniaxial or compression deformation modes. Rivlin manipulated Eq. (4.24) to a new form

$$\frac{T_1}{2(\lambda - \lambda^{-2})} = C_{10} + \frac{1}{\lambda} C_{01} \tag{4.25}$$

If $1/\lambda$ is treated as an independent variable and $T_1/2(\lambda - \lambda^{-2})$ as a dependent variable, their relationship in a graphic representation is the so-called typical Mooney-Rivlin plot. The neo-Hookean constitutive relation as Eq. (4.22) converts to a constant line which stands for C_{10} in a typical Mooney-Rivlin plot. The Mooney-Rivlin constitutive relation states a linear relationship indicated by Eq. (4.25) in a Mooney-Rivlin plot. The intercept and slope of a regression line equals C_{10} and C_{01} respectively. As an example, the test data of tread rubber was firstly reformed from Fig. 4.10(a) to a typical Mooney-Rivlin plot in Fig. 4.10(b). The parameter estimation of neo-Hookean and Mooney-Rivlin models were completed by a constant regression (straight line in blue) and a linear regression (straight line in black) of the test data (red dots) in the Mooney-Rivlin plot as shown in Fig.4.10(b). The regression results show that the data does not agree well with a linear relationship at all over the full strain range.

It could be argued that the regression should be emphasized over the lower stretch range(towards large value of $1/\lambda$). However, if the parameter estimation only relies on the data in the low stretch range (λ close to 1, small strain range) without considering the data reaching higher stretch may lead to an unstable hyperelastic model. As in

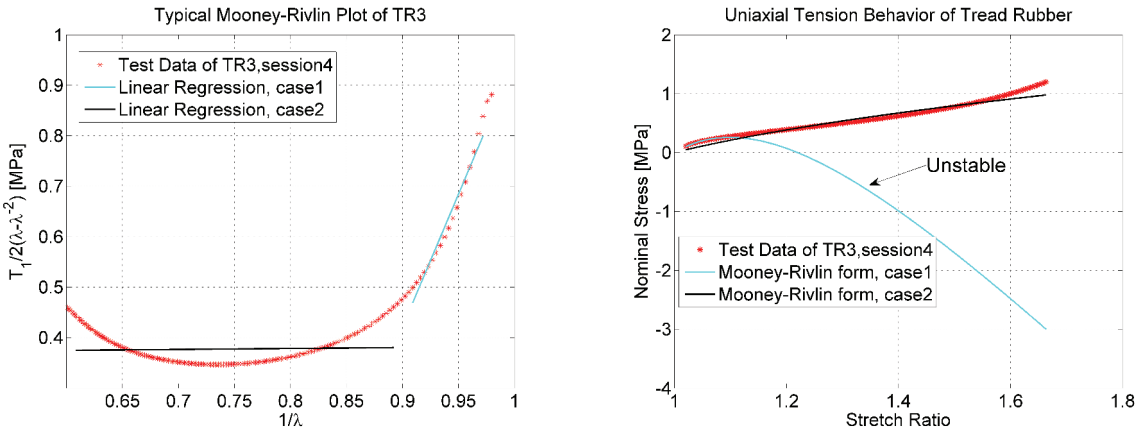

(a) (b)

Figure 4.11: Parameter estimation of Mooney-Rivlin model depends on two different stretch ranges. (a) Calibrations of Mooney-Rivlin model depends on two different stretch ranges (b) Corresponding model behaviors for a given calibration result.

Fig. 4.11(a), the straight line in cyan is a linear regression of data covering the stretch range $\lambda \in (1, 1.09)$ which corresponds to $1/\lambda \in (0.91, 0.98)$. The estimated parameters C_{10}, C_{01} give a predictive stress-strain curve in cyan shown in Fig. 4.11(b).

Notice that the prediction in the range $\lambda \in (1, 1.09)$ is of course accurate. However, when the stretch exceeds 1.1 its trend deviates from the test data in an opposite way and becomes non-physical. This situation may happen if we only had the test data covering small stretch range just like testing cases of TR-1 and TR-2 in the test session2&3. The lesson learned is that even a rubber-like material is only exercised in a small strain range for its particular application, the test for material characterization must cover enough strain range for obtaining reasonable parameters of a constitutive model. As a contrast, the regression results indicated by the lines in black in Fig. 4.11 loses some accuracy over the small stretch range but captures the dominant hyperelastic behavior over the large stretch range.

It is obvious that neither neo-Hookean nor Mooney-Rivlin form has a good representation of the elasticity of Hoosier tread rubber over the large strain range. One inherent reason is Mooney-Rivlin form embeds an assumption that $\partial W/\partial I_1 = C_{10} = const, \partial W/\partial I_2 = C_{01} = const$ in Eq. (4.23). But this assumption does not generally hold. Rivlin & Saunder and Obata, Kawabata & Kawai [35] found that neither $\partial W/\partial I_1$ nor $\partial W/\partial I_2$ is constant. The next step is to seek a better hyperelastic model.

4.4.1.3 Yeoh form

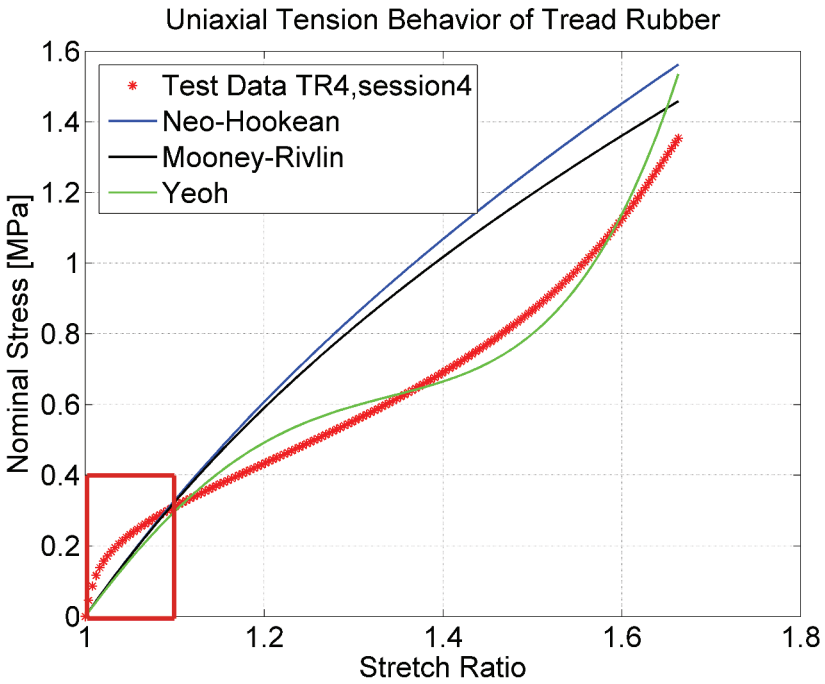

Figure 4.12: Prediction performance of the candidate hyperelastic models against the test data

Table 4.1: The estimated coefficients for the candidate hyperelastic models. The statistics to evaluate the performance of each model against the test data is summarized

Hyperelastic Model	C_{10}	C_{20}	C_{30}	C_{01}	Mean of Residual	Standard Deviation of Residual
	Unit: [MPa]					
neo-Hookean	0.6	N/A	N/A	N/A	0.24	0.16
Mooney-Rivlin	0.5	N/A	N/A	0.09	0.19	0.13
Yeoh	0.566	-0.422	0.229	N/A	0.0008	0.056

An agreement among the literatures is that $\partial W/\partial I_1$ is generally much greater than $\partial W/\partial I_2$. Yeoh [36] suggested to neglect $\partial W/\partial I_2$ and make it zero, which does not cause any serious error. Moreover, Yeoh highlighted the contribution of I_1 by considering its effect up to third order. The leading terms of strain energy potential are now

$$W(I_1) = C_{10}(I_1 - 3) + C_{20}(I_1 - 3)^2 + C_{30}(I_1 - 3)^3 \tag{4.26}$$

which is a cubic function of $(I_1 - 3)$ and referred to as the Yeoh form. The emphasis on I_1 originates in the Gaussian model Eq. (4.21) based on statistical theory. The uniaxial tensile nominal stress-strain relation becomes

$$T_1 = 2(\lambda - \lambda^{-2})\left[C_{10} + 2C_{20}(I_1 - 3) + 3C_{30}(I_1 - 3)^2\right] \tag{4.27}$$

The parameters C_{10}, C_{20}, C_{30} can be estimated through a least-squares curve fitting procedure. The following error defined as Eq. (4.28) is minimized.

$$Error = \sum_{i=1}^{n}(1 - T_i^{theory}/T_i^{test})^2 \tag{4.28}$$

where T_i^{theory} is a theoretical stress expression and T_i^{test} is a stress value from the test data. Figure. 4.12 shows a comparison of the performance among three candidate models. The estimated coefficients for each model is listed in Table. 4.1. It is worth addressing the importance of C_{10} again because of its physical meaning in the Gaussian statistical hyperelastic model. C_{10} plays the dominant role for all three models, thus its value in those models should be similar as expected. The degree of discrepancy to the test data will vary with the strain range to be modeled, the nonlinearity of the material, and the particular hyperelastic form being employed. Looking closely into the small strain ($\lambda < 1.1$) region highlighted by a rectangular frame in Fig. 4.12, all three models have the similar initial elastic modulus but still deviate from the test data a little bit. It is obvious that only the Yeoh model is capable of capturing the first and second turn of measured stress-strain curve over the full strain range. The Yeoh model has the best prediction among three candidates.

Several comments are given as 1) beside the uniaxial tension which is the most common test, other homogeneous deformation modes e.g. equibiaxial tension, planar tension (pure shear), and volumetric compression tests are used to characterize the material parameters. It is best to utilize data from various deformation modes to estimate model parameters and identify the best material model. 2) However, if uniaxial tension mode is the only available data, Yeoh form has better predictive performance than neo-Hookean and Mooney-Rivlin forms for various deformation modes. 3) Users may put more weights on the small strain region for a parameter estimation procedure. It leads to accurate prediction in this region for a given model, but has the potential for large discrepancies at higher strain range or even worse non-physical behavior beyond a certain strain level.

4.4.2 Model and parameterization of fiber-reinforcement layer

The analysis of cord reinforced composites imposes challenges to characterize the highly anisotropic behavior. The anisotropic property of laminated fiber-reinforced rubber layers in a tire is induced by a different spatial orientation arrangement of parallel cords. The traditional treatment of elasticity of cord-rubber laminates "utilizes the overall elastic stiffnesses of both the cords and rubber treated as a two-dimensional orthotropic material." It is much more convenient to work with an average property. This requires that the cord spacing should be much less than the dimensions of a layer of cord-rubber composite. A modern method is introduced by Helnwein et. al.

4.4.2.1 Helnwein's model

Helnwein et al. [27] proposed an approach which is termed as "rebar layer". The "rebar layer" provides a mechanical description of different constituents in the framework of large-strain theory, and conducts geometrical and constitutive nonlinear analysis of cord-reinforced rubber composite. All shortcomings resulting from homogenization of different materials to a "mechanically equivalent medium" are coped with using the "rebar layer" concept. The main features of the proposed method include 1)the different constituents (several unidirectional laminate and the rubber matrix) are represented separately; 2)the states of true stress are obtained separately in the different plies and in the rubber; 3)experimentally obtained material parameters for the individual components may be fed into the model directly as input parameters. The last feature provides great convenience for material characterization from the consideration of experiment design.

The constitutive behavior of a broad class of cord materials undergoing large deformation and strain can be described similarly by means of the hyperelastic formulation. The fiber-reinforced rubber elasticity is characterized by a function of stored strain

energy potential $\widetilde{W}$. Then the total strain energy form W of fiber-reinforced rubber layer is

$$W(\mathbf{C}) = U(J) + \widetilde{W}(\mathbf{C}) = U(J) + \widetilde{W}(\lambda_R, \lambda_L) \tag{4.29}$$

where $\mathbf{C}$ is the right Cauchy-Green tensor, J is the total volume ratio of rubber matrix. The term $U(J)$ is the strain energy potential due to the rubber matrix and $\widetilde{W}(\mathbf{C})$ is the strain energy potential induced by reinforce fibers; λ_R, λ_L denote the axial and the lateral stretch of a uniaxially stressed fiber. The strain energy potential $\widetilde{W}$ can be further expressed in terms of stretches of fibers along principal directions i.e. $\widetilde{W} = \widetilde{W}(\lambda_R, \lambda_L)$. The stress-strain relation of the rebar layer can be derived from Eq. (4.29) but details are not presented here.

4.4.2.2 Sample preparation of tread section

It is not always feasible to separate the desired component from a tire product in practice. For example, extracting a thread of textile fiber from the rubber matrix in a reinforcement layer is nearly impossible to make a usable test sample. Similarly, a thin layer of rubber matrix is even harder to make it a sample from an existing tire. The repeatability of testing results also need to be guaranteed for the samples in the same kind. A possible solution is extracting a group of "sandwich" samples which contain the tread and carcass together instead of single material component from the Hoosier LC0 tire. The mechanical behavior of this kind of "sandwich" sample affects the global tire behavior through a more direct way than a single material component. Characterizing the "sandwich" sample meets the needs of pursuing global response. However, a new method of characterization needs to be developed, since no single material law can apply to the "sandwich" sample.

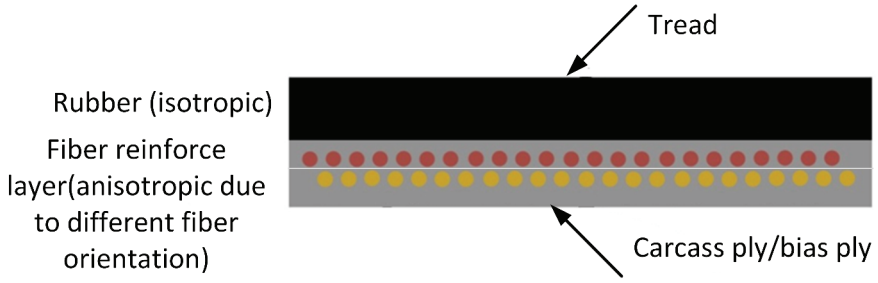

Figure 4.13: The cross-section of crown region of Hoosier LC0 6.0/18.0-10.0 tire. The thickness of two layers of carcass ply is exaggerated to show the arrangement of reinforcement fibers.

The cross-section of crown region of the Hoosier LC0 tire is illustrated as Fig.4.13. The crown section can be divided into the tread and carcass. The carcass consists of two layers of bias ply. The direction of fibers (unidirectional) on each layer is described

by the crown angle which is the angle between the fiber and the circumferential center line of the tire. For the Hoosier LC0 tire, the crown angles are $\pm 30 deg$ respectively. When the fibers have a low crown angle, the tire will have good cornering performance but sacrifice the ride comfort. The low crown angle also gives rigidity to support the tread. That is a reason that belts are not necessary for a bias-ply tire.

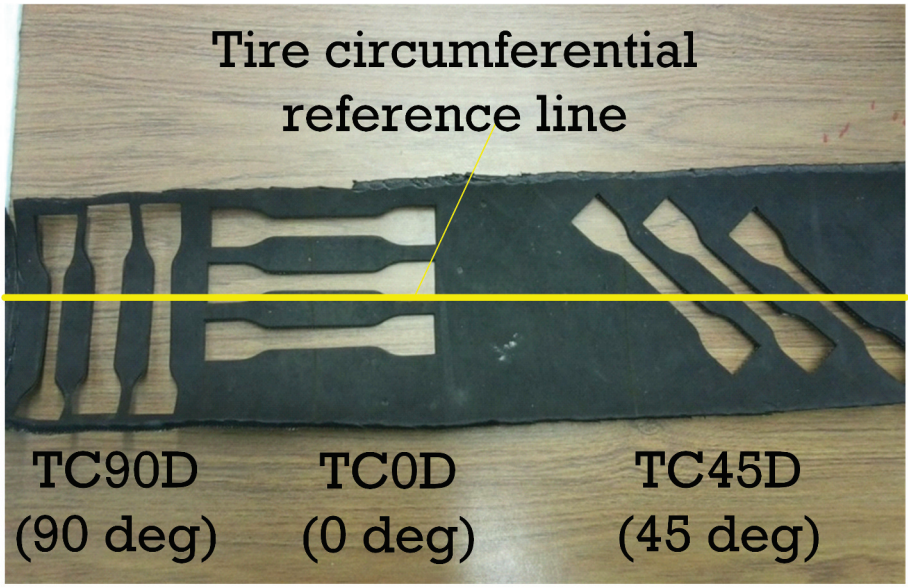

Figure 4.14: Three types of sandwich sample were extracted from the crown region of Hoosier LC0 6.0/18.0-10.0 tire, and each type of sample included three specimens.

A strip of crown region was cut from the Hoosier LC0 tire. Three different kinds of "sandwich" samples were extracted as shown in Fig. 4.14. The dog-bone shaped samples were distinguished by their relative position angles between the centerline of a sample's geometry and the circumferential centerline of the tire crown. The three types of samples were labeled as "TC0D", "TC45D" and "TC90D" respectively, which corresponds to the relative position angles being 0, 45, and 90 in degrees relative to the circumferential centerline of the tire crown. It should be noted that these position angles have nothing to do with the fiber angles in the underlying carcass ply. For each type of sample, three specimens were extracted to check the repeatability of test data. The purpose of preparing several types of samples is to activate different deformation modes of samples caused by fiber arrangement. Figure 4.15 depicts the fiber orientation in each layer for three types of sample. The "TC0D" sample has $\pm 30 deg$ fiber angles with respect to the centerline of sample; the "TC90D" sample is with $\pm 60 deg$ fiber angles. These two types of sample primarily affect the longitudinal and lateral behavior of a tire. The "TC45D" sample has $15 deg$ fiber angle for one layer, and $105 deg$ fiber angle for the other layer. So the layers are not balanced for the "TC45D" sample.

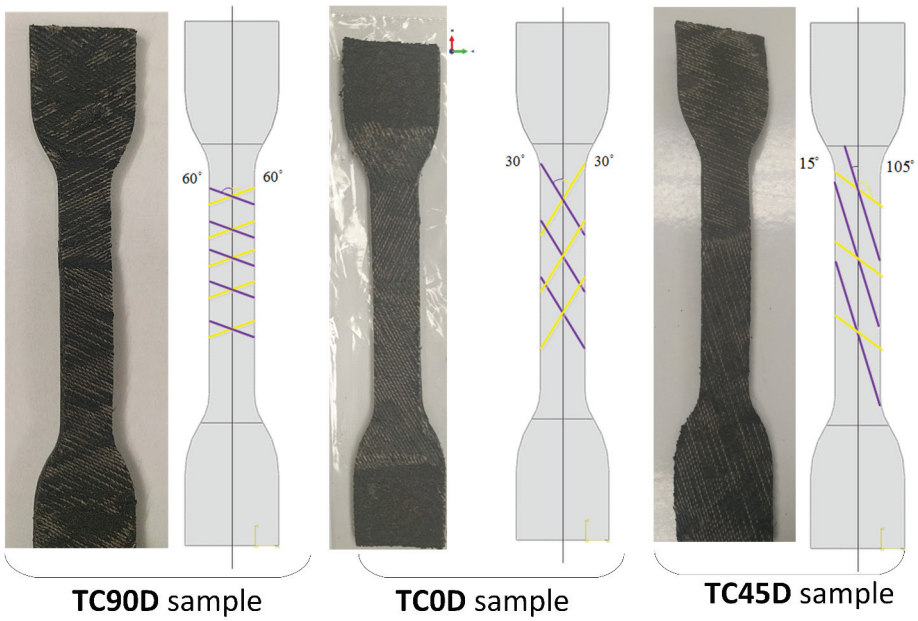

Figure 4.15: The fiber arrangement in each layer of carcass ply for each type of sample. Sample TC90D and TC0D were anatomized to reveal the fiber angles

These dog-bone shaped samples went for quasi-static tensile tests in the INSTRON load frame at Virginia Tech.

4.4.2.3 Method of characterizing "sandwich" sample

Since not all of the material properties of the "sandwich" sample can be directly measured, the basic idea behind the proposed method of characterization is estimating the model parameters by minimizing the difference between a virtual test and a physical test through optimizations.

TC0D and TC90D samples are selected to perform physical tensile tests. The load-displacement relation of both samples are preferred for parameter estimation instead of stress-strain relation. The load vs. displacement has the physical scales of the applied load subject to the given displacement on the sample level, but the stress vs. strain relation does not because it is normalized.

The corresponding finite element models for each type of sample are then created. The constitutive relation of the FE sample model is a combination of the Yeoh and Helnwein's model. The isotropic tread rubber is modeled in the Yeoh form. The carcass layer is suitable to be modeled as a membrane with reinforcement bars based on Helnwein's theory because the bending stiffness of the carcass-ply can be neglected. Some of the parameters involved in the "rebar layer" model, such as the fiber orientation and spacing between fibers, can be directly measured in advance after physically

tearing the reinforcement layer apart. The elasticity of tread rubber has been obtained as in Section 4.4.1.3 and the elastic property of the rubber matrix of carcass ply is assumed being the same. Only the elastic modulus of reinforcement fiber remains to be estimated. After imposing proper boundary and loading conditions, a virtual test corresponding to the physical tensile test can be carried out given a set of parameters.

The general formulation of the optimization problem is summarized as below. Let $\mathbf{x} = (x_1, x_2, x_3, \ldots, x_M)^T$ be a column vector containing parameters to be estimated. The inverse problem for estimation of model parameters is minimizing the objective function $f(\mathbf{x})$,

$$\min_{\mathbf{x}} \left\{ f(\mathbf{x}) = \sum_i (Error_i)_{L-\delta} \right\} \tag{4.30}$$

subject to $g_j(\mathbf{x}) \geq 0$. where i is the number of types of sample being tested for calibration. In this case, $i = 1$ for the TC0D sample and $i = 2$ for the TC90D sample; For the n pairs of load vs. deflection data, the error $(Error)_{L-\delta}$ is defined as the squared difference of the load-displacement curve between the virtual and real test as in Eq. 4.31;

$$(Error)_{L-\delta} = \sum_{k=1}^{n} (L_k^{model} - L_k^{test})^2 \tag{4.31}$$

L_k^{model} is a load value from the model in the virtual tests, and L_k^{test} is a load value from the real test. j in $g_j(\mathbf{x})$ is the number of inequality constraints and each inequality constraint relates to the setting of upper or lower bound to make sure the parameters are physically meaningful. The "best" estimation of material parameters can be achieved in the sense of Least Mean Square by solving this optimization problem.

A scheme is designed to involve Abaqus, Python, and MATLAB environment in a optimization loop (see Fig. 4.16) to automatically solve the problem stated in Eqn. (4.30). The optimization process runs iteratively within this loop. Given a set of initially guessed parameters, Abaqus conducts one virtual tension test for the sample TC0D and TC90D respectively. Then a Python script is used to extract the load-displacement curve from the simulation results of Abaqus. A series of tasks are completed in a MATLAB environment: 1) computing the difference between the simulation and the real test curve of load vs. displacement; 2)searching the next point in the parameter domain to reduce the difference in an optimal way; and 3)sending a new set of parameters to Abaqus to do the next virtual test. The iterations continue to run until the value of the objective function getting below a certain tolerance. Finally, the "best" estimation is obtained.

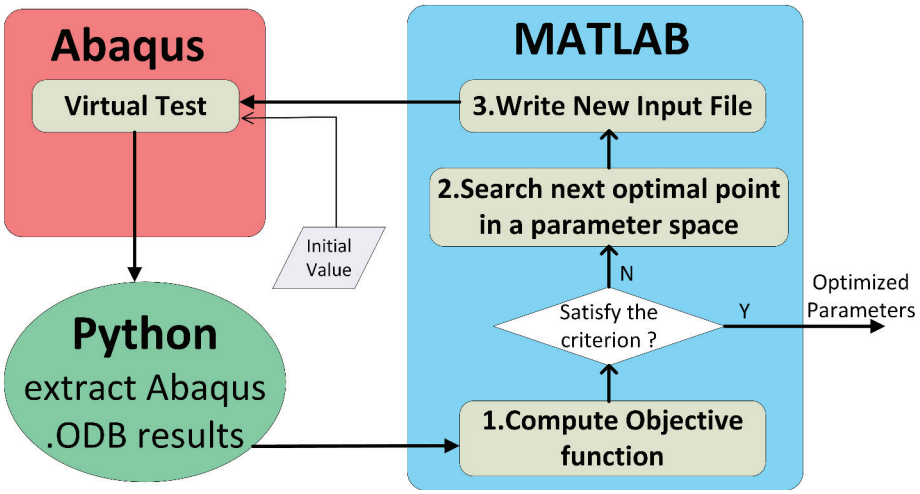

Figure 4.16: The scheme of process to estimate a set of parameters of a model through optimization.

4.4.3 Parameterization of tread section

The dogbone-shaped tread section sample models of TC0D and TC90D were calibrated by the tensile test data. The measured geometric parameters and estimated elastic parameter of reinforcement fibers through the proposed optimization process are summarized in Table. 4.2. The predicted load-displacement curves from simulations are compared to tests as in Fig. 4.17(a) and (b) for the sample TC0D and TC90D respectively.

Table 4.2: The parameters value of reinforcement fiber.

Name	cross-section area	spacing	elastic modulus
Unit	in^2	in	psi
	$4.38e-4$	0.033	$4.95300e5$

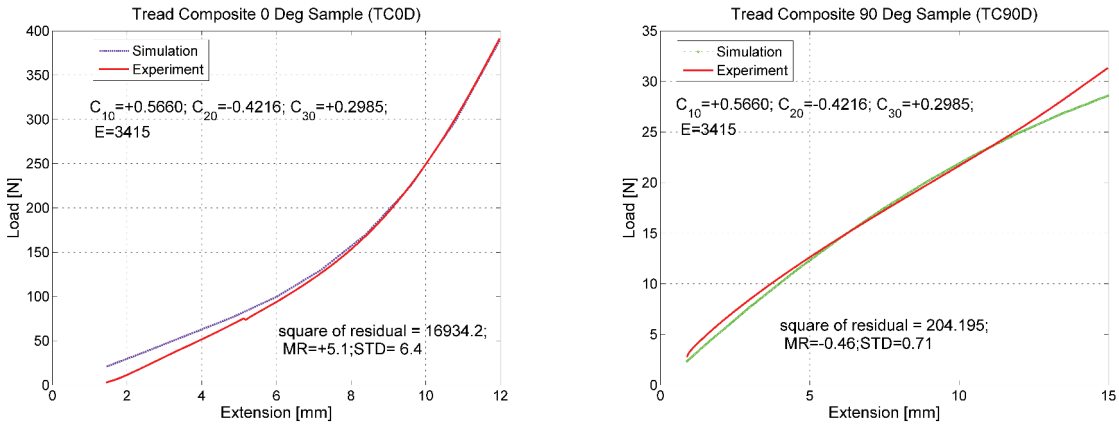

(a) (b)

Figure 4.17: Calibration results of tread composites model based on the uniaxial tension test (a) for TC0D and (b) for TC90D. Statistics of comparison between the simulation and test are also labeled, where "MR" stands for Mean of Residual and "STD" abbreviates Standard Deviation of residual.

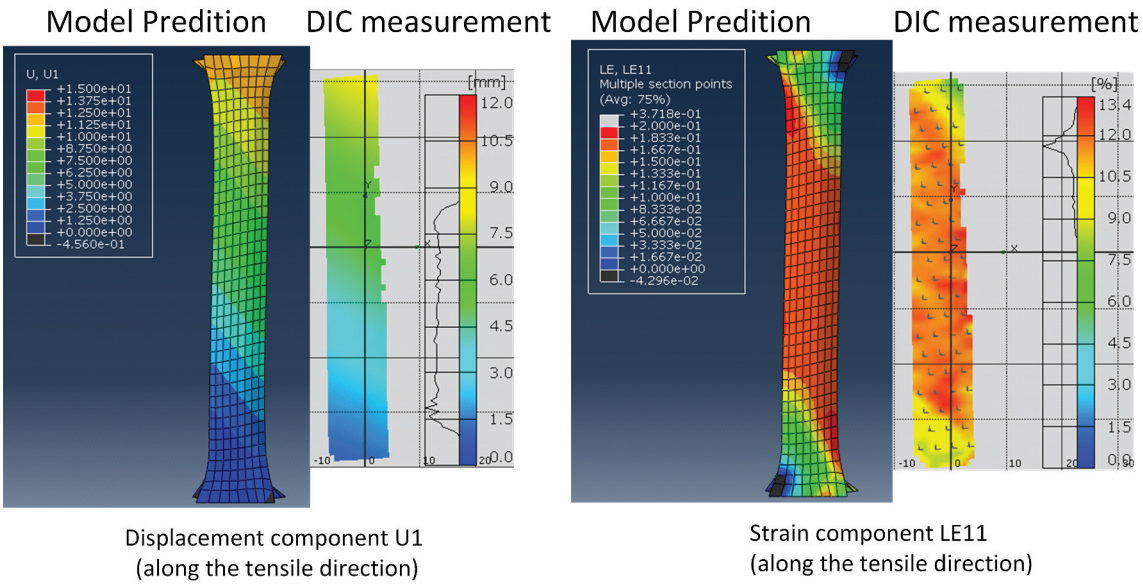

Figure 4.18: Displacement and strain fields comparison between the simulation and DIC measurement for the sample TC0D.

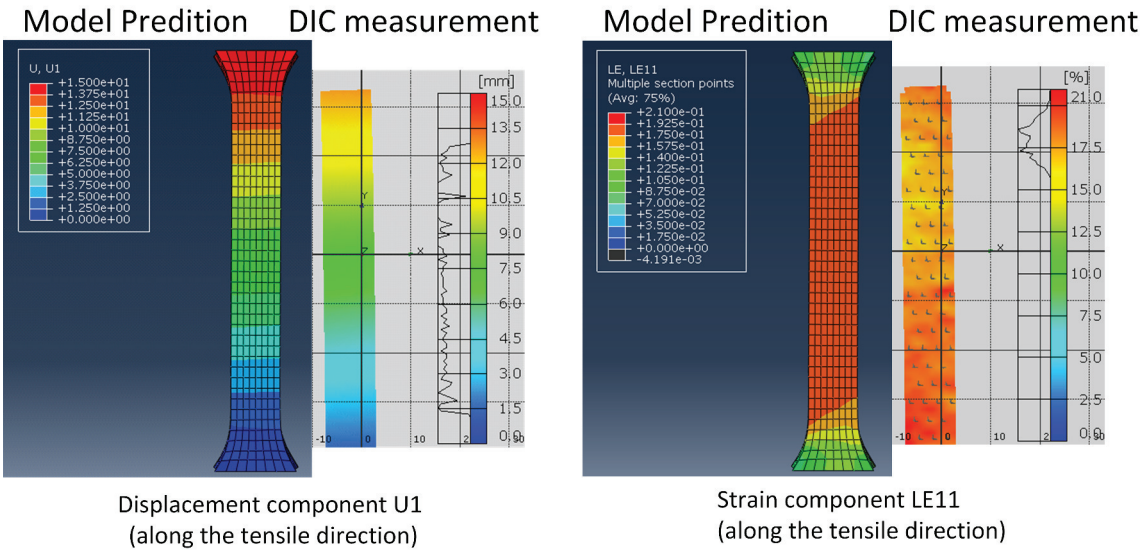

Figure 4.19: Displacement and strain fields comparison between the simulation and DIC measurement for the sample TC90D.

The heterogeneous tread composites gave rise to the complicated deformation modes. A warping around the central axis of the dogbone-shaped specimen of TC0D could be observed so that the surface in the gauge section was no longer in a plane. The sample TC0D has the fiber orientations almost along the tensile direction($\pm 30 deg$ fiber angles), so the stiffness is primarily strengthened in the tensile direction. Whereas the fibers in sample TC90D are more perpendicular to the tensile direction ($\pm 60 deg$ fiber angles), thus the effect of reinforcement fibers in the tensile direction is much weaker than of the sample TC0D. These deformations are all large deformations which can be observed by eye. The full strain field for each deformation case was captured by the Digital Image Correlation (DIC) technology. The displacement and strain fields obtained from the simulation are compared to the measurement of DIC as shown in Fig.4.18 and Fig.4.19.

4.4.3.1 Evaluation of model parameter estimation: Uniaxial tension

The performance of model parameter estimation is evaluated by a two-step process. The first step uses the estimation obtained from TC0D and TC90D to predict the response of TC45D under the uniaxial tension. The sample TC45D showed the most complex deformation mode since two bias plies are not balanced ($+15/+105 deg$ fiber angles) with each other. An "S" shaped deformation field occurred for the gauge section as shown in Fig.4.20 . The simulation captures most of the features of the

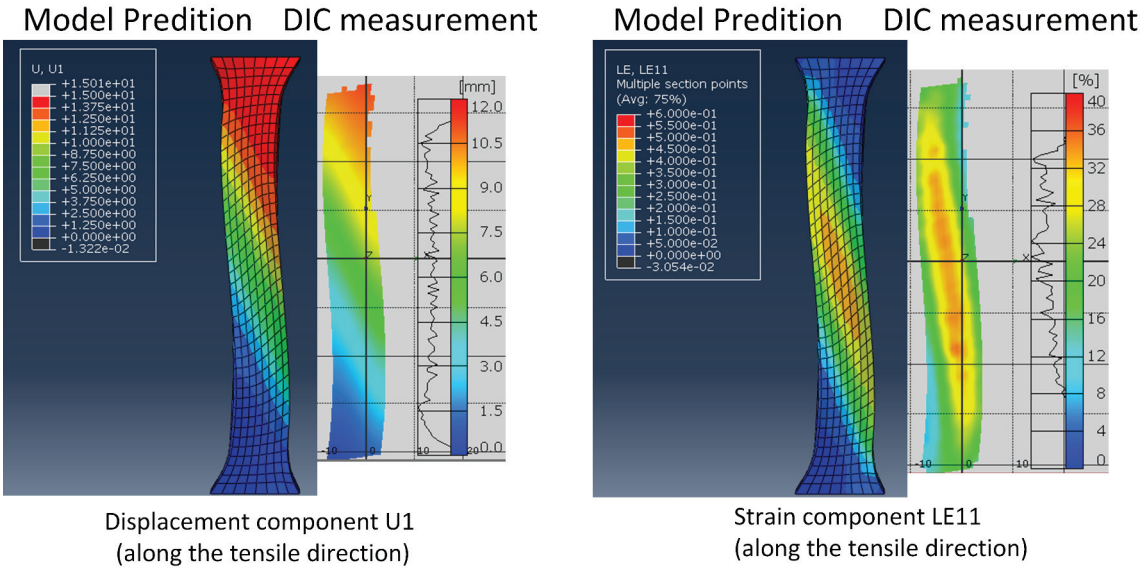

Figure 4.20: Displacement and strain fields comparison between the simulation and DIC measurement for the sample TC45D.

Table 4.3: Quantification of the difference (tensile strain) between the simulation and the measurement for three types of dogbone shaped "sandwich" samples. Note $x = 0$ is the center of gauge section.

	TC0D		TC90D		TC45D	
	simulation	test	simulation	test	simulation	test
$x = -15mm$	18%	13%	19%	20%	30%	22%
$x = 0$	18%	13%	19%	18%	45%	32%
$x = +15mm$	18%	13%	19%	19%	25%	28%

displacement and strain field as the color contours indicated. However, the absolute values are slightly different as in the last two columns of Table. 4.3. To quantify the difference of tensile strain, the values at three "sensor points" along the center axis of the dogbone-shaped specimen are compared for for all three types of samples in Table. 4.3. The main reasons causing the difference are 1) The fibers clasped in the machine grips do extend to the gauge section. The boundary effect of the machine grips do affect the "far field" gauge section through those extended fibers. The simulation cannot fully realize the boundary effect of the machine grips in practice. 2) Helnwein's constitutive relation is not so accurate for the unbalanced plies as for the balanced plies. The deformation of balanced layers is still in-plane response even though anisotropic. In contrast, the unbalanced plies may have out-of-plane deformation under a tensile load, which challenges all kinds of constitutive models of fiber-reinforced rubber. 3) The fiber angles in the real sample are not ideal because the sample was extracted by hand.

4.4.3.2 Evaluation of model parameter estimation: Planar tension

The second step of evaluation is predicting a different deformation mode i.e. planar tension using the same set of estimated parameters from TC0D and TC90D. A rectangular-shaped tread compound sample was extracted from the tire crown region for the planar tension test in the load frame. At the same time, the virtual planar tension test was performed in simulation. The results from the physical and virtual tests are compared.

The rectangular-shaped tread sample has the guage section with dimensions as $168 \times 33 \times 4.7mm$ as shown in Fig. 4.21. The fiber angles of the rectangular-shaped tread sample in the two reinforcement layers are $\pm 60deg$, which are the same as of the dogbone-shaped TC90D sample, relative to the tensile direction. Following the naming convention, the sample used for the planar tension test is named as the rectangular-shaped TC90D sample. The basic experiment settings for the planar tension test are demonstrated in Fig. 4.22 and the image in Fig. 4.22 (a) and (b)

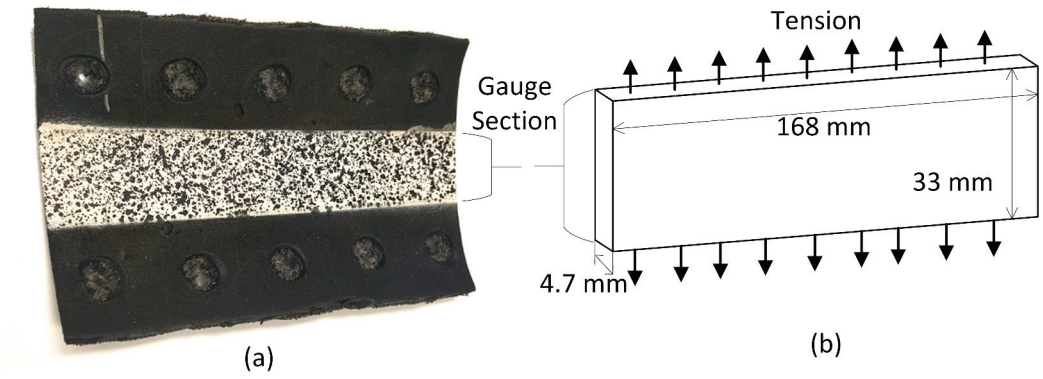

Figure 4.21: Rectangular-shaped TC90D sample for planar tension test. (a) the picture of a real sample. (b) dimensions of the sample and the schematic plot for the planar tension test

are from the left and right camera sensors of the DIC system. At the same time, the measured strain field contour (the strain component along the tensile direction) is imposed on the original images. Notice that the strain fields are the same in both images. The tensile strain ideally should be uniform except the regions near the free edges of the sample. But the irregularity and non-constant thickness of the hand cut sample could not guarantee an uniform response.

In simulation, only the gauge section of the rectangular-shaped TC90D sample is modeled. The measurement shows the tensile strain is around $6\% - 8\%$ and the simulation predicts the strain value $6\% - 9\%$ as in Fig. 4.23(a). The load-extension curve is a direct representation (not normalized) of the compliance of the sample with a physical scale (e.g. the maximum tensile load caused the $2.5mm$ extension of the sample is about $450N$ in this test). The agreement of the load-extension curves in Fig. 4.23(b) demonstrates that the constitutive models and estimated parameters from the small dogbone-shaped samples are still valid to the larger rectangular-shaped sample even under the different deformation mode for the Hoosier LC0 tire tread section.

The method of modeling and parameterization was completed for the tread section of Hoosier LC0 racing tire. The parameterization of remaining tire sections are discussed in the following sections.

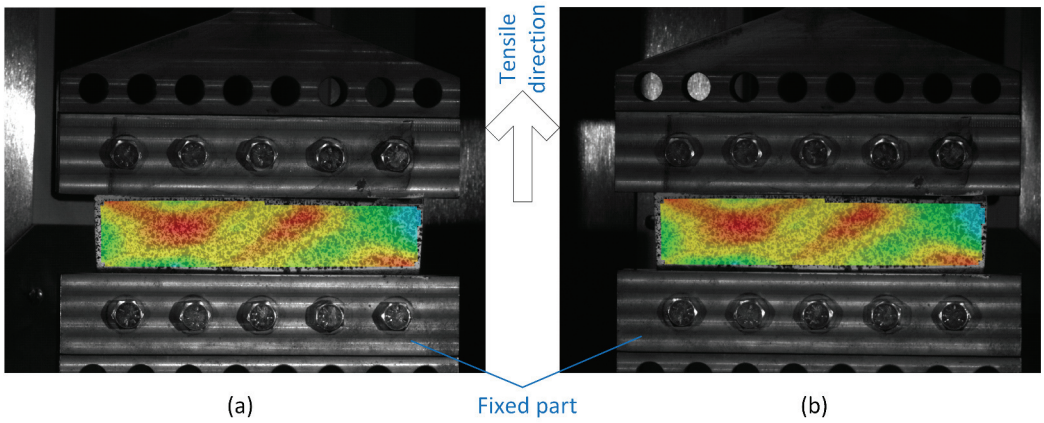

Figure 4.22: Planar tension test configuration illustration by the images from left (a) and right (b) sensors of DIC system. And the strain field of the component in tensile direction is imposed on both images. Keeping in mind that the strain field is repeated in (a) and (b)

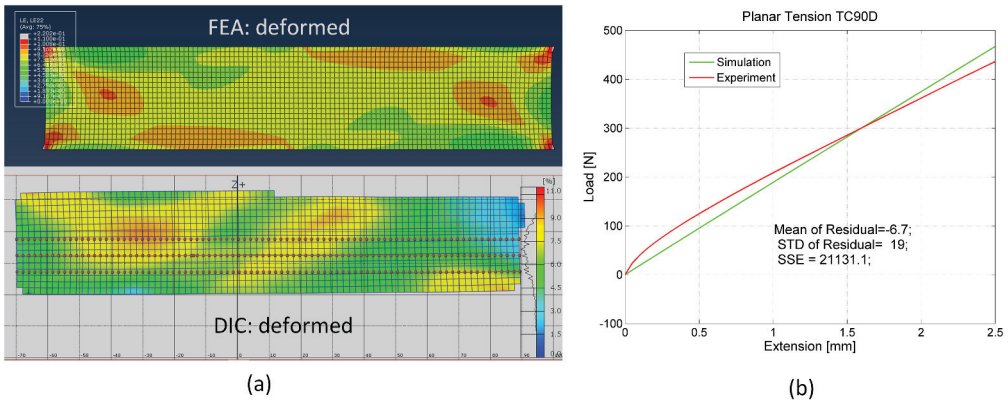

Figure 4.23: Comparison of (a) strain field for the strain component along the tensile direction and (b) the load-extension curve between the simulation and physical measurement. Statistics of comparison between the simulation and test curves are also labeled, where "MR" stands for Mean of Residual and "STD" abbreviates Standard Deviation of residual.

4.4.4 Parameterization of sidewall section

The characterization of the tread section was fully studied. The sidewall section remains to be investigated.

Following the idea of stiffness distribution, the whole sidewall section has to be individually treated up to three sub-sections. The top sub-section has the similar structural form like the tread section. The only difference is a thinner layer of rubber on top of the carcass comparing to the tread section. Thus the constitutive model and material parameters are still applicable to the top sidewall sub-section. The middle sub-section is reinforced by extra turn-up plies which significantly alter the stiffness in that region. Two extra reinforcement layers have to be modeled to account for the added stiffness. For the root sub-section, there is no easy way to know the stiffness there because of the mixed effect of bead filler. An estimation of elastic property in the root region was completed through a particularly designed non-standard mechanical test. Two samples were cut from the tire as shown in Fig. 4.24 and Fig. 4.25.

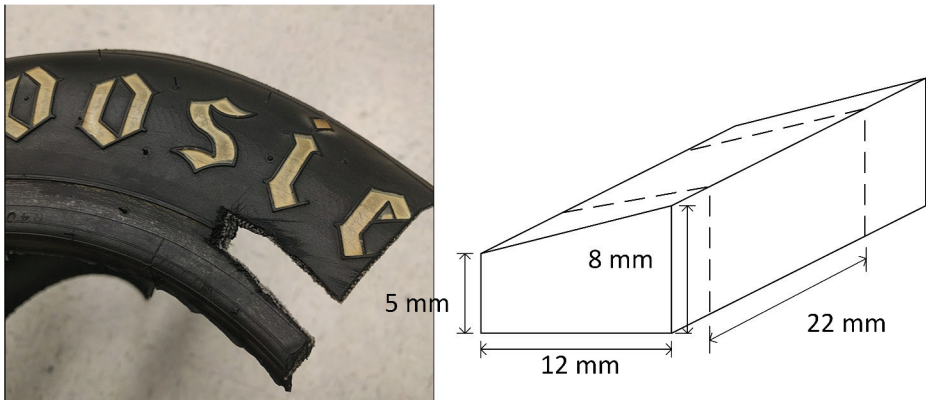

Figure 4.24: The sample cut from the root of sidewall along the circumferential direction. Its ideal shape is illustrated, and the dimension of gauge section is labeled. The two ends beyond the dotted line boundary are regions for gripping in a tensile test.

It is impossible to extract the samples meeting the requirement of ASTM standard on the sample geometry because the limited size of the target region in the tire. One sample is cut along the circumferential direction and the other one is along the meridian direction. The uniaxial tension tests were exercised for both samples. The test data shows the stress-strain behavior of the samples are nearly linear up to 7% of strain as in Fig. 4.26. The root region of sidewall of a rolling tire under a common operational condition does not typically suffer a large strain. Therefore it is sufficient and reasonable using simple linear elasticity to describe the stiffness of this region. The testing results also reveal the anisotropic behavior of the root-sidewall region which states the stiffness along the circumferential direction is almost twice as much

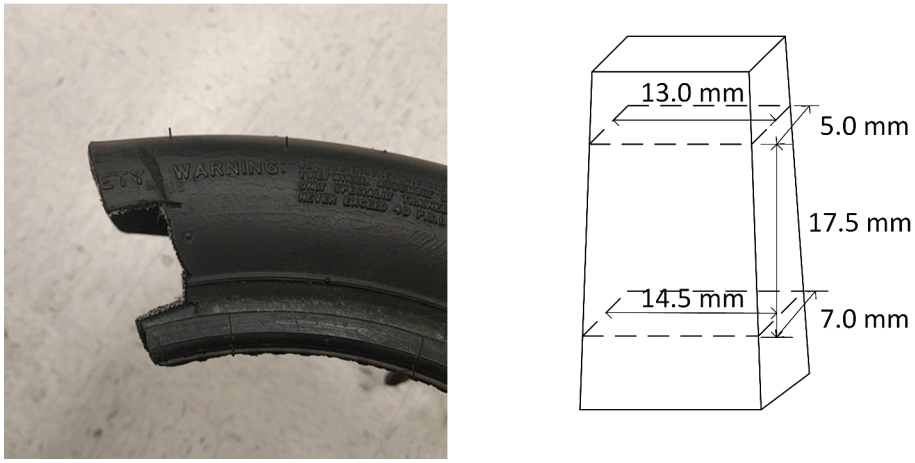

Figure 4.25: The sample cut from the root of sidewall along the meridian direction. Its ideal shape is illustrated, and the dimension of gauge section is labeled. The two ends beyond the dotted line boundary are regions for gripping in a tensile test.

as the meridian direction. However, since the samples are not in any standard size, there is no way to guarantee the accuracy of measurement and the significance of anisotropicity. The test results only provide a rough estimation of the elasticity of the root-sidewall region. In this case, it might make more sense just to treat the stiffness in that region isotropic. The later full tire simulation will shows that this assumption is acceptable in terms of the prediction on global tire response.

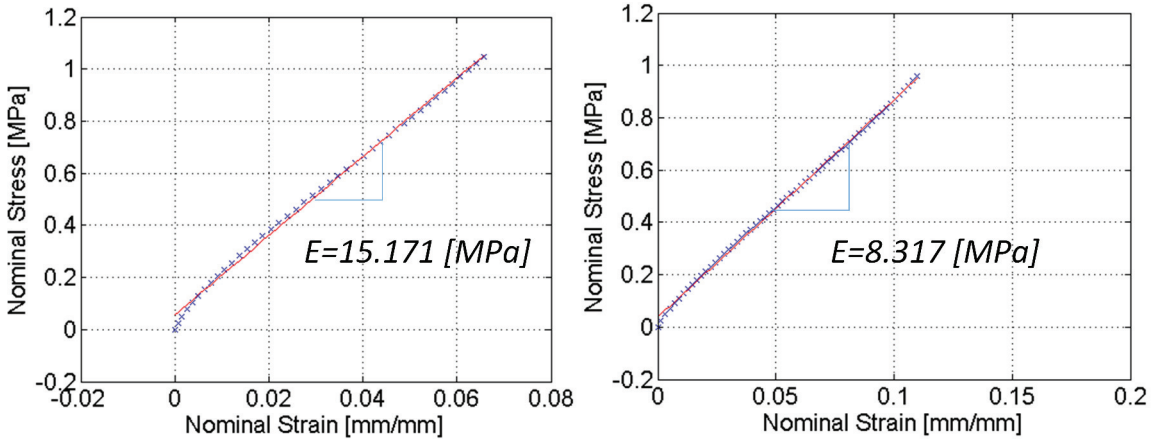

Figure 4.26: The test data shows a linear stress-strain relationship for both samples up to a strain level of 7%.

4.4.5 Parameterization of bead section

The bead section is the region including steel bead cords and bead filler. The stiffness distribution is dominated by the bead cords.

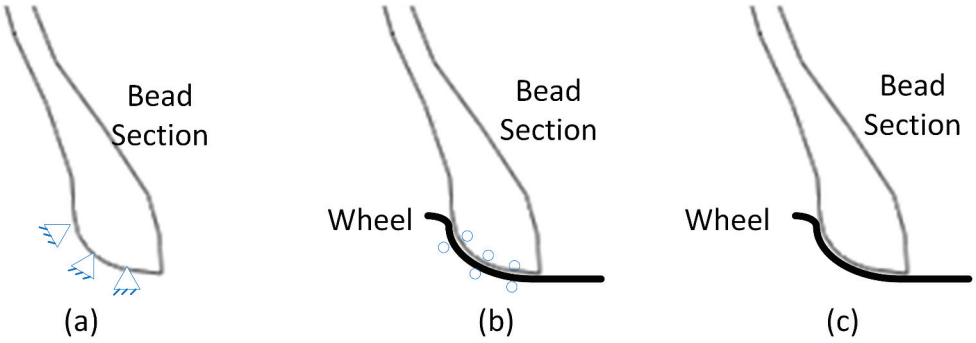

Figure 4.27: Three ways of modeling the tire wheel connection. (a) fixed boundary condition; (b) tie constraint; (c) detailed interaction properties

The ways of modeling the tire-wheel connection affect how to model the bead coil. The simplest way is setting fixed boundary conditions on the bead section as in Fig. (a). In this case, the wheel is not explicitly modeled and the bead coil model is even not required. For the second way as illustrated in Fig. (b), the wheel is explicitly modeled. The bead-rim contact is enforced by the "tie" constraint in Abaqus, which assumes the tire firmly sitting on the wheel all the time. The bead coil can be simplified as one-dimensional curved beam and discretized by beam elements. The third way of modeling the tire-wheel connection allows both contact and separation between the bead and wheel-rim as shown in Fig. (c), which requires detailed description of the bead structure and the bead-rim interaction. Thus, the bead coil needs to be modeled using 3D elements.

This study adopts the second way of modeling tire-wheel connection and saves computing resource for making judgments on the contact conditions between the tire bead and wheel-rim. At the same time, setting "tie" constraint makes little requirement to accurately know the elasticity of bead filler. The estimated elasticity of the root-sidewall region which contains the effect of bead filler rubber compounds is used to approximate the stiffness of bead filler, which is $15MPa$. The stiffness of bead coil is approximated by the elastic modulus of hard drawn - ASTM A 227 steel wire, which is $2 \times 10^5 MPa$.

The stiffness distribution of the whole structure was analyzed and parameterized for the Hoosier LC0 racing tire.

4.5 Hoosier LC0 Racing Tire Structure Model

Based on the parameterization of the Hoosier tire sections according to the stiffness distribution, the 3D structure model of the full tire is constructed as in Fig. 4.28. The FE model is composed of pure rubber parts, the reinforcement layers, and bead coils. The rubber parts are modeled using 3D solid elements with the hybrid formulation to account for the nearly incompressibility. The reinforcement layers are modeled using membrane elements with the "rebar layer" technique. The pair of bead coils are modeled using beam elements to save the degrees of freedoms. The reinforcement layers model is integrated to the 3D solid model by "embedded element" techniques, which is used to specify a group of elements that lie embedded in a group of host elements whose response will be used to constrain the translational degrees-of-freedom of the embedded nodes. However, the rotational degrees-of-freedom of the embedded element nodes are not constrained by the host elements. The bead coil model is also combined in the bead section through the beam-in-solid "embedded elements" techniques.

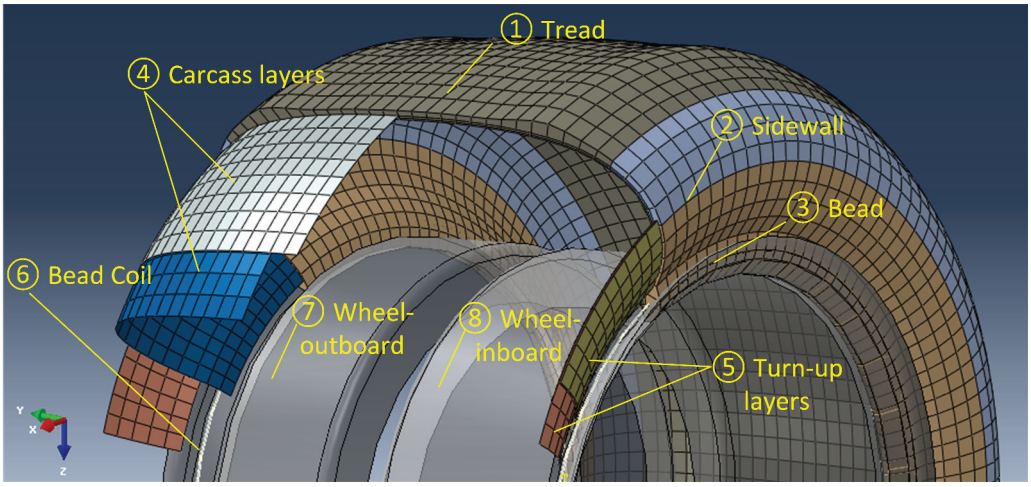

Figure 4.28: The arrangement of reinforcement plies in the developed FE model of Hoosier LC0 tire

The wheel is explicitly modeled as rigid part. The wheel inboard part and outboard part together form the whole wheel. the tire-wheel connection is fulfilled by setting "tie" constraint between the interface of the tire bead and wheel rim. The material properties required for each component have been identified in Section 4.4.

Table 4.4: The element type and integration scheme used in the FE tire model (refer to Fig. 4.28).

ID	Name	Element type	Integration scheme
①	Tread section	8-node brick	Reduced integration
②	Sidewall section	8-node brick	Reduced integration
③	Bead section	8-node brick	Reduced integration
④	Carcass layers	4-node membrane	Reduced integration
⑤	Turn-up layers	4-node membrane	Reduced integration
⑥	Bead coils	2-node element	Full integration
⑦	Wheel-inboard	analytical rigid	N/A
⑧	Wheel-outboard	analytical rigid	N/A

4.5.1 Mass Distribution

The mass distribution of tire structure only affects the dynamic response of a tire. The mass matrix in the equation of motion reflects the mass distribution. The reinforce cord of Hoosier LC0 tire is made of natural fiber and light in weight. Its mass can be neglected comparing to the tread and sidewall rubber. Also, because of the absence of steel belts, the mass density is pretty uniform for the tread and sidewall section for the Hoosier LC0 tire. A pair of steel bead coils primarily contribute the weight in the bead section. The total weight comes mainly from the body rubber and bead coils. This assumption results in less than 5% error between the weight evaluation by the FE model and real measurement by the scale as shown in Table. 4.5.

Table 4.5: Mass distribution and weight evaluated by FE model of Hoosier LC0.

Component	Material	Density $[lbf \cdot s^2/in^4]$	Mass $[lbf \cdot s^2/in]$	Weight $[lbf]$
Body(except beads)	Rubber	0.000105	0.0158	6.10
Bead coils	Steel	0.000739	0.0015	0.58
Total Weight evaluated by the FE model				**6.68**
Total Weight by physical test				**7.03**

One source of the weight/mass difference between the model and test is from the bead coil. But the mass in bead coil is highly constrained by the wheel rim (assuming no debead phenomenon happens), the inaccurate estimation of mass density in the bead region does not have a large impact on the tire response. Another source of the weight/mass difference comes from the neglecting the weight of reinforcement-fibers.

4.6 Hoosier LC0 Racing Tire-Road Contact Model Parameterization

The characterization of tire-road contact property plays the key role for a full tire performance simulation. Since the rolling response predictions are going to evaluated against the test data obtained in Calspan, the contact property technically needs to be characterized between the Hoosier tread surface and the surface of the flat track of the Calspan test machine.

The contact property generally includes mechanical contact properties and thermal contact properties. The tire-road contact modeling has been discussed in Section 3.3. This research only considers the modeling and parameterization of mechanical contact properties. The "hard" contact is adopted for representing the normal contact behavior. The most basic form of classical isotropic Coulomb friction model is used for describing the frictional behavior in this research and has the form,

$$\tau_{cr} = \mu\sigma_n \tag{4.32}$$

where μ is a constant friction coefficient and σ_n is normal contact pressure. Equation. 4.32 is the simplest version of Eq. 3.2. The no-slip condition is still as Eq. 3.1. In sticking state, the frictional shear stress is determined by Eq. 3.3. And in slipping state, the frictional shear stress is τ_{cr}. The relation between the frictional shear stress and total slip is visualized in Fig. 3.4.

The next step is to identify the constant μ for the contact pair of the Hoosier LC0 tire tread and Calspan platform road surfaces. In general, a series of sophisticated experiments have been reported to identify parameters associated with a complex friction model like Eq. 3.2 which may include both mechanical and thermal effects. It should be noticed that the interaction between rubber and road opens a wide research topic which can be traced back to the fundamental study of friction in physics. It is beyond the scope of this research. In addition, the detailed surface property of Calspan platform road surfaces is unknown. The parameter estimation has to rely on the normalized lateral and longitudinal force data in Fig. 4.29(a) and (b) recorded through individual signal channels of the Calspan test platform for the Hoosier LC0 tire. It is noted that the normalized lateral force F_Y/F_Z and longitudinal force F_X/F_Z have the similar physical meaning as μ and are lumped parameters to describe the global behavior but rather the local behavior. It is decided to use F_Y/F_Z and F_X/F_Z to estimate μ.

The interpretation of test data in Fig. 4.29 is developed as below. When a steady state rolling tire subjected to cornering or drive&brake event, if the slip angle(for cornerning) or longitudinal slip ratio (for drive&brake) are beyond a certain limit the whole contact patch becomes a slipping region as illustrated in Fig. 3.3. That means the magnitude of tire lateral force (for cornerning) or longitudinal force (for

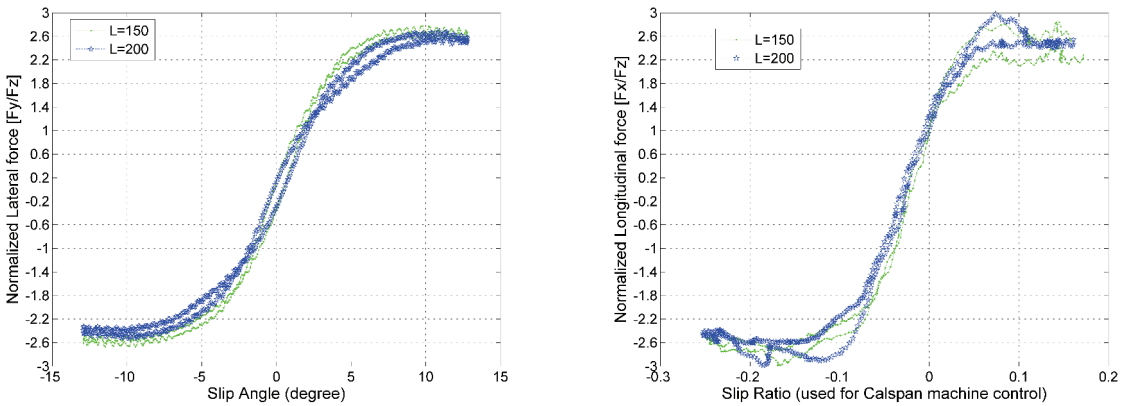

(a) (b)

Figure 4.29: Tire-road interaction model parameterization based on (a) Normalized lateral force vs. slip angle (b) Normalized longitudinal force vs. slip ratio. Their peak values are an indication of "apparent" coefficient of friction when the whole contact patch is in slipping

drive&brake) achieves extreme values because the sliding frictional force cannot exceed a certain limit under a given tire normal load. If we examine the normalized lateral force F_Y/F_Z and longitudinal force F_X/F_Z which share the similar meaning of friction coefficient, the peak values of F_Y/F_Z and F_X/F_Z reflect the "apparent" coefficient of friction under a given tire normal load.

Two normal loads $L = 150lbf$ and $L = 200lbf$ were applied to the tire for both cornering and drive&brake tests. The "apparent" coefficient of friction extracted from Fig. 4.29(a) and (b) is about 2.4 to 2.6 for both out-of-plane and in-plane response, which is a good indication of consistency across different testing modes. The normal load does have an effect on the "apparent" coefficient of friction but not so significant. Finally, it should be noted that the estimated $\mu \in (2.4, 2.6)$ is far larger than a typical value which usually ranges from 1.0 to 1.4 for a tire rolling on a common asphalt track.

Chapter 5

Validation for Static Response

5.1 Axisymmetric Model for Inflation Response

The simplest response of a tire is its equilibrium shape under inflation air pressure without any other external load. The first rigorous analytical solution to calculate the equilibrium shape was obtained by Purdy [37] in the United States. The analytical solution is also believed to be obtained independently by investigators Hofferberth in the Germany, and Biderman in the Soviet Union. Their work is referred to as the PHB solution and summarized and re-expressed by Walter [38]. The usage of the PHB solution previously was to calculate the stresses developed in the inflated tire once its equilibrium shape is accurately known. The importance of the analytical solution for the current study is to provide a verification of the FE tire model in the early stage of model developing.

The PHB theory says most pneumatic tires can be simplified as a thin-walled composite toroidal shell (see Fig. 5.1) which is highly flexible and relatively inextensible when the tire is inflated. The carcass determines the equilibrium shape. The reinforcement fibers embedded in the carcass are in tension mode and form a network to carry the most load caused by the inflation pressure. In other words, the pressure acting on the inside surface of the tire is balanced by the force generated in the fiber network. Furthermore, the fiber is assumed to be inextensible. The rubber matrix plays the role of a membrane to hold a certain volume of air, but does not bear any load. These assumptions are highly idealized, but good enough to predict the inflation response in an analytical way. The geometric parameters used to describe

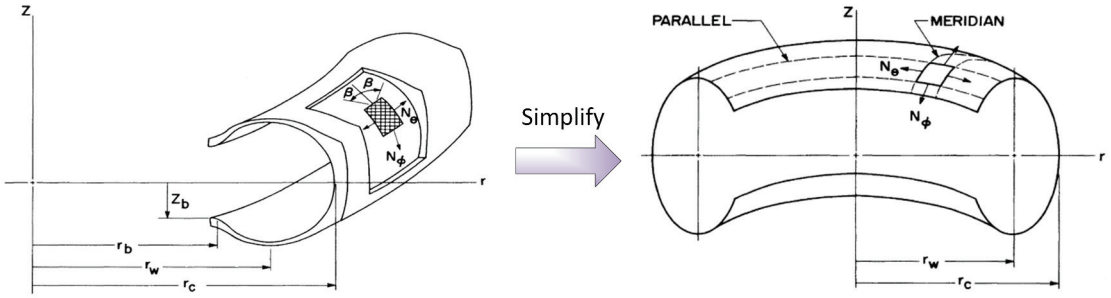

Figure 5.1: Idealized simplification of a pressurized bias tire into a pressured toroidal composite shell. Reprinted from [38]. Reprinted courtesy of the National Institute of Standards and Technology, U.S. Department of Commerce. Not copyrightable in the United States

the equilibrium shape in a cylindrical coordinate system include r_c and r_w which are the radial distance evaluated at the crown and the location of maximum tire section width. The cord angle β is the angle between a meridian and a cord. It should be noted a more common description of a cord angle is so-called the crown angle which relates the cord angle as $\alpha = \pi/2 - \beta$.

The equilibrium shape is in the form of $z = z(r)$ which satisfies a second order nonlinear differential equation involving z' and z''

$$z'' + z'\left[1 + (z')^2\right]\left[\frac{rsin^2(\beta_c)}{r_c^2 - r^2sin^2(\beta_c)} - \frac{2r}{r^2 - r_w^2}\right] = 0 \tag{5.1}$$

where z' and z'' denote the first and second derivative of z with respect to r; and β_c is the cord angle evaluated at the crown. The appearance of the second derivative comes from the mathematical expression of curvature. By the method of solving ordinary differential equations [37], Equation (5.1) can be reduced to a first order equation which further degrades to the indefinite hyper-elliptic integral as

$$z = \mp \int_r^{r_c} \frac{(r^2 - r_w^2)(r_c^2 - r^2sin^2(\beta_c))^{1/2}}{[(r_c^2 - r_w^2)^2 r_c^2 cos^2(\beta_c) - (r^2 - r_w^2)^2(r_c^2 - r^2sin^2(\beta_c))]^{1/2}} dr \tag{5.2}$$

Equation (5.2) is the PHB solution representing the equilibrium contour of a bias tire.

When a tire is only subjected to inflation pressure, its geometry, material behavior, boundary conditions, and loading condition are all axisymmetric with respect to the revolving axle. Therefore, an axisymmetric FE model is sufficient to represent the inflation response which is also axisymmetric. The runtime of an axisymmetric model is much less than an equivalent full 3D model, which speeds the model development. Figure 5.2(a) shows the simulated equilibrium shape of the Hoosier LC0 tire under inflation pressure of 10 *psi*. The response obtained from the FE tire model can be

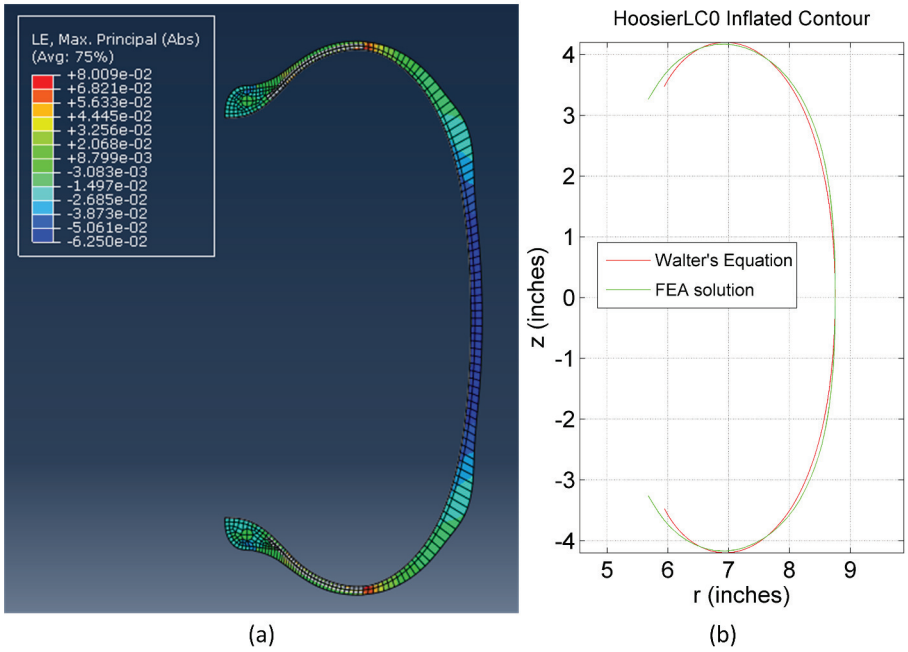

Figure 5.2: The simulation result of the equilibrium shape of the inflated Hoosier racing tire. (a) The simulation with a pressure load 10psi. (b) A comparison between the simulation and the PHB(re-expressed by Walter) solution

verified by comparing with the PHB solution. The deformed (after the tire being inflated) coordinates of element nodes in the mid-surface were extracted from the model. The simulated equilibrium shape was rendered in MATLAB. The analytical solution Eq. (5.2) could be numerically integrated using MATLAB routines. The comparison between the FE simulation and the analytical solution was presented in Fig. 5.2(b). The curves matched each other well on the tread and sidewall sections with a relative difference 1.4%. Equation (5.2) relies on the force balance of a fiber network of the carcass along the circumferential and meridian direction against the effect of inflation pressure, and it works well for the crown and most of the sidewall regions of a tire. While the force balance around the bead region not only matters with the fiber network but also the force transmitted to the wheel rim through the tire bead. The PHB theory does not account for these factors. Therefore, a noticeable deviation occurred on the bead region.

Several successive simulations also justify the assumptions of the PHB theory. Varying the inflation pressure in a range, e.g. from 8 to 12 *psi*, does not change the equilibrium shape of the Hoosier LC0 tire much. This justifies the inextensible assumption of the reinforcement fibers. If the material property of rubber matrix varies, as long as its elastic modulus is far less than the reinforcement fiber, the equilibrium shape does not change significantly either. This supports the second

assumption made regarding the rubber matrix. These assumptions are the basis of formulating the problem of bias-ply tires' static inflation response. At the meanwhile, these assumptions point out the dominant mechanics existing in the inflation response.

5.2 Validation for Static Load-Deflection Response

The typical quasi-static response of a tire is the load-deflection response. The tire behaves like a linear spring subjected to a vertical dead load. The tire spring rate directly relates to the ride performance of a vehicle. Therefore, it is necessary to examine the load-deflection response of the full-3D Hoosier tire model.

5.2.1 Physical test of static load vs. deflection

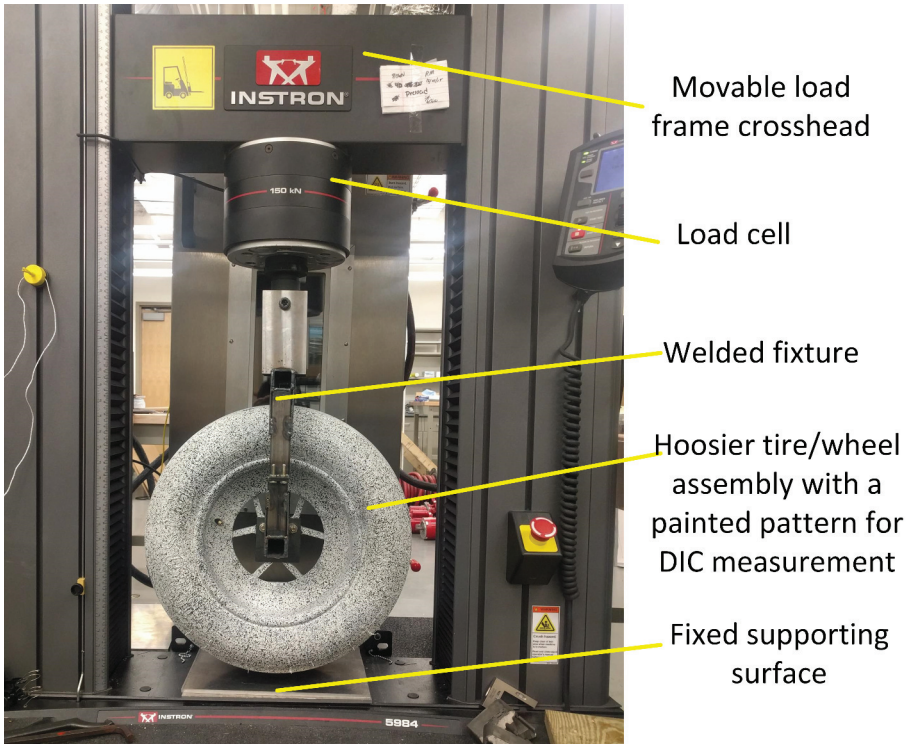

Figure 5.3: The hardware configuration for the quasi-static load-deflection test of the Hoosier tire.

A standard load-deflection test exerts a vertical load on the wheel hub when the tire is supported by a nearly rigid surface. The relationship between a given load and

Table 5.1: The test matrix for quasi-static/static load-deflection tests of the Hoosier tire

		Test Matrix for Session 1 and 2		
Test Sessions	Test Conditions			
Session 1	14psi, DC, Speed_a	12psi, DC, Speed_a	10psi, DC, Speed_a	8psi, DC, Speed_a
Session 1_manual	14psi, LC, Static	12psi, LC, Static	10psi, LC, Static	8psi, LC, Static
Session 2	14psi, DC, Speed_a	12psi, DC, Speed_a	10psi, DC, Speed_a	8psi, DC, Speed_a
Session 2_manual	14psi, LC, Static	12psi, LC, Static	10psi, LC, Static	8psi, LC, Static
		Test Matrix for Session 3,4,5, and 6		
Test Sessions	Test Conditions			
Session 3	14psi, DC, Speed_a	12psi, DC, Speed_a	10psi, DC, Speed_a	8psi, DC, Speed_a
Session 3_manual	14psi, DC, Static	12psi, DC, Static	10psi, DC, Static	8psi, DC, Static
Session 4	14psi, DC, Speed_a	12psi, DC, Speed_a	10psi, DC, Speed_a	8psi, DC, Speed_a
Session 5	14psi, DC, Speed_a	12psi, DC, Speed_a	10psi, DC, Speed_a	8psi, DC, Speed_a
Session 6	14psi, DC, Speed_b	12psi, DC, Speed_b	10psi, DC, Speed_b	8psi, DC, Speed_b
Inflation Pressure :	14, 12, 10, and 8 [psi]			
DC:	Displacement control			
LC:	Load control			
Speed_a:	0.2 [in/min] = 0.003 [in/s], the moving speed of the crosshead of INSTRON			
Speed_b:	0.6 [in/min] = 0.01 [in/s], the moving speed of the crosshead of INSTRON			
Static:	1)manually controlled the moving of the crosshead, the speed<<0.001[in/s]			
	2)The time interval between each data recorded manually four minutes.			
*Note:	"Speed_a" and "Speed_b" are regarded as Quasi-Static condition			
	"Static" is regarded as truly Static condition			

tire deflection is investigated for the Hoosier tire. A special fixture was designed and manufactured to connect the load cell and the wheel hub to conduct physical tests utilizing the INSTRON load frame. The fixture is a welded steel frame. The basic experiment configuration is illustrated in Fig. 5.3. The stiffness of the welded steel fixture in the vertical direction has been measured in advance, which is $8150lbf/in$, and ten times more than the vertical stiffness of the Hoosier tire. So the deflection of the fixture can be neglected. When the cross-head of the load frame moves downward to compress the tire, the transducer in a load cell measures the corresponding vertical load. The displacement of the cross-head equals the deflection of the tire and is also recorded at the same time. The load-deflection curve is a visualization of the relationship between these two data sets and used to validate the static deflection response of the FE tire model.

A test matrix of standard load-deflection tests in Table 5.1 was designed to examine the quasi-static responses under various conditions. A dominant factor affecting a tire's spring rate (vertical stiffness) is inflation pressure. Four levels of inflation pressure were tested $P = 8, 10, 12$, and $14psi$. Noting that the recommended tire inflation pressure is $10psi$. In order to justify the reliability of measurements, six sessions were conducted for each pressure condition. It should be noted that the load vs. deflec-

tion measurements for a given pressure condition was not consecutively repeated six times, the tests in that case would no longer be mutually independent. Instead, the pressure condition was adjusted from 14*psi* to 8*psi* in each single test session and the same procedure was repeated through all six test sessions. The quasi-static condition was satisfied by setting the speed of the cross-head below the limit referred to the ASTM standard in the console. Three "manual" test sessions were added in which the cross-head motion was manually controlled to maximumly approach an ideal static condition. For a given load vs. deflection data point the state was held and not recorded until after about four minutes to eliminate any transient effect. The first two manual sessions adopted the load-control mode, while the third one adopted the displacement-control mode.

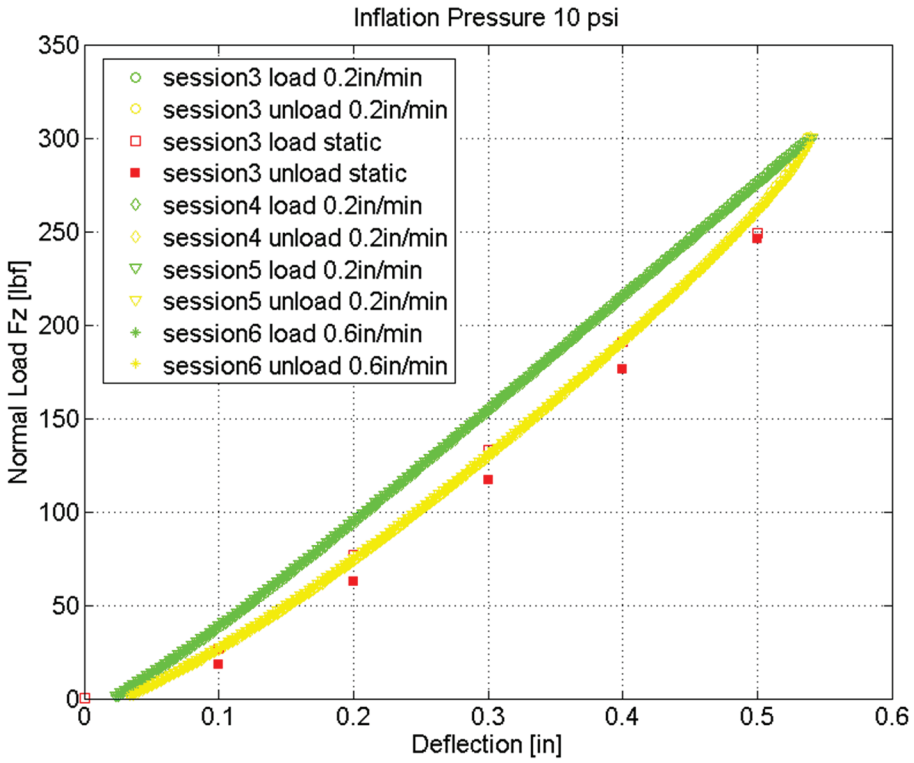

Figure 5.4: The typical raw data of standard load vs. deflection tests when the inflation pressure equals 10psi

The raw data for the 10*psi* inflation pressure is shown in Fig. 5.4. The square marks in red represent data points for the static condition. The unload data does not follow the same path as the load data, which are distinguished by the unfilled and filled square markers respectively. For the quasi-static condition, all types of markers in green represent data points acquired in the different sessions along a load path, and all types of the markers in yellow represent data points along an unload path.

The overlapping of these data points demonstrates good repeatability of the test procedure. The hysteresis in Fig. 5.4 appears in the full tire load vs. deflection plot comes from the hysteresis property of rubber compound addressed in Section 4.4.1. Even for the quasi-static situation, the hysteresis phenomenon can not be completely eliminated but only diminished as the speed of cross-head approaching to zero. The data along a load path is used to evaluate the tire spring rate as a convention.

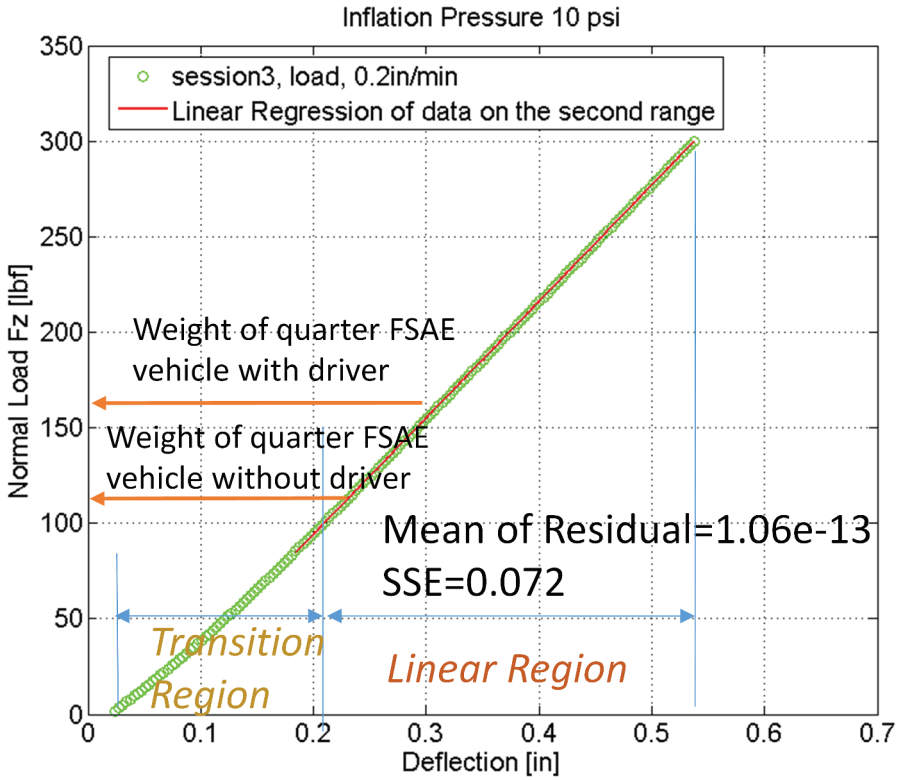

Figure 5.5: Characterization of typical standard load vs. deflection test data of the Hoosier racing tire

A typical load vs. deflection curve is selected from Fig. 5.4 and further analyzed in Fig. 5.5. Beyond the initial transition range, the tire behavior becomes linear as indicated by the statistical results of the applied linear regression as shown in Fig. 5.5. The typical load vs. deflection curve is decomposed into two regions, the "linear region" and the "transition region" which better fits a quadratic relationship. It is hard and unnecessary to define a clear boundary between these two regions. For the current application, the weight of a quarter FSAE vehicle with or without a driver as a vertical load acting on the tire falls in the linear region. Thus the characterization of data in the linear region is our priority. The slope of a regression line is defined as the tire vertical stiffness or tire spring rate which is a key feature of the tire static

behavior. Although the static and quasi-static data on a load path in Fig. 5.4 does not overlap with each other, it should be noted that the loading and unloading data exhibit nearly the same slope. Later validations in utilize the test data collected in the static condition.

5.2.2 Virtual test of static load vs. deflection

The Hoosier LC0 tire structure model developed in Chapter 4 is used to conduct the static load vs. deflection virtual test. The appropriate boundary conditions, loads, and simulation steps need to be prescribed for the virtual test. The Abaqus Static-General solver is used for simulation, so only the stiffness distribution (stiffness matrix) of the model dictates the solution.

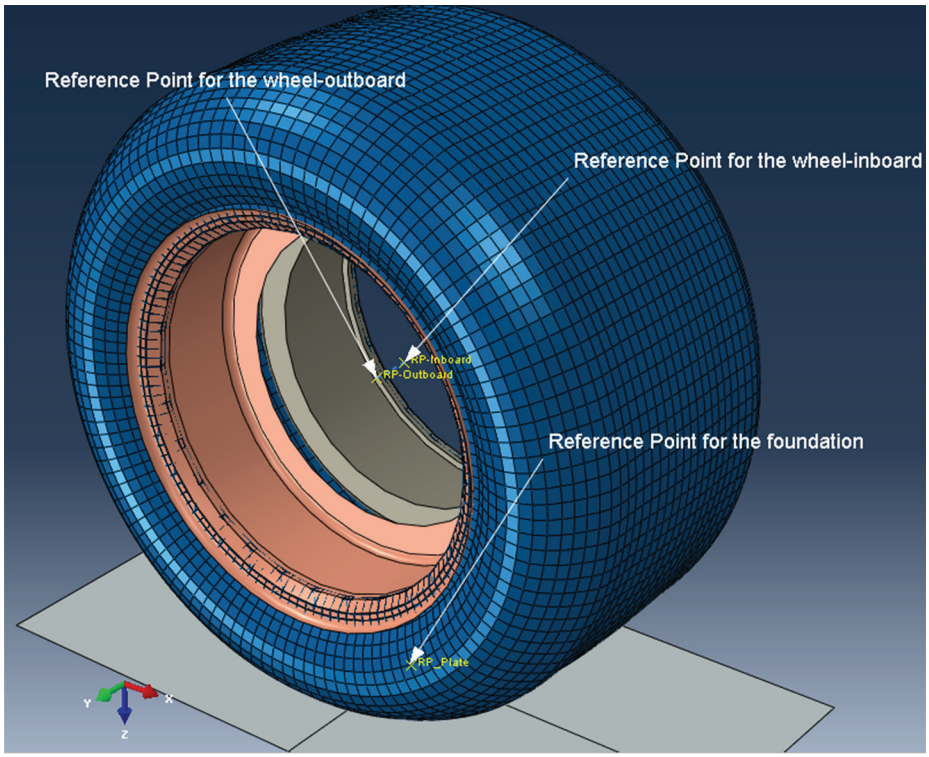

Figure 5.6: The initial tire/wheel assembly and reference points configurations

The wheel is modeled as two separate parts, wheel-inboard and wheel-outboard. These two parts are analytical rigid, and each one is assigned a reference point to represent their rigid body motion in 3D space. The rim of wheel-inboard and wheel-outboard connects to the tire bead section through 'tie' constraints as illustrated in Fig.4.27 (b). The distance between the two bead-contact surfaces of a free/unmounted tire is always larger than its designated wheel rim width. So, in the initial assembly,

the wheel-inboard and wheel-outboard are separated by a distance as shown in Fig. 5.6. To simulate the tire mounting process, a 'translator'-type connector element is used to connect the wheel-inboard and wheel-outboard. The reference points of two wheel parts are set as the end nodes of this connector element. Then the tire mounting process can be realized by shortening the length of the 'translator' to make the wheel-inboard and wheel-outboard attached together. The inflation process is fulfilled by exerting pressure load to the inner surface of the FE model.

The foundation to support the loaded tire is modeled as rigid surface and assigned an individual reference point to represent its motion. A easy way to simulate the load-deflection process is fixing the wheel center (the reference point for the wheel-inboard can be deliberately set on the location of the wheel center) and moving the foundation surface upward against the tire model. The 'displacement-control' mode of the load-deflection process can be realized by prescribing the displacement of the reference point of the foundation relative to the wheel center. The 'load-control' mode of the load-deflection process can be realized by exerting a force on the the reference point of the foundation upwards in the opposite direction of a vertical wheel load. If the 'displacement-control' mode is adopted, the resultant normal force can be extracted from the wheel center. If the 'load-control' mode is adopted, the tire deflection can be calculated from the relative distance between the foundation and the wheel center. The 'hard contact', which is introduced in Section 3.3.1, is used to model the normal contact behavior between the tire tread and foundation. The tangential behavior of the contact is set to 'frictionless'.

The reduced integration is preferred for the the 8-node brick isoparametric 3D elements when they possess nearly incompressible constraints. If these elements suffer bending, the full integration will make the element too stiff to bend and causes undesirable response which is called 'lock-up in constant volume bending'. The reduced-integration applied on the same elements often work well in such cases. In addition, the reduced integration lowers the cost of computing. The pay-off is using the reduced integration may result in the unusable hourglass mode.

The simulation steps are designed as shown in Table. 5.2. Users can set the step intervals for Abaqus outputting the simulation results. For example, this research set four intervals from the step4 to step5 to enable the results outputted at the vertical load $L = 50$, $L = 100$, $L = 150$, $L = 200$, and $L = 250lbf$.

5.2.3 Validation results analysis

The load vs. deflection results comparison is visualized in Fig. 5.7 between the physical and virtual standard load vs. deflection tests of the Hoosier racing tire under four levels of inflation pressure. Notice that the tests in a load-control mode (line in pink) result in a systematic bias of the tire spring rate which is higher than the measurements (lines in cyan and red) in a displacement-control mode. Especially for

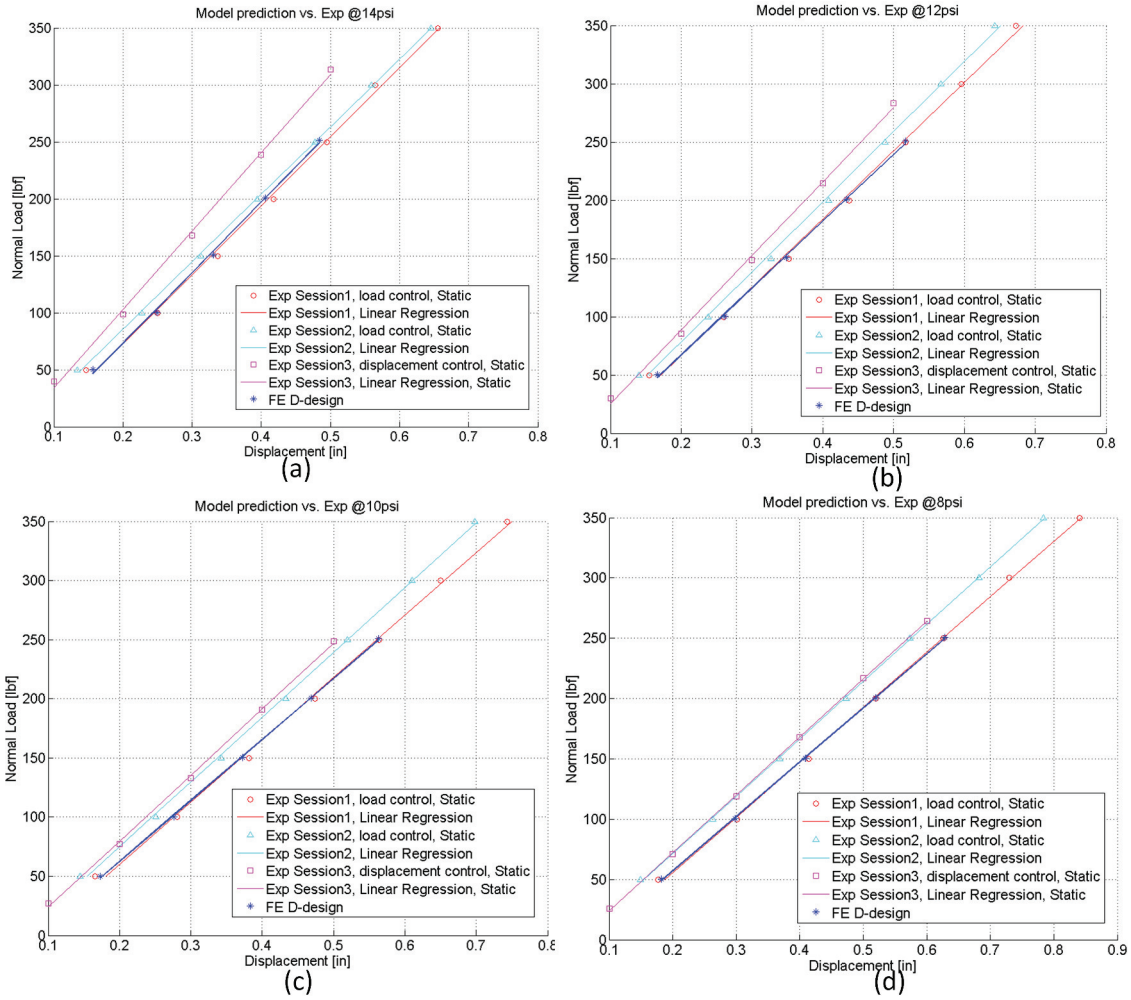

Figure 5.7: Validation of static responses of the LC0 Hoosier tire through standard load vs. deflection tests at four levels of inflation pressure, which is (a) 14psi, (b) 12psi, (c) 10psi, and (d) 8psi

Table 5.2: Simulation steps for the virtual load vs. deflection test

Step Name	Description
Step1-Mount&Inflation	Simulate the tire mounting and inflation process in one step
Step2-DispControl	Create the initial tire-foundation contact by displacement-control mode
Step3-preLoad	Adjust the normal contact load to a small value ($3lbf$) by load-control mode
Step4-Load50	Add wheel load to $50lbf$ via load-control mode
Step5-Load250	Add wheel load to $250lbf$ via load-control mode

the case of $P = 14psi$, the measurement in a load-control mode gives an extraordinary bias. The bias may be introduced by the difference of test procedures. It can be seen that the FE model's prediction (line in blue) for each condition of inflation pressure agrees with the test results. Table. 5.3 numerically summarizes the validation results of the static response to quantify the performance of model predictions. The "true" value of the vertical stiffness is estimated by taking an average of three independent measurements for each case. Notice that the abnormal measurement in a load-control mode at $P = 14psi$ has been excluded. The relative difference is then computed between the simulations and tests, which fall in a $\pm 6\%$ bound for all cases.

Table 5.3: The model predictions vs. physical tests on the static tire spring rate of Hoosier LC0 tire.

Test Sessions	Inflation Pressure			
	14psi	12psi	10psi	8psi
Session 1_manual	604.9	585.6	527.2	457.5
Session 2_manual	592.5	601.5	547.4	475.3
Session 3_manual	687.4	635.4	557.5	480.3
Average	598.7	607.5	544.0	471.0
Model Simulation	618.7	573.6	515.2	449.7
Error%	3.30%	-5.58%	-5.29%	-4.52%

Besides checking the global static load vs. deflection response, it is also good to examine the strain generated on the sidewall of the Hoosier tire with the help of Digital Image Correlation(DIC) although which is not our first priority. The sidewall and the aluminum-alloy wheel were painted with a high contrast random pattern as shown in Fig. 5.3 for measuring the deformation via DIC. The measured max-principal strain on the full 3D sidewall surface is presented in Fig. 5.8(a) for the normal load of

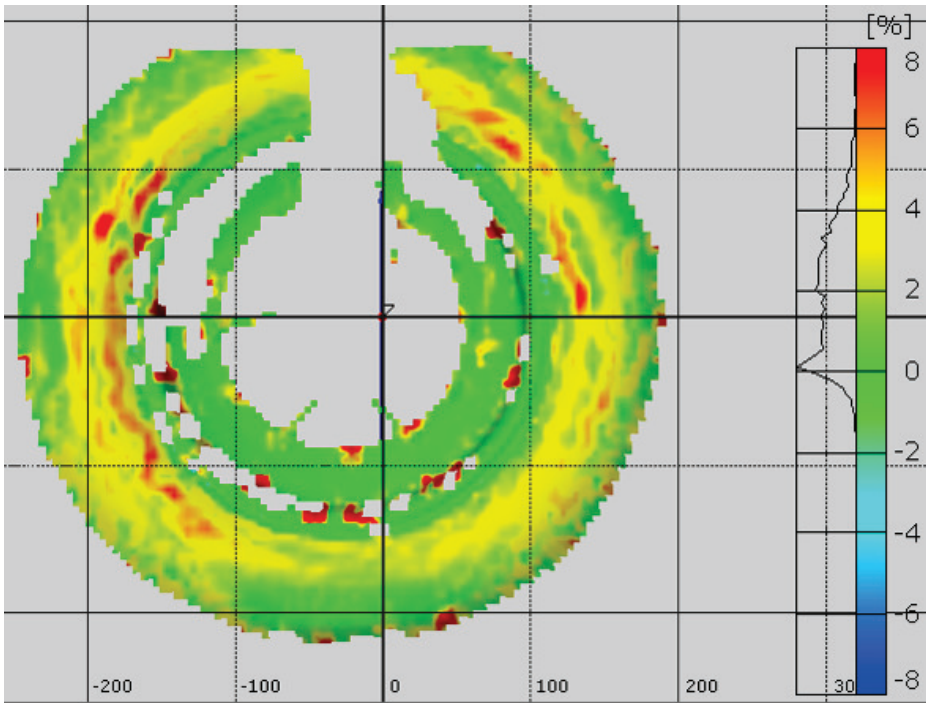

(a)

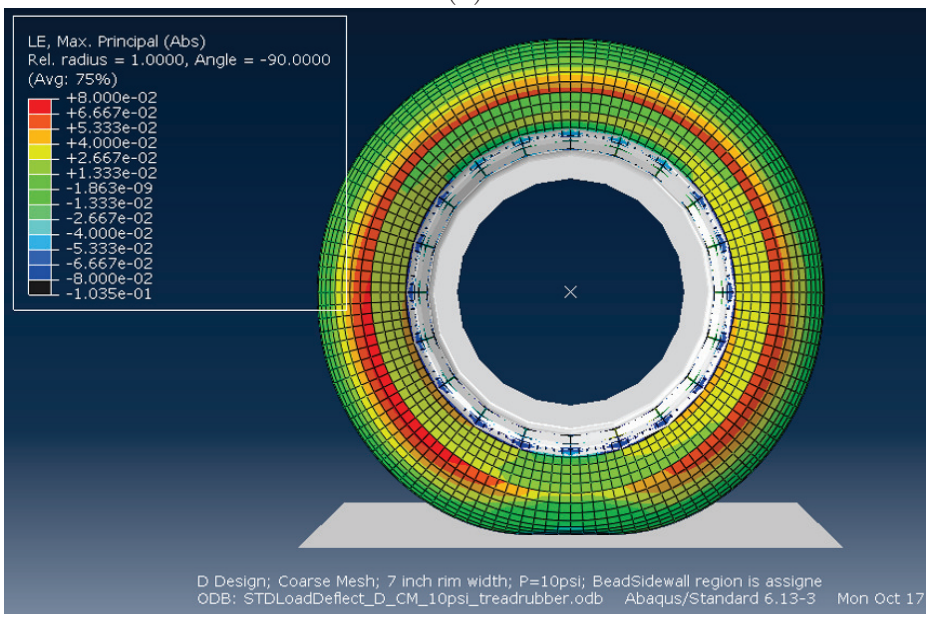

(b)

Figure 5.8: The strain occurred on the sidewall of Hoosier LC0 tire subjected to a vertical load $L = 250lbf$ and inflation pressure $P = 10psi$ (a) DIC measurement (b) FEA simulation

$250lbf$ and the inflation pressure of $10psi$. It is observed that the highest strained region occurred in the middle of the sidewall all the way along a hoop direction then lessened in the sector which connects to the contact patch. The peak max-principal strain value is around $6\% \rightarrow 8\%$ for most of the sidewall and decreases to about 2% in the sector involving the contact patch. Other critical information from the measurement is that the strain in the wheel was so small compared to the strain generated in the flexible sidewall that the wheel can reasonably be assumed as a rigid part in the model. The FE simulation for the Hoosier LC0 tire at $250lbf$ vertical load at $10psi$ inflation pressure gave out a similar strain distribution as shown in Fig. 5.8(b). Although it is not our purpose to match the local strains between the simulation and measurement, the simulation provided additional evidence that the developed model captures the right mechanics of the tire structure in addition to its global load vs. deflection response.

The mechanics of load carrying of the tire structure under static load is further analyzed. The discussion starts from the inflated but undeflected tire whose casing takes up its equilibrium shape. The detailed features of a tire e.g. turn-ups, filler, etc and their effects for ease will be ignored. When the tire is pressed against a flat surface, the tire locally loses its axisymmetry because of the added load and boundary. A contact patch forms to flatten the tread section. The cords of the casing in the tread section in contact with the road will also lie in a flat plane, and hence, the cords in that region become straight and still in tension. The tension is determined primarily by the cord tension transmitted from the adjacent free wall of the tire. In other words, the tension in the cord bears no relation to the inflation pressure in that particular region compared to the purely inflated condition. If the tire contact patch is isolated from the remaining tire body, the force balance in the normal direction requires the contact pressure from the road to tread should be roughly the same as the inflation pressure(strictly speaking, slightly greater than the inflation pressure). In reality, the contact pressure at the peripheral region of the contact path, especially in the region containing the tread shoulder (with thicker tread rubber than tire crown), is higher than the average contact pressure in the middle region of the contact patch. Therefore, most of the vertical load is balanced by the product of the overall contact area and inflation pressure. The remaining portion of the vertical load is carried by the tire structure itself.

The transmission of force from the contact patch to the wheel can be explained through a few steps. Figure. 5.9(a) shows the situation when the tire is statically loaded by inflation and contact pressure. The contact force transmitted from the road is balanced by the effect of inflation pressure acting on the contact region. The inflation pressure acting on the remaining sector of the tire causes a unresisted net force which has the tendency to pull the bead coil upward as illustrated in Fig. 5.9(b). This force tries to pull the bead coil against the rim of wheel above the contact region, thus transmitting the upward force to the wheel as shown in Fig. 5.9(c). Finally, the upward force is balanced by the wheel vertical load downward.

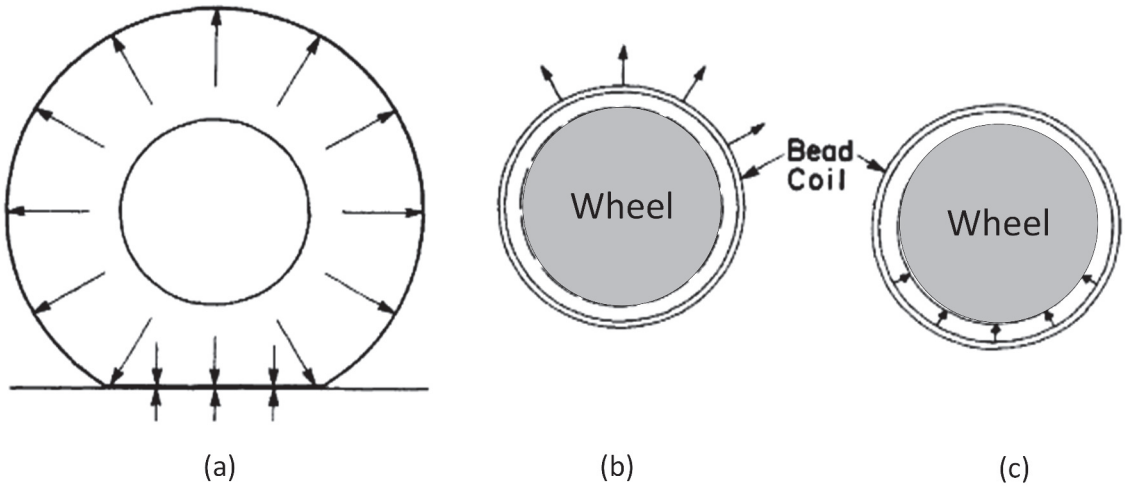

Figure 5.9: Mechanism of load transfer from the road to wheel

Overall, the vertical dead load acting on the wheel causes the tensions of sidewall in the lower half diminished and the upper half increased comparing to the equilibrium state subjected only to inflation pressure. This description directly justified by the DIC measurement result.

As one merit of the FE tire model, the information of contact patch can be retrieved from the simulation results. Figure 5.10(a) shows the normal contact pressure distribution (recall the normal contact algorithm in Section 3.3.1) when the inflation pressure $P = 10psi$ and the wheel load $L = 150lbf$. It is seen that the contact pressure in the center region of the contact patch is about $10psi$, which equals the inflation pressure, and higher contact pressure occurs in tread shoulder regions as expected. Figure 5.10(b) shows the contour of opening distance which measures the distance from a point on a 3D surface to a contact plane. Therefore, the region having zero opening distance delineates the geometry of the footprint. The shape of footprint and contact pressure distribution for the static load case technically can be validated by a experimental process using the pressure indicating film. This research did not carry out the validation of the contact path phenomena.

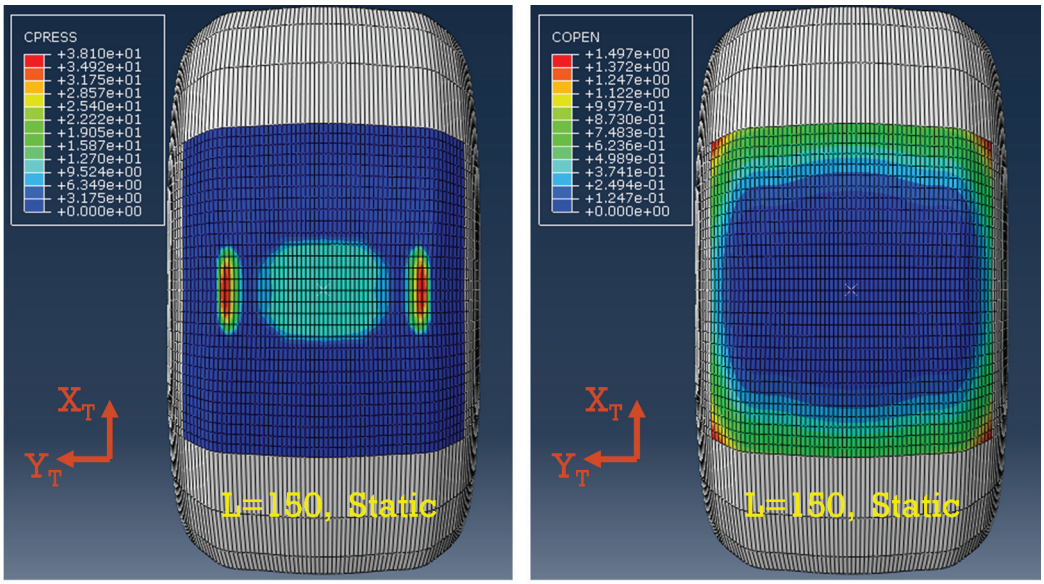

Figure 5.10: The contact pressure in *psi* (a) and contact opening distance in *in* (b) distribution in the contact patch for the static condition when the inflation pressure P= 10 *psi* and the wheel load L= 150 *lbf*

Chapter 6

Validation for Steady-State Response

6.1 Introduction to Steady-State Analysis

6.1.1 Problem formulation of steady-state rolling

Steady-state response is the most fundamental response and a special case of general dynamic response for a rolling tire. The steady-state rolling requires the revolution speed of the wheel is constant and the angular acceleration is zero. If an observer is in an earth-fixed coordinate system, he views the steady-state rolling of a body as a time-dependent process since each material point in the rolling body periodically undergoes a repeated history of deformation. Now introduce a new coordinate system which is attached to the revolution center of the rolling body and translates at the same velocity of the axle, but this coordinate system does not spin with the rolling body. An observer in this coordinate system can describe the motion in the Eulerian manner which features giving attention to what is occurring at a fixed point in space as time progresses. The points which define the boundary of the rolling body are fixed in the new coordinate system, but the material made up of the body is flowing through those locations of points. The explicit time dependence of the velocity $\mathbf{v}$ of a material point described in this coordinate system is then removed, i.e.

$\mathbf{v}$ becomes only function of location $\mathbf{x}$, and $\mathbf{v} = \mathbf{v}(\mathbf{x})$. The observer in the new coordinate system sees fixed spatial points with "material flow" passing through them. In the new coordinate system, the rigid body rotation of the steady-state rolling body is described in a spatial (or Eulerian) manner, while the deformation which now is measured relative to an undeformed body with the same rotational speed is described in a material (or Lagrangian) manner. This new way of describing the steady-state rolling is called the mixed Lagrangian/Eulerian method.

Using a Lagrangian formulation to describe the steady-state rolling of a tire is computationally expensive because a transient analysis can not be avoided in order to get a steady-state solution. In addition, a fine mesh is required along the entire hoop direction of the rolling body since the whole tread surface has a chance to contact the road surface. In contrast, the mixed Lagrangian/Eulerian method converts the steady-state rolling contact problem into a purely spatially dependent problem. The finite element mesh describing the rolling body in the second coordinate system does not undergo the large rigid body spinning motion. Consequently, a fine mesh is only required near the contact zone.

Abaqus provides the steady-state transport solver to deal with the steady-state rolling problem with considerable efficiency because the cost of the analysis is independent of the rolling speed. The theory is described in detail in the Abaqus theory Guide. The steady-state transport solver in Abaqus/Standard uses Newton's method to solve the nonlinear equilibrium equations. The nonlinearities in a steady-state transport analysis arise from large-displacement effects, material nonlinearity, and boundary nonlinearities such as contact and friction.

6.1.2 Free rolling as a special case

The free-rolling condition is a special case of the steady-state rolling. First, the free-rolling tire/wheel must possess a zero inclination angle and slip angle, which implies the tire is rolling along a straight line. Second, the translational speed of the wheel axle, v, and the revolutionary speed of the wheel, ω, in straight line rolling have to make the tire/wheel with zero applied torque around the wheel axle and no slipping between the tire-road interface to achieve the free rolling condition. The translational speed of the wheel axle and revolutionary speed in this special rolling state are denoted as v_0, and ω_0(reference spin velocity) respectively. In general, v and ω are two independent kinematic quantities. There are several other possible in-plane rolling modes characterized by various combinations of v and ω. The free-rolling mode is usually regarded as a reference for other complex rolling modes. The translational speed of the wheel axle, v, is also called ground speed in some literatures because v is a measurement of the relative translational speed between the wheel axle and the road. The dynamics for a free-rolling tire rolling on a fixed road and on a moving flat-track test machine is the same. The term "translational speed of the wheel axle"

is more suitable for the tire rolling on the fixed road, while "ground speed" is more suitable for the tire rolling on the flat-track tire test machine.

A free-body diagram in Fig. 6.1 shows the case of free rolling. F_d is the force to tow the wheel and maintain it moving forward at a constant velocity,v. F_X is the tangential resultant force generated in the contact patch equal and opposite to F_d. The wheel load is F_Z, and its reaction normal force is F_n. The overall resultant force which is the combination of F_X and F_n must pass through the revolution axis otherwise it would produce a nonzero moment which breaks the law of balance of moment since the applied torque T is always zero for a free-rolling wheel. As a result, F_n cannot be collinear with F_Z and shifts with a distance e from the centerline. The important role of the free-rolling condition will be reflected in the following in-plane and out-of-plane response.

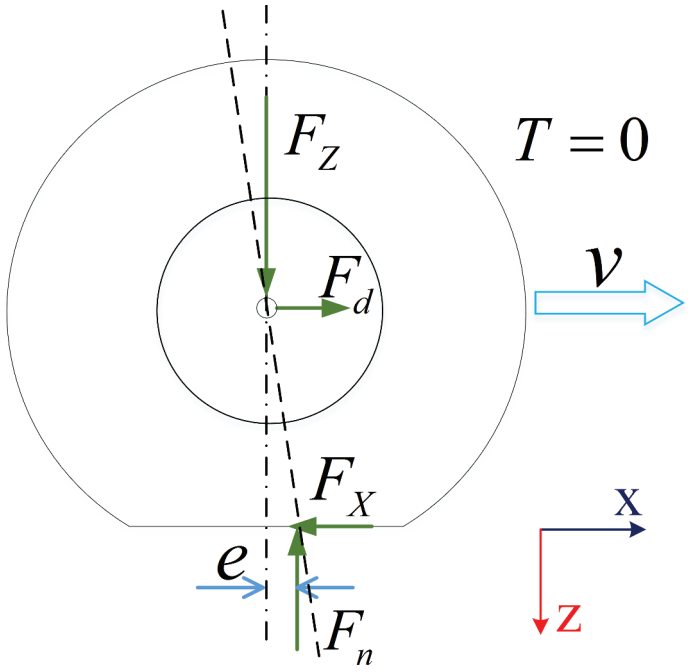

Figure 6.1: Free Body Diagram of a free rolling tire

6.2 Validation Plan Based on Calspan Test Data

The FSAE Tire Test Consortium(TTC) contracted Calspan Tire Research Facility (see Fig. 6.2) for testing a series of racing tires in the laboratory environment to benefit university racing teams in 2012. The Hoosier LC0 6.0/18.0 − 10 racing tire

was chosen as one of the subjects in the test round 5. The complete suite of tire tests was divided into two parts, cornering tests and drive/brake tests. Both were steady-state response tests.The tests plan and test data description can be found in the unpublished document named "FSAE TTC- ROUND 5 RUN GUIDE" and "FSAE TIRE TEST CONSORTIUM-ROUND 5". The cornering test data is going to be used to validate the out-of-plane response of the developed FE tire model. The in-plane response of the developed tire model will be compared against the drive/brake test data.

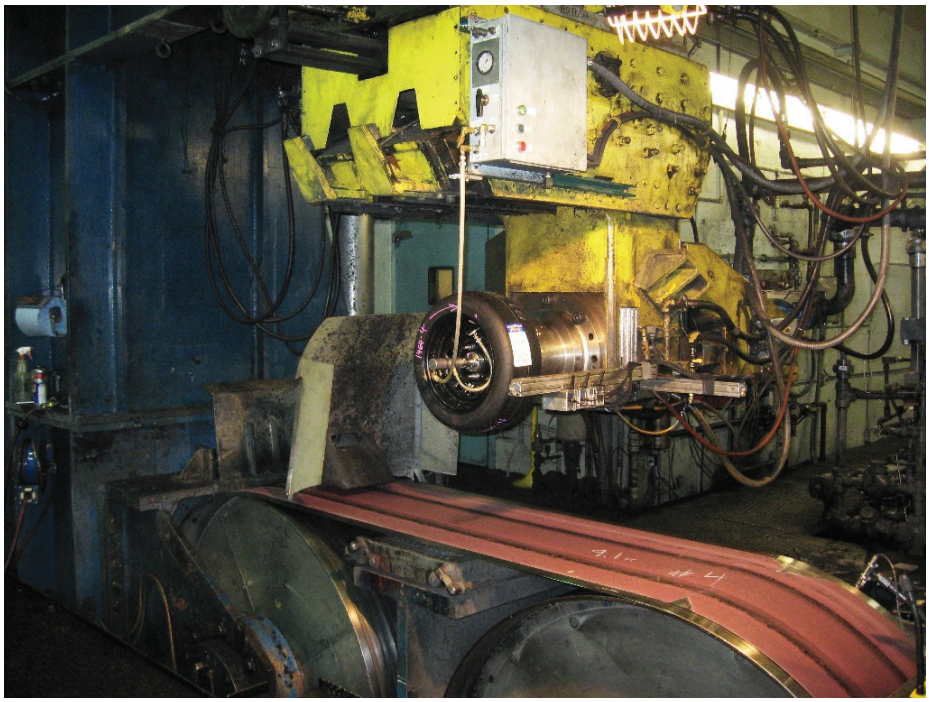

Figure 6.2: Calspan Tire Research Facility for FSAE tire testing

Table 6.1: Two factors design for visualizing the cornering test

FACTORS		
Pressure (P) [psi]	Normal Load (L) [lbf]	Response (FY)
10	150	Fig.(a)
10	200	Fig.(b)
12	150	Fig.(c)
12	200	Fig.(d)

6.2.1 Cornering test

The cornering test was started with a free-rolling (no slip angle, no longitudinal slip ratio) condition. The road speed was maintained at $25mph$. The slip angle(SA or α in degrees) of the rolling tire was set to sweep between -12 and +12 degrees. Various combinations of the inflation pressure, normal wheel load, and inclination angle conditions were exercised during the test. The tire lateral force F_Y induced by the slip angle is regarded as the output/response. A way of visualizing the data under various conditions is proposed as in Fig. 6.3.

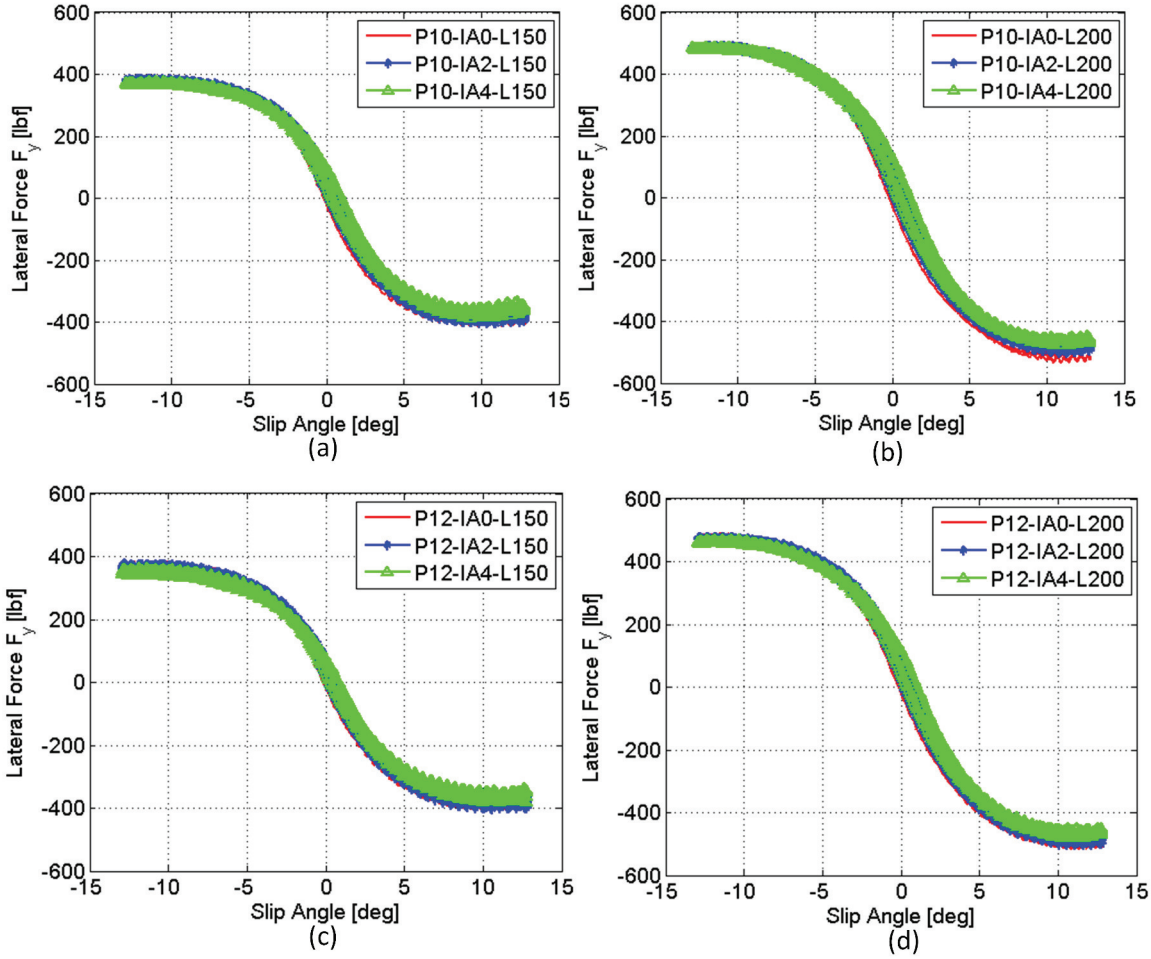

Figure 6.3: Cornering response test data of the Hoosier LC0 tire

A matrix for displaying the test data in the way of Fig. 6.3 is explained in Table. 6.1. The symbol L, P, IA represents the vertical wheel load in lbf, inflation pressure in psi, and inclination angle in $degree$ respectively. Each subplot in Fig. 6.3 corresponds to one case of the combination of normal load and inflation pressure. Three curves

in each subplot are measurements under three inclination angle conditions (IA=0, 2, 4 in degree). The influence of inclination angle to the lateral force is within 5%. Consequently, inclination angle does not appear in Table 6.1 since it does not account for a major influence factor. Furthermore, if Fig. 6.3(a) is compared with Fig. 6.3(c) or Fig. 6.3(b) is compared with Fig. 6.3(d), it is observed that the influence of inflation pressure on the output is less significant than the influence of normal wheel load. The most significant factor is the normal wheel load.

6.2.2 Drive/Brake test

The drive/brake test was implemented by fixing the road speed at $v = 25mph$ and varying the spinning speed ω of the wheel. The longitudinal slip ratio whose accurate definition will be expanded in Section 6.5 is used to describe the possible combined states of rotation and translation of a tire. The longitudinal slip ratio is regarded as an independent variable of any drive/brake test as a convention. The slip ratio used here was designed according to the Calspan test protocol and controlled to sweep from -15% to +15%. The longitudinal tire force F_X was examined as the output/response. It should be noted that the electro-mechanical control of the test platform required for the drive/brake test is much harder than the cornering test. That is why the drive/brake data looks more noisy than the previous cornering data. For this reason, a portion of data beyond the designed data acquisition range is also in record.

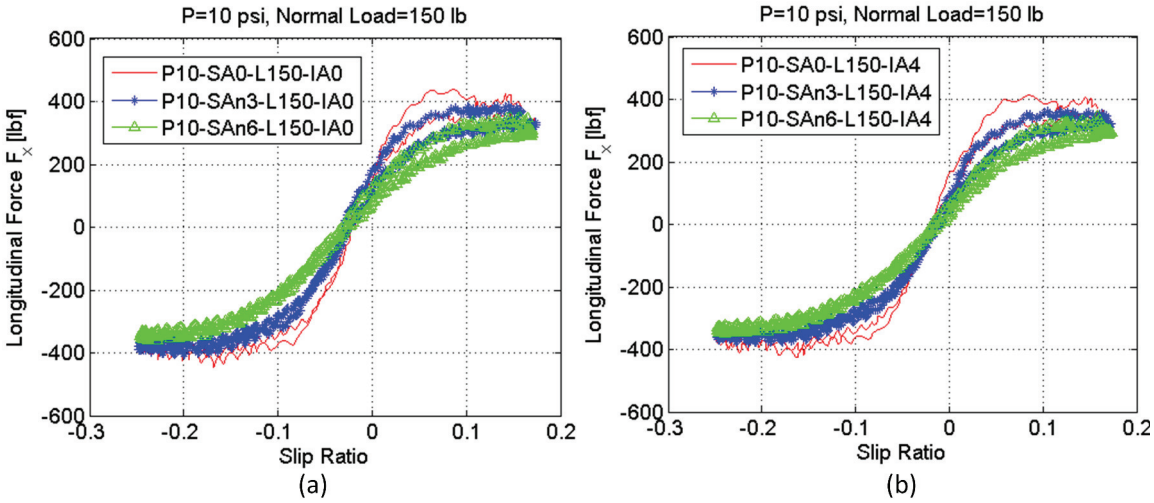

Figure 6.4: Longitudinal force vs. slip ratio curves do not change much when the inclination angle(IA) changes from 0 degree in (a) to 4 degrees in (b). The slip angle(SA), inflation pressure(P), and normal wheel load(L) are kept the same.

A series of drive/brake tests were carried out under different slip angles (SA), in-

clination angles (IA), inflation pressure (P), and normal wheel loads (L). First, if the strict "in-plane" response requires the slip angle must be zero to confine the motion in the wheel plane. The measurements under non-zero slip angles should be categorized to so-called "combined slip responses" according to Pacejka [4]. Therefore, the measurements under the SA=0 condition are used for the following model validation for in-plane response. Second, Fig. 6.4 (a) and (b) were measurements when the inclination angle IA=0 and IA=4 respectively, and all remaining conditions were kept the same. The changes of inclination angle does not affect the longitudinal force F_x. The role of inflation pressure in the drive/brake test is similar to the one in the cornering test. The influence of inflation pressure on F_X is much smaller than the effect caused by the normal wheel load as compared between (a) and (c) or between (b) and (d) in Fig. 6.5

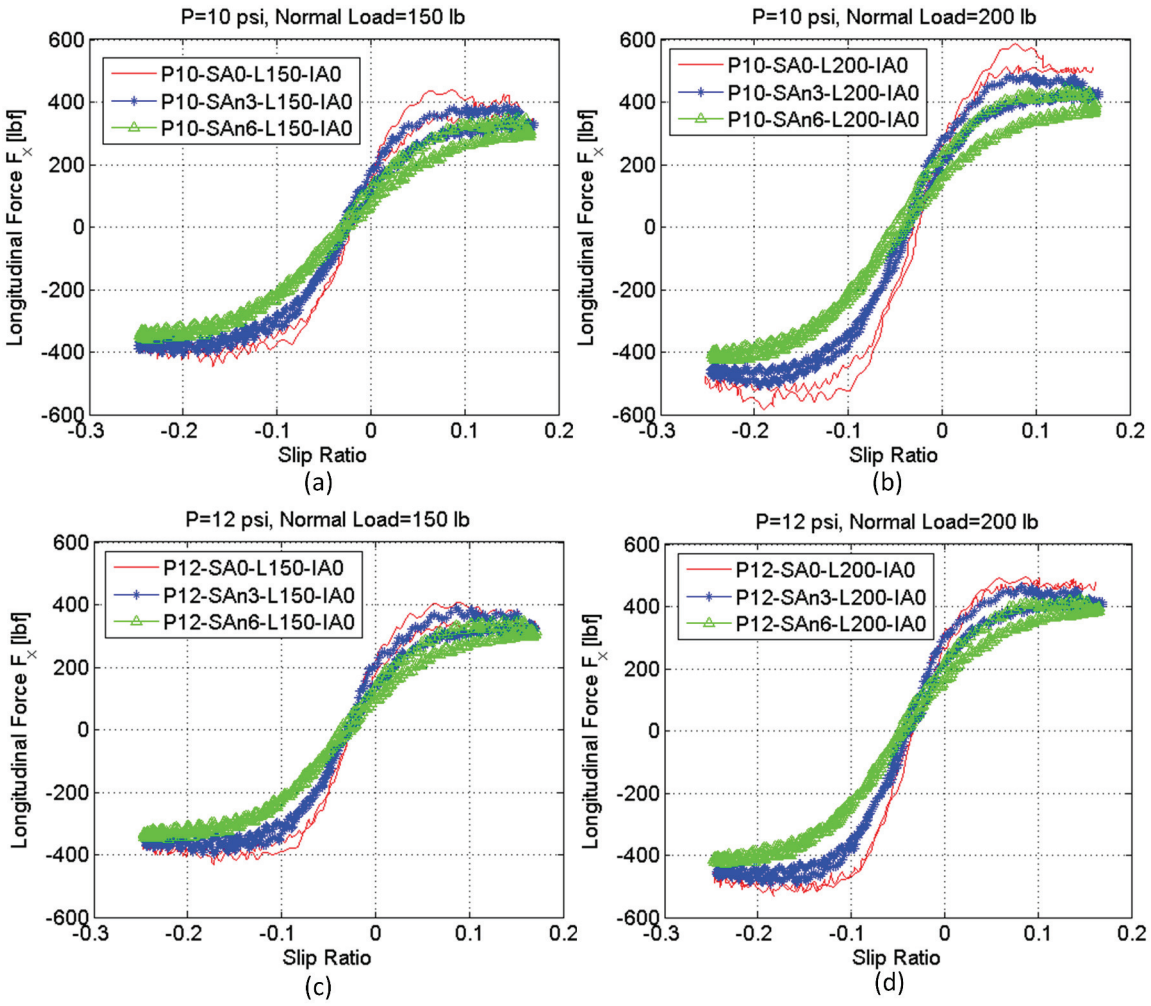

Figure 6.5: Drive/brake response test data of the Hoosier LC0 tire

6.2.3 Validation plan summary

In summary, the camber(inclination angle) effect of the Hoosier LC0 tire is limited for both cornering and drive/brake tests and can be ignored. The inflation pressure is set to $P = 10psi$, which is the recommended value in practice for the FSAE racing, because the inflation pressure does not alter the response of either cornering nor drive/brake significantly. For both out-of-plane and in-plane response, the first priority is to capture the normal wheel load effect on the model. As discussed in the static load vs. deflection response, the possible wheel load for one Hoosier tire ranges from 150 to $200lbf$ taking the load transfer into account. The steady-state response is checked at two levels of the normal wheel load, $L = 150lbf$ and $L = 200lbf$ for both the cornering and drive/brake tests. For the drive/brake test, the in-plane response data under the condition of zero slip angle (SA=0) is used to validate the developed model.

The maximum shear force (F_Y or F_X) generated in the contact patch for both types of tests are nearly the same if the wheel load is the same as shown in Fig. 6.3 and Fig.6.5. The reason can be explained by the simple Coulomb theory. Under the circumstances of the entire contact patch entering the sliding zone, no matter how the tire is sliding (laterally or longitudinally), the overall shear force should achieve the same peak value given the same normal load. The test data agrees with the expectation. This established the foundation of estimating the coefficient of friction between the tread of the Hoosier tire and the Calspan flat-track surface, which has been discussed in Section 4.6. The detailed validation of the FE tire model is discussed in Section 6.4 and Section 6.5

6.3 FE Tire Model for Steady-State Analysis

The steady-state transport solver requires the input model defined by so-called streamlines in Abaqus. The streamlines are the paths that the material follows during transport through the mesh. To meet this requirement, the mesh must be generated using the symmetric model generation capability. More specifically, the 3D model must be created by revolving an axisymmetric model about its axis of revolution. The steps of modeling scheme is summarized in Fig. 6.6.

There are two types of the steady-state rolling kinematics and they are equivalent in terms of resultant tire forces. The first type is that the tire is spinning and moving forward at the same time, and the road is stationary. The other type is that the tire is spinning without any translation, but the foundation supporting the tire is moving backward, which corresponds the case when the tire is running on the flat-track test machine. The rolling kinematics of both types can be described using the mixed Lagrangian/Eulerian formulation with respect to a purposely defined coordinate system

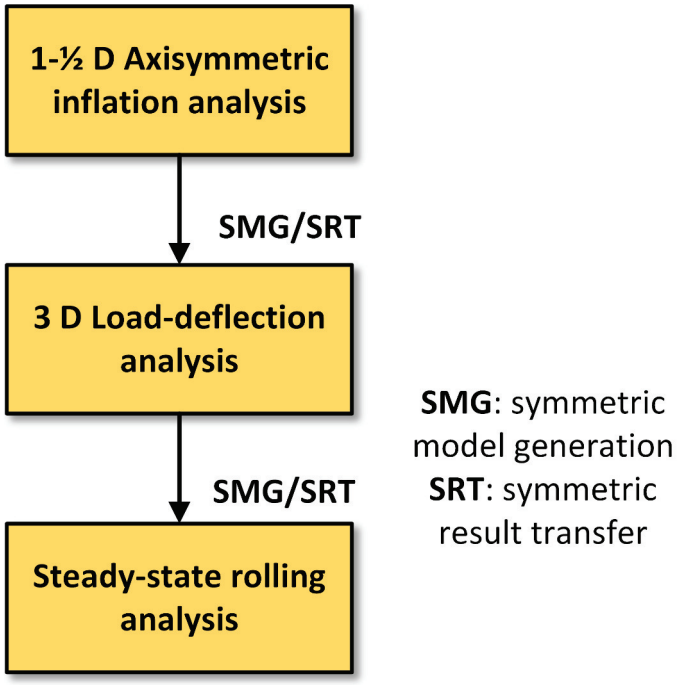

Figure 6.6: The work-flow of modeling a steady-state rolling tire in Abaqus. Modeling techniques such as symmetric model generation and symmetric result transfer are employed

which is attached to the revolution axle and only has translation for the steady-state rolling analysis. Notice that this coordinate system is also an inertia reference frame. For the first type of kinematics, the coordinate system attached to the revolution axle translates at velocity of v, and the road is stationary. Alternatively for the second type of kinematics, the coordinate system attached to the revolution axle has zero translation, and the road surface translates at velocity of $-v$. The constant spinning of the tire is described by the angular velocity ω for both types of steady-state rolling. Notice that this angular velocity also equivalently defines the transport of material passing though the mesh in the Eulerian description.

It is noted that the steady-state transport solver only accepts the model, boundary conditions (B.C.s), loads, and associated results from the previous static load-deflection analysis as shown in 6.6. Therefore, the symmetric result transfer technique (It should be distinguished by the general result transfer technique in Abaqus) must be used at the beginning of the steady-state transport analysis. The boundary conditions and loads in the static analysis will be propagated to the current steady-state transport analysis. For example, if the steady-state rolling tire under the vertical load $L = 150lbf$ is to be studied, the corresponding static load-deflection simulation results and associated B.C.s and loads, which have been discussed in Section

5.2.2 , need to be transferred to the current steady-state transport analysis. The boundary conditions and loads remain the same as in the static simulation step. The 'hard contact', which is introduced in Section 3.3.1, is used to model the normal contact behavior between the tire tread and the foundation. The theory describing the tangential behavior of the contact is discussed in Section 3.3.2. The model and parameterization of the tangential behavior for this research is developed in Section 4.6.

The translational velocity and transport velocity are two new B.C.s need to be prescribed. The road speed is $25mph$ for the Calspan flat-track for all the test conditions, so the translational velocity of the FE tire model (all nodes of tire model) is set to $v_0 = 25mph = 440in/s$. The transport velocity which equals the angular velocity ω of the wheel needs to be assigned for all nodes of the tire model too. Please note that the transport velocity should be a negative value for traveling forward (pointing to the same direction as X_T), if the sign convention of SAE J670-2008 is used. The next step is to search the reference spin velocity ω_0 for the given $v_0 = 440in/s$ to make the tire model entering free-rolling state. The criteria is the wheel torque T approaches 0 as discussed in Section 6.1.2. This searching step can be automated by using UMAT or Matlab. The reference spin velocity ω_0 is listed in Table. 6.2 for the case of vertical load $L = 150lbf$ and $L = 200lbf$ respectively. It is expected that the magnitude of ω_0 at $L = 150lbf$ is smaller than ω_0 at $L = 200lbf$ because the loaded radius decreases as the vertical load increasing. Both successive cornering and drive/brake tests start from the free-rolling condition.

Table 6.2: The reference spin velocities to achieve the free-rolling state for two vertical load conditions for the Hoosier LC0 18.0/6.0-10 tire model

	Inflation Pressure [psi]	Ground speed [mph]	Reference spin velocity [rad/s]
L=150	10	25	-51.53
L=200	10	25	-51.74

For the cornering test, there is a slip angle between the direction of heading and ground speed v_0 as shown in Fig. 6.7. The Abaqus global coordinate system is the Earth-Fixed Axis System (X_E, Y_E, Z_E) in the tire simulation. Since the wheel model is fixed with respect to the Abaqus global coordinate system in the previous static simulation, the Wheel Axis System (X_W, Y_W, Z_W) is always lined up with the Earth-Fixed Axis System. Also, the Tire Axis System (X_T, Y_T, Z_T) is always lined up with the Earth-Fixed Axis System as shown in Fig. 6.7 according to the way of determining the Tire Axis System via the Wheel Axis System. The ground speed/translational speed has a relative angle (equals the slip angle α) to X_T and X_E. The translational speed of the tire model has to be prescribed with respect to the Abaqus global coordinate system. Therefore, the component of the translational

speed along the Abaqus global X direction is $v_0 cos\alpha$, and the component of the translational speed along the Abaqus global Y direction is $v_0 sin\alpha$. The transport velocity is at ω_0 all the time. All the remaining B.C.s and loads are kept the same as in the static simulation.

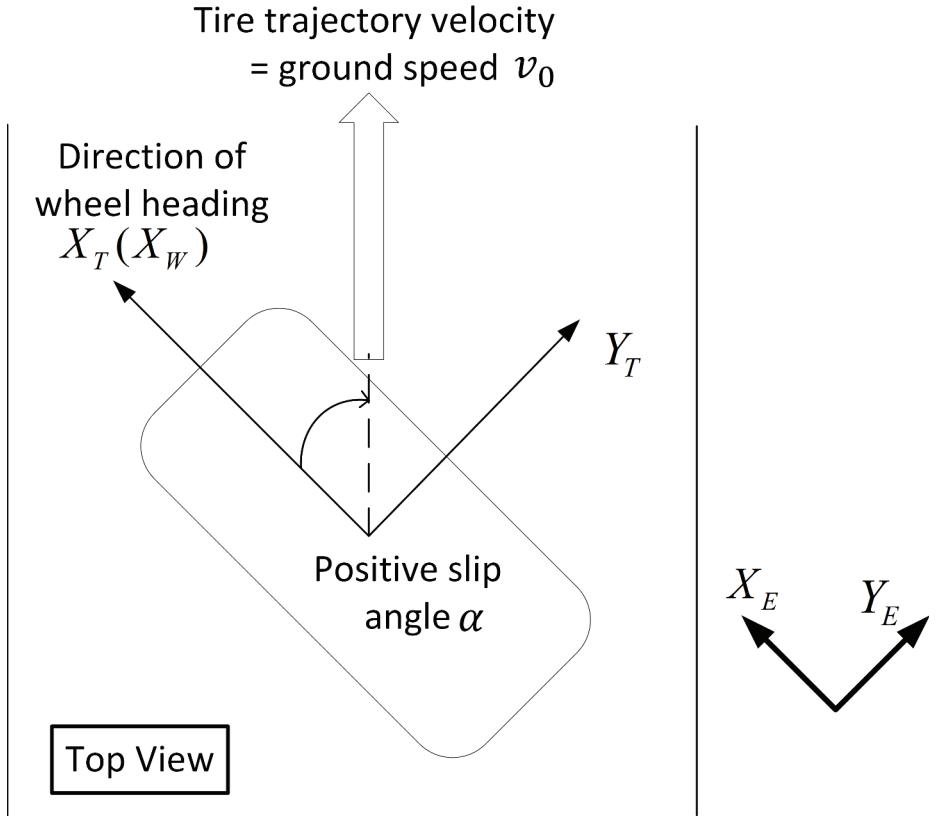

Figure 6.7: Schematic explanation on how to bring the slip angle into the model

For the drive/brake test, the desired longitudinal slip ratio is calculated based on the reference spinning velocity ω_0. It is not allowed to directly prescribe the desired longitudinal slip ratio to the FE model in simulation. Instead, the desired longitudinal slip ratio has to be converted to the corresponding spinning/angular velocity ω of the wheel, which equals the transport velocity in the Lagrangian/Eulerian method. The conversion can be done through Eqn. 6.3 following the SAE J670-2008 or through Eqn. 6.4 according to the convention of Calspan. The converted ω from the desired longitudinal slip ratio can be fed into the FE model for the drive/brake test. All the remaining B.C.s and loads are kept the same as in the static simulation.

The simulation steps for the virtual cornering and drive/brake tests are summarized in Table. 6.3.

Table 6.3: The simulation steps for the out-of-plane and in-plane response for the Hoosier LC0 18.0/6.0-10 tire model

Step Name		Description
Step-FreeRolling		Search ω_0 for the free-rolling condition
Step-Cornering	Step-Drive/brake	Cornering response at a given slip angle Drive/brake response at a given slip ratio

6.4 Validation for Out-of-Plane Response

The objective of the steady-state corning simulation is to obtain the out-of-plane solutions for the rolling Hoosier tire model. The tire can travel out of its wheel plane without appreciable slippage. That means the direction of wheel heading and of tire traveling may not be parallel. The angle between these two directions is called the slip angle α. The formal definition of slip angle appeared in Section 2.1.3. The out-of-plane traveling is the result of the tire laying down successive prints, each laterally displaced because of the sideways distortion of the tire. The word "slip" angle is somewhat of a misnomer. In fact, as long as in the elastic range of tire operation (small slip angle) little slipping occurs. The lateral force F_Y due to steady-state cornering comes from the sideways elastic distortion of the tire. Thus, the lateral force may be thought of as the result of the slip angle. The tire rolling on the Calspan test machine is controlled to sweep through a series of slip angles by slowly altering the wheel heading direction while maintaining a constant revolutionary speed. The resultant lateral force for each slip angle can be measured. The relationship between lateral force and slip angle is a critical characteristic to represent the tire's cornering performance.

Keep in mind that each data point on a curve of lateral force vs. slip angle is regarded and corresponds to one steady-state rolling state. Each run of a simulation using the steady-state transport solver in Abaqus only generates one data point of the curve. It is necessary to have several data points to form a full curve. The virtual cornering test requires several runs of steady-state transport analysis. In simulation, following the work flow illustrated in Fig. 6.6, the static load-deflection solution was transferred to the steady-state transport analysis through symmetric results transfer technique. When a tire is in cornering, it possesses not only longitudinal but also lateral velocity. Accordingly, one needs to prescribe the translational velocity with both components for the FE model.

The raw test curves in Fig. 6.8(a) show that different sweeping directions of the slip angle cause non-collapsed curve passing the $F_Y = 0$ line. The hysteresis phenomenon occurs again in the cornering test. This phenomenon also implies that when $SA = 0$ the lateral force F_Y is not necessarily zero, which challenges most of the tire models. It does not require to model this subtle hysteresis phenomenon of

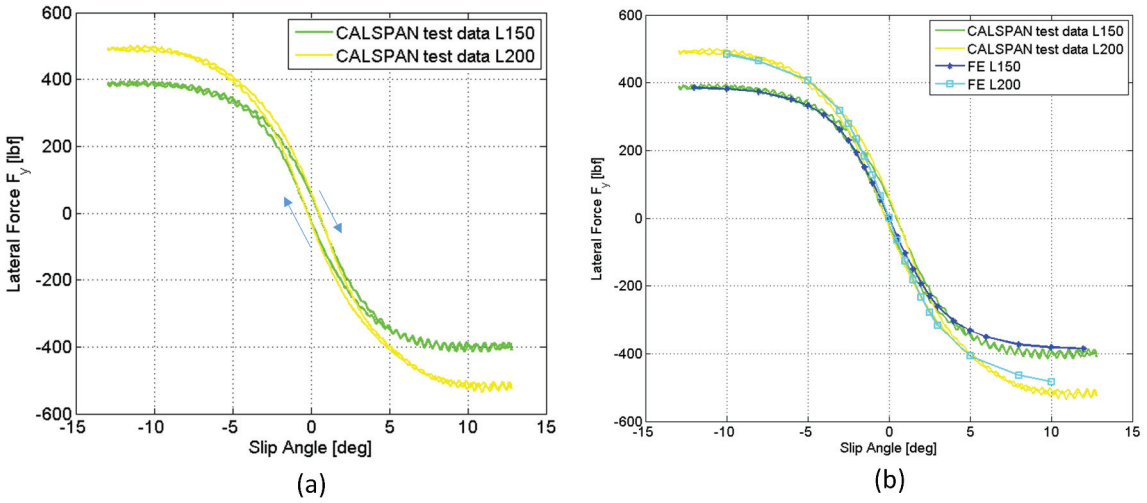

Figure 6.8: Simulation and test results on lateral force vs. slip angle for the Hoosier LC0 tire. (a) the raw test data exhibits a deviated path when the slip angle sweeps in a different direction for any given wheel load; (b) the results of FE model simulation are imposed directly on the raw test data

a rolling tire for the vehicle dynamics simulation. There are several common ways to avoid the problem. One method is collapsing two curves into one by averaging technique. By this way, the final curve will have a pleasant property that is $F_Y = 0$ at $SA = 0$. Another method is just picking one single curve at will. The Michelin tire company adopts the second method which is using a single curve to validate their models based on the author's knowledge. The single curve when slip angle varying from negative to positive is selected for further quantifying the performance of model's predictions.

Fig. 6.8(b) shows the simulation results against the original test data. Several comments are made on the simulation. First, since we obtain the solution at any given slip angle through steady-state analysis, the sweep direction of slip angle is not a factor in simulation at all. In other words, the steady-state analysis can only generate a single F_Y vs. SA curve. Second, the simulation technically gives out symmetric results for $SA > 0$ and $SA < 0$, which may not be true for the real test data.

The next step is to quantitatively evaluate the performance of the developed model based on the lateral force vs. slip angle graph. The evaluation metric is defined as

$$error\% = \frac{A_{sim} - A_{test}}{A_{test}} \times 100\% \tag{6.1}$$

where A can be geometrically interpreted as the area enclosed by the simulation or test curve and its independent variable axis. The percentage error is -2.9% for

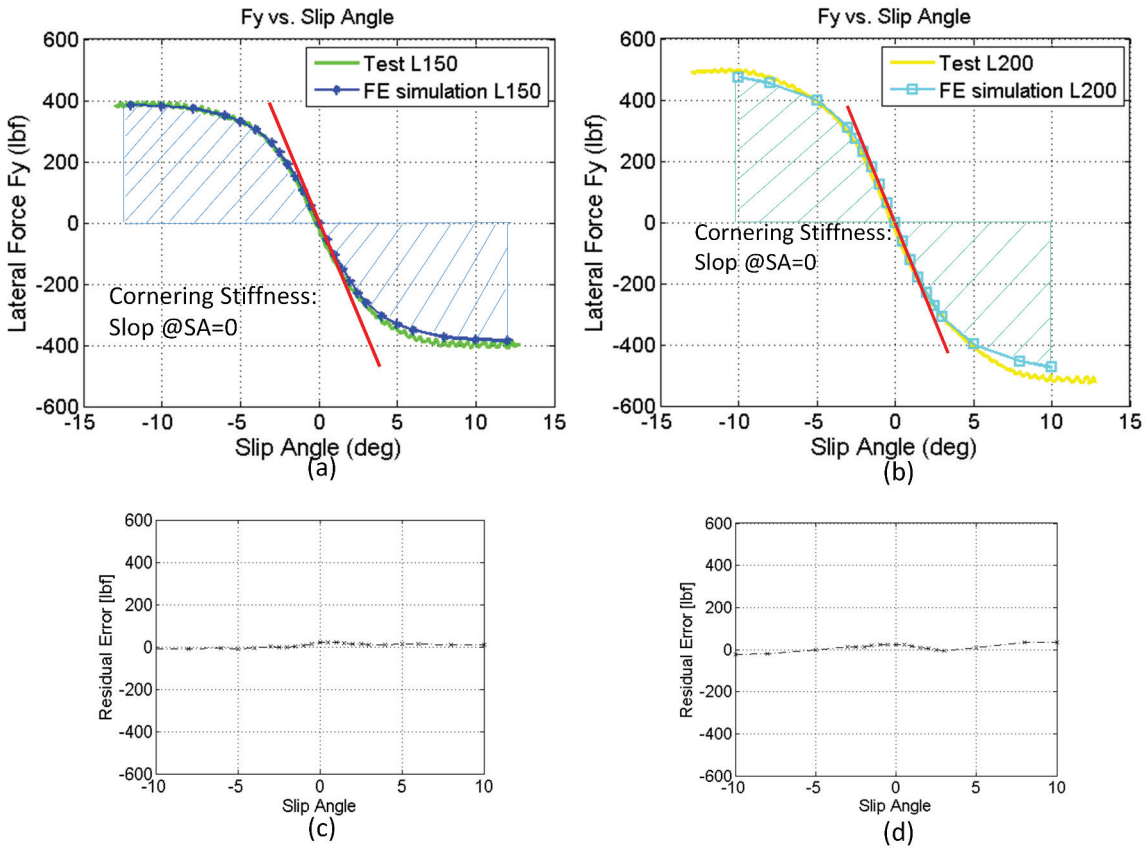

Figure 6.9: Quantifying of the model's performance based on the lateral force vs. slip angle graph for the Hoosier LC0 tire. (a) case L=150 lbf; (b) case L=200 lbf; (c) residual error between the simulation and test for L=150 lbf case; (d) residual error between the simulation and test for L=200 lbf case

$L = 150lbf$ case (Fig. 6.9(a)) and -2.7% for $L = 200lbf$ case (Fig. 6.9(b)). Figure 6.9(c) and (d) are residual plots between the simulation and test for both cases. It is seen that the mean of residual is nearly zero, which indicates the model predictions are not biased. When the slip angle is small, the response of lateral force is almost linear. Cornering stiffness is introduced to characterize the cornering behavior in the linear region. The cornering stiffness is defined as the slope of curve at the point $SA = 0$. In Fig. 6.9(a) and (b), the slope is illustrated by the straight line in red. The cornering stiffness obtained through the simulation is $\hat{C}_Y = 107.44lbf/deg$ and through the test is $C_Y = 115.55lbf/deg$, when the wheel load is $L = 150lbf$; If the wheel load increases to $L = 200lbf$, the cornering stiffness estimated through the simulation becomes $\hat{C}_Y = 128.18lbf/deg$ and through the test curve is $C_Y = 125.48lbf/deg$. Increasing the wheel load leads to a greater cornering stiffness at a given traveling speed, which causes the rolling tire harder to steer. This phenomenon is common for

all kinds of pneumatic tires.

6.5 Validation for In-Plane Response

The rigorous definition of the longitudinal slip ratio is provided first. As discussed in Section 6.1.2, for a given constant ground speed v_0 there is a unique wheel angular speed ω_0 to enable a tire being the free-rolling state. If the revolution speed increases i.e. $\omega > \omega_0$, at least part of the contact patch has relative slipping to the ground, and a non-zero net shear force is generated in the same direction of heading. So the tire enters a so-called drive mode. Similarly, if $\omega < \omega_0$, a non-zero net shear force also occurs but in the opposite direction of travel, the tire enters a so-called brake mode. A quantity κ called the longitudinal slip ratio is proposed to describe the kinematic relationship between v and ω. In the free-rolling condition, the "effective rolling radius" of a free-rolling tire is defined by dividing v_0 by ω_0,

$$R_e = v_0/\omega_0 \tag{6.2}$$

The longitudinal slip ratio κ or S_X according to the SAE J760-2008 standard is defined as,

$$S_X = \frac{\omega - \omega_0}{\omega_0} = \frac{\omega}{\omega_0} - 1 = \frac{\omega R_e}{v_0} - 1 \tag{6.3}$$

Notice, the definition of effective rolling radius has been used. The slip ratio at special rolling conditions is examined. The slip ratio at the free-rolling condition is $S_X = 0$ because $\omega R_e/v_0 = 1$; The condition for a locked wheel written in terms of the longitudinal slip ratio is $S_X = -1$ because $\omega = 0$; for an ideal extreme case when $\omega \to \infty$, then $S_X \to \infty$. The road contact shear force (longitudinal tire force F_X) is a function of slip ratio and could be either a tractive force or braking force. Strictly speaking, when $S_X = 0$, F_X is not zero (FBD in Fig. 6.1) and is right the rolling resistance force. Since F_X at $S_X = 0$ is so small (a hundredth of a vertical wheel load), it is typically approximated to zero for the purpose of vehicle dynamics.

There are several other definitions for the longitudinal slip ratio commonly used in industry. The Calspan TIRF uses the loaded radius R_L instead of R_e to define the slip ratio SR because R_e is much harder to measure than R_L especially on an instantaneous basis.

$$SR = \frac{\omega R_L}{v_0} - 1 \tag{6.4}$$

The symbol "SR" in Eqn. 6.4 is to distinguish the SAE definition. A significant difference in using the Calspan definition and SAE definition to evaluate the F_x vs. longitudinal slip ratio relationship is that in Calspan definition $SR = 0$ does not give $F_X = 0$ anymore. Although we introduced the longitudinal slip ratio under the circumstance of steady-state straight line rolling, the concept of slip ratio is still

applied in general transient scenarios. For example, it is widely used in anti-lock brake system studies but more difficult to measure or estimate.

It is noted that for all rolling states in the Calspan drive/brake tests, neither acceleration nor deceleration is involved, although terms like "brake" or "drive" are used.

In simulation, following the work flow illustrated in Fig. 6.6, the static load-deflection solution was transferred to the steady-state transport analysis through symmetric results transfer technique. The effect of vertical wheel load was examined at two levels, 150 and 200 lbf. It is recommended to set the coefficient of friction to zero for the load-deflection analysis first, then vary it from zero at the beginning to its final value at the end during the steady-state transport step. This procedure makes the frictional force gradually added during the analysis, which helps the convergence of a solution. For the virtual drive/brake test, different slip ratio conditions are achieved by fixing the translational road speed at $v_0 = 25mph$, at the same time varying the transport velocity of spin from $\omega < \omega_0$ to $\omega > \omega_0$ to cover the braking, free rolling, and driving regions.

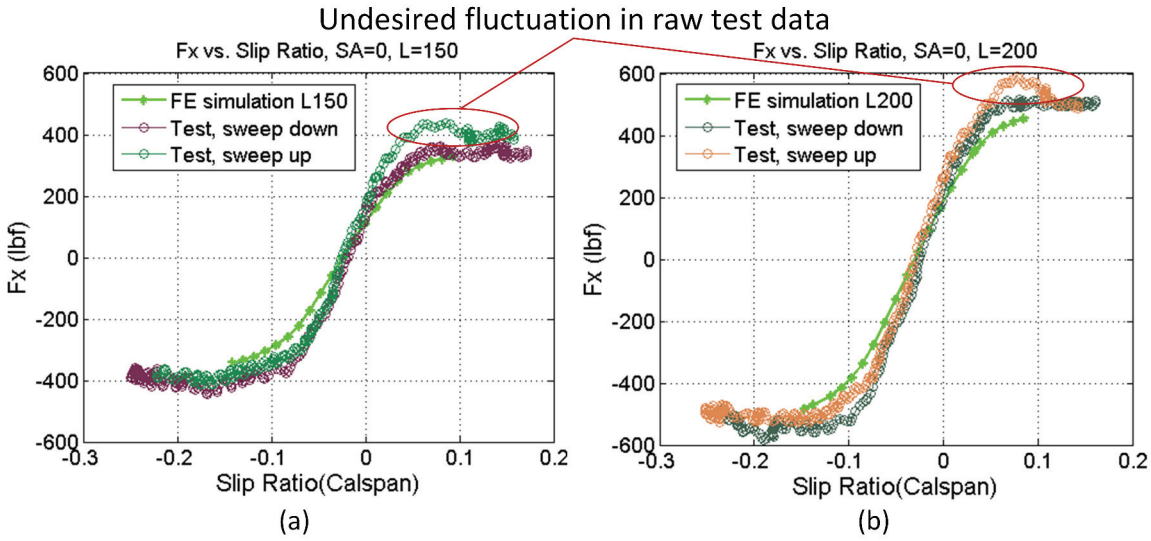

Figure 6.10: Simulation and test results on longitudinal force vs. slip ratio (Calspan definition) for the Hoosier LC0 tire. (a) case L=150 lbf; (b) case L=200 lbf.

The raw test curves in Fig. 6.10 were obtained by sweeping the slip ratio from positive to negative (downward) then back to positive (upward). It is observed that the sweep direction caused some differences in the measurement of F_X. As an example in Fig. 6.10 (a), the measurement of F_X when the slip ratio is changing from 0.03 to 0.1 (upward) significantly deviates the record of F_X when the slip ratio is changing from 0.1 to 0.03 (downward). The similar phenomenon can be observed in Fig. 6.10 (b) too. The drive/brake test data seems less smooth than the cornering data because

the drive/brake test needs more sophisticated control of the test machine than the cornering test. The precise control of the road speed to match the slowly changing (to guarantee the steady-state condition) wheel spinning speed is required to achieve the desired longitudinal slip ratios. The cornering test requires maintaining a constant road speed. The test machine has two d.o.f to control for the drive/brake test and one d.o.f for the cornering test. The deviation of measurements is mainly caused by the testing system.

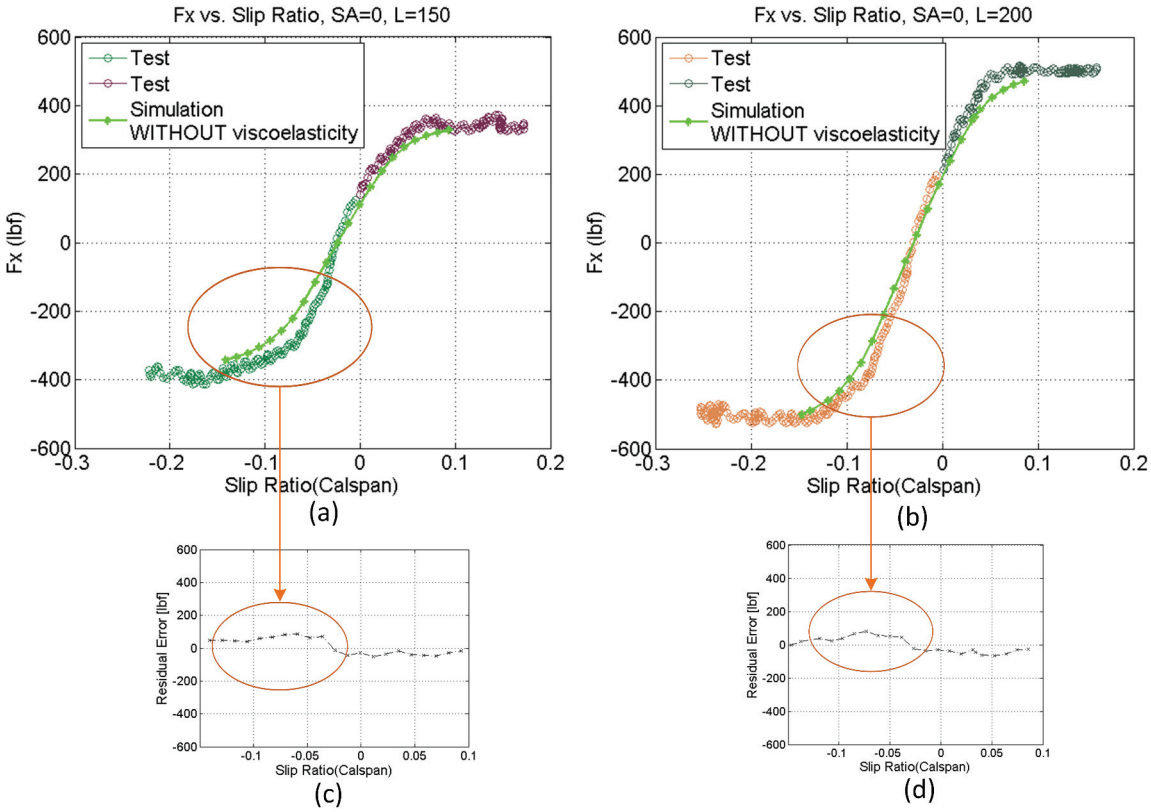

Figure 6.11: Quantifying the model's performance based on the longitudinal force vs. slip ratio graph for the Hoosier LC0 tire. (a) case L=150 lbf; (b) case L=200 lbf; (c) residual error between the simulation and test for L=150 lbf case; (d) residual error between the simulation and test for L=200 lbf case

To quantify the model's in-plane performance, we have to work on a single test curve as a baseline. As in Fig. 6.11 (a) and (b), the single test curve consists of a portion ($SR < 0$) of upward sweep data and a portion ($SR > 0$) of downward sweep data. The raw data of F_X in Fig. 6.10 has severe fluctuation which is likely caused by the test machine but not the tire performance, when the slip ratio is changing from 0.03 to 0.1(upward). Therefore, it is reasonable to exclude the fluctuated test data for the purpose of validation. The simulation can only predict a single smooth

Table 6.4: The statistics for evaluation of the steady-state response of the FE tire model

	Cornering		Drive/Brake	
	$L = 150lbf$	$L = 200lbf$	$L = 150lbf$	$L = 200lbf$
$error\%$	-2.9%	-2.7%	-17.5%	-12.1%
mean of residual	6.53	10.71	11.40	-3.75
standard deviation of residual	10.52	16.14	50.05	46.36

response curve with no distinction on the sweep direction of slip ratio. Each data point on the simulation curve is a steady-state solution. The difference between the simulation and test is evaluated by the same metric given by Eqn. 6.1. For the case L=150 lbf, the model prediction against the test is visualized in Fig. 6.11 (a), and the distribution of residual error is displayed in Fig. 6.11 (c). The percentage difference is -17.5%. For the case L=200 lbf, the model prediction is compared to the test in Fig.6.11 (b), and the distribution of residual error is displayed in Fig. 6.11 (d). The corresponding percentage difference is -12.1%. It can be seen that the most deviation between the prediction and test curves happens when the slip ratio is falling in the region $(-0.1, -0.05)$, which contributes significantly to the percentage difference. That is probably due to the quality of test data rather than the behavior of the FE tire model.

6.6 Validation Results Analysis

The predictions of models always possess point reflectional symmetry. e.g. the lateral force subjected to a positive slip angle has the same magnitude with the lateral force subjected to a negative slip angle but opposites in direction. The symmetry comes from the symmetry in geometry, material properties, B.C.s, and loads of the model. On the other hand, the real test data exhibits non-symmetric behaviors due to intrinsic tire properties arising from asymmetries in tire material, construction, or geometry caused by the manufacturing irregularities. The non-symmetric behaviors introduce the so-called "tire pull forces" according to SAE J670-2008 [3]. The largest $error\%$ in Table.6.4 is caused by the non-symmetric behavior of the tire if one examine Fig. 6.11 (a) and (c).

The tire-road contact model influences the performance greatly. The friction model and parameterization used in this research is limited by the available test data. The model prediction may be improved by employing advanced friction model or having more specific friction data associated with the surface of the test machine to characterize the tire-road interaction.

The measurement protocol and test facility impact the test data. The different measurement protocol may cause noticeable measurement result for the same tire. This factor should also be accounted for the evaluation of the model's performance.

The contact pressure distribution for several typical rolling conditions are shown in Fig. 6.12. It is observed that the contact pressure averagely is $10psi$ in the center region of the contact patch, which is indicated by light blue in the contour plot for each rolling case. The inflation pressure is $10psi$ which makes the simulation results reasonable. It is noted that Fig. 6.12(a) is the same as Fig. 5.10(a) except the changed limits of the color scale.

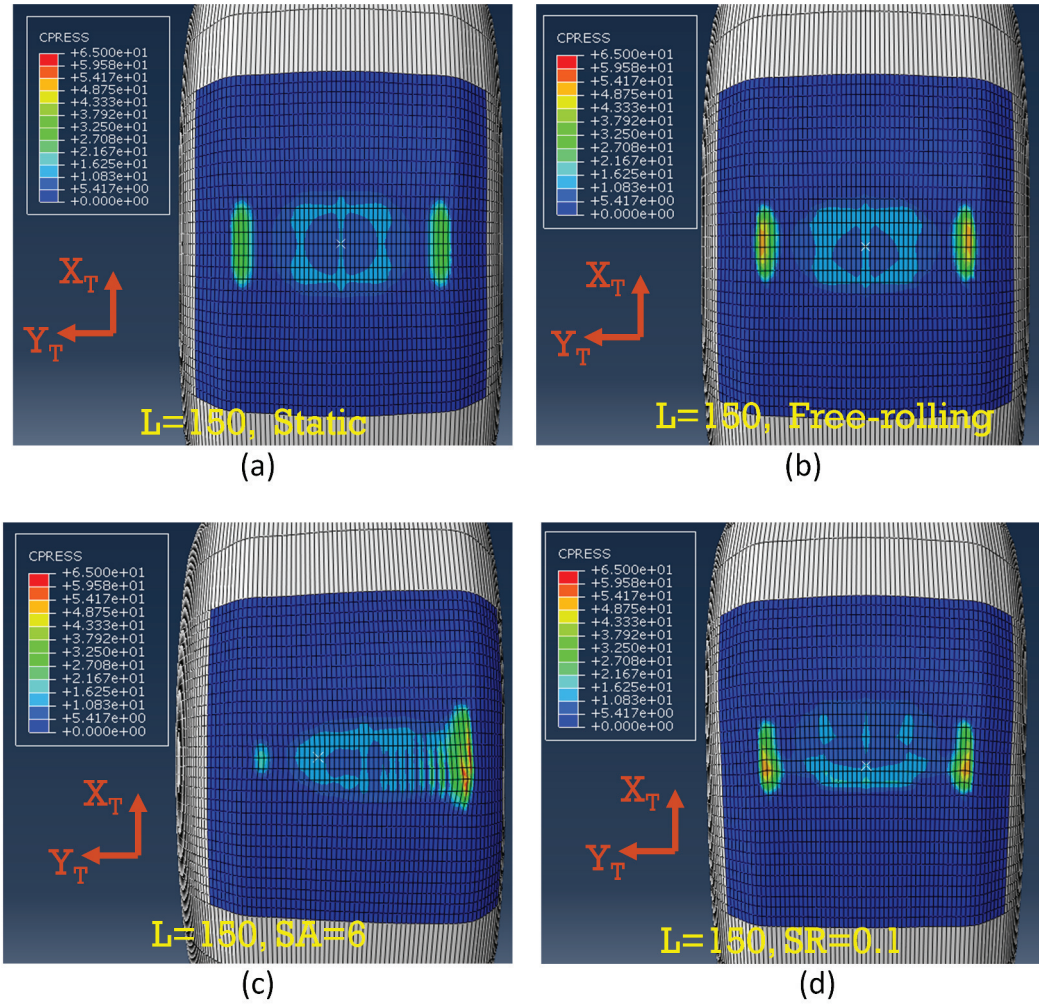

Figure 6.12: The contact pressure distribution in the contact patch for different rolling conditions: (a) static; (b) free-rolling; (c) cornering mode; (d) drive mode. The inflation pressure P= 10 psi and wheel load L= 150 lbf for all cases

Chapter 7

Modeling Study for Dominant Tire Mechanics

In this chapter, the dominant mechanics of the Hoosier LC0 tire response is highlighted by exploring the FE model on different levels. The purpose of exploring the model is to provide a solid foundation to support future full-vehicle simulation. In addition, a series of numerical studies was carried out to help understanding of various effects on the tire response.

7.0.1 Mechanics in Inflation Response

The equilibrium shape of an inflated tire without any external load is the most basic response, which is axisymmetric. The carcass which embeds the fiber network dominates the final equilibrium shape. The molded shape of the carcass and reinforcement fiber arrangements (e.g. fiber spacing, crown angle, and elasticity etc.) dictate the static inflation response. In contrast, the tread and sidewall rubber attached on top of the carcass do not significantly affect the equilibrium shape. The cords of the fiber network are in tension mode to balance the load induced by inflation pressure. This is the reason behind the PHB theory [38] which does not take the rubber elasticity into account for the problem formulation. Consequently, a conclusion can be made that one can infer little if any elastic response in the tire rubber from the inflation response.

7.0.2 Mechanics in Static Load-Deflection Response

When a tire is subject to a vertical wheel load, the sidewall will be bend outward (the section width will be widened). The bending stiffness of the sidewall together with the function of inflation air pressure plays a role affecting the sidewall deformation and further the total amount of tire deflection. The root sidewall sub-section (transition region between the sidewall and bead section) of the Hoosier LC0 tire is significantly stiffer than the remaining sidewall and tread sections. The carcass plies turn around the bead, and their tails form extra reinforcement layers in addition to the original carcass layers. A portion of the bead filler (hard rubber) bonds those layers together and further enhances the stiffness of the root sidewall sub-section. The model's description on stiffness distribution of the root sidewall region significantly dictates the simulated tire spring rate. As a comparison, some researchers [39] estimated the effect of extra layers by stating that "Youngs modulus from the bead area to the middle of the sidewall is roughly double the modulus observed in the other locations" based on the classic lamination theory. The treatment of doubling the elastic modulus is not very sound and relies more on human experience. Instead, the present work explicitly models the additional layers of fiber network. The vertical stiffness

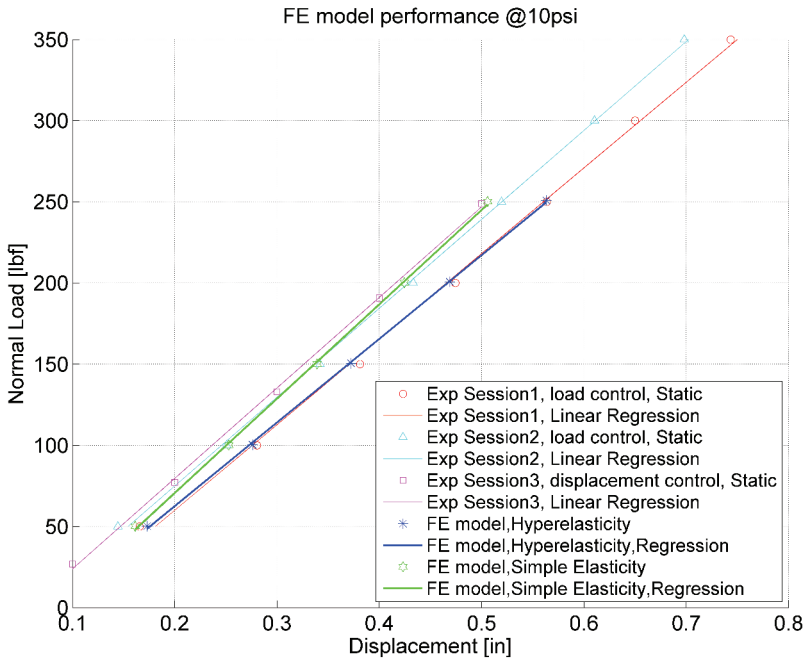

Figure 7.1: The effects of adopting simple linear elastic and hyperelastic material model on the vertical stiffness of Hoosier tire

of a pneumatic tire does not merely rely on its structure but more importantly the contribution of inflation air pressure. If one multiplies the inflation pressure by the

area of the contact patch, the result is close to but less than the vertical wheel load, which has been discussed in Section 5.2. Whereas the remaining difference is regarded as the load bearing by the tire structure. The tire structure itself only accounts for about 10% to 15% of the load carrying capacity [32]. Furthermore, most of the load carried by tire structure is carried by the tension of reinforcement fibers. That is why the material nonlinearity of rubber has such a small influence on the tire vertical stiffness, and why the tire behaves just like a linear spring in the vertical direction. An interesting numerical experiment was conducted to show the influence of material nonlinearity of rubber on the vertical tire spring rate. According to the linearization theory of the Yeoh form(recalling Eqn. 4.27), the initial shear and Young's modulus are

$$G_0 = 2C_{10}, E_0 = 6C_{10} \tag{7.1}$$

Instead of the Yeoh form, if we use the simple linear material model (Young's modulus $E_0 = 6C_{10}$, Poisson's ratio $\nu = 0.495$ not ideal 0.5 which may cause numerical problem) for rubber, its effect on the tire global load vs. deflection response is shown in Fig.7.1 indicated by a line in light green. The new prediction overestimates the tire spring rate by 15%. The explanation of this result is derived as below. From DIC measurements, the strain magnitude in the sidewall region can achieve up to 8% and the stress-strain curve of Hoosier rubber already exhibits nonlinearity. The initial Young's modulus (at strain=0) is greater than the actual tangential modulus (at strain= 8%). This causes the overestimation of the tire vertical stiffness. However, the nonlinearity of rubber has limited influence on the linear behavior of the tire subjected to a vertical wheel load.

7.0.3 Mechanics in Steady-State Response

It is commonly accepted that the viscoelasticity of rubber material does not affect much about the tire global forces. However, a rigorous study addressing the contribution the contribution of the viscoelasticity of the rubber materials on the global tire forces is rarely seen. The following numerical experiments make a further step to evaluate this statement. The FE tire model takes advantage of being able to carry out virtual tests by ideally adding or subtracting the rubber viscoelasticity, which can never be fulfilled by any physical test.

By the time of composing this dissertation, the author did not have any viscoelastic data for the Hoosier rubber. Instead, the viscoelasticity of a similar type of ASTM reference rubber is available at hand. Then the time-dependent material data of the ASTM reference rubber was added to the hyperelastic material model of the FE tire model and remain the elasticity of the Hoosier rubber the same as previously tested. Specifically the Prony series of the ASTM rubber which include a series of dimensionless shear relaxation coefficients and their corresponding relaxation time constants are listed in Table. 7.1. The purpose of this study is to check the effect of

Material Name	parameter
Rubber(ASTM-Ref)	viscoelasticity (Prony series) $\bar{g}_1^P = 3.22 \times 10^{-1}; \bar{g}_2^P = 1.25 \times 10^{-1}; \bar{g}_3^P = 8.93 \times 10^{-2}$ $\tau_1^G = 1.86 \times 10^{-5}; \tau_2^G = 1.81 \times 10^{-4}; \tau_3^G = 1.60 \times 10^{-3}$ $\bar{g}_i^P$ are dimensionless shear relaxation moduli; τ_i^G are time constants for shear relaxation in [sec]

Table 7.1: The time-dependent properties used in the tire model

viscoelasticity qualitatively not quantitatively.

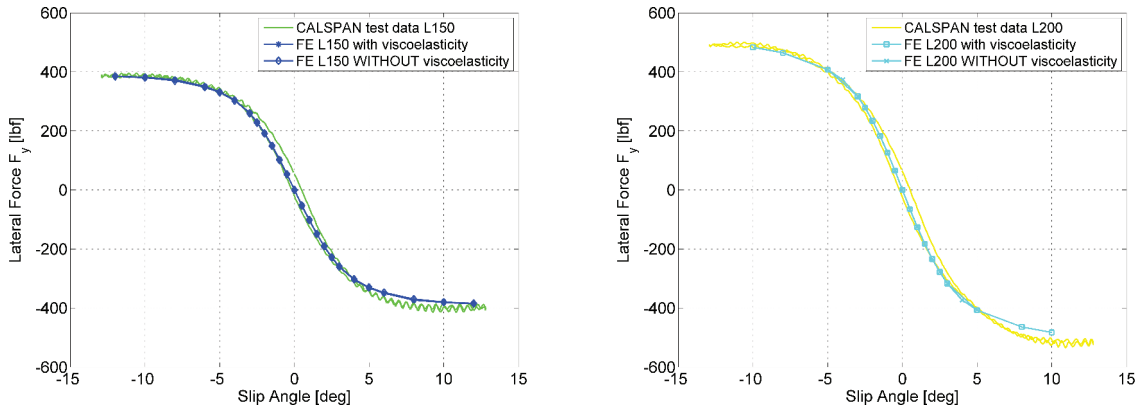

(a) (b)

Figure 7.2: The effects of rubber viscoelasticity on the cornering performance of the Hoosier LC0 tire when it is subjected to a wheel load (a) L=150 lbf; (b) L=200 lbf

For a cornering test, the simulation results between the model in Chap.6 and a modified model which differs by adding the time-dependent material property are compared in Fig. 7.2(a) and (b). It is seen that the difference of lateral force response is not distinguishable particular in a sense of vehicle simulation. For the in-plane drive/brake test, the difference of simulated response of the longitudinal force induced by considering the time-dependent material property is not negligible as shown in Fig. 7.3.

In consequence, the following analysis is trying to explain why the viscoelasticity impacts the in-plane response of a rolling tire. A rolling cylinder model with simple geometry is borrowed from Oden's paper [40]. The dimensions and property parameters associated with Oden's model is widely used as a benchmark. Therefore, adopting Oden's model for a numerical study here makes it convenient for other researchers to repeat the analysis. The model depicts steady-state rolling of a deformable hollow cylinder against a flat rigid surface. The length of the cylinder is so large that the

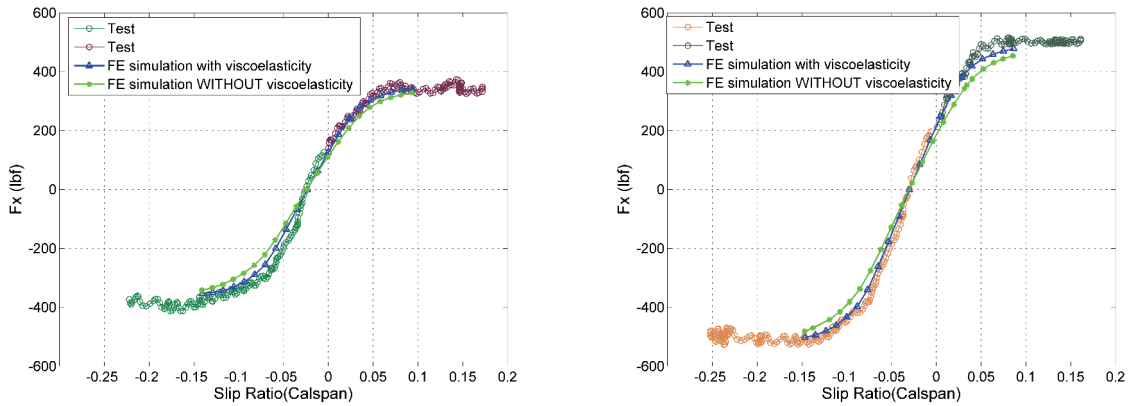

Figure 7.3: The effects of rubber viscoelasticity on the Drive/Brake performance of the Hoosier LC0 tire subjected to a wheel load (a) L=150 lbf; (b) L=200 lbf

plane strain assumption is valid through the direction of rolling axle. The parameter set adopted in the current numerical study is summarized in Table. 7.2

The cylinder is displaced a distance $\Delta = 0.3in$ against the foundation to establish a contact pressure. Then a steady-state transport analysis step is followed to simulate its spinning at a constant revolution speed $\omega = 2.5rad/s$. Friction is neglected so that no translation happens. Two simulation cases are compared where pure elastic and viscoelastic material effects are considered respectively. All other factors in the simulation are kept the same for both cases. The result in Fig.7.4(a) where the pure elastic material (Mooney-Rivlin model) is used shows a symmetric deformation mode with respect to a vertical centerline. Whereas if the viscoelastic material (adding time-dependent property to the same Mooney-Rivlin model) is used, the response exhibits a non-symmetric deformation mode as in Fig.7.4(b). For a perfectly elastic material, the deformation is reversible. A material entering the contact zone passing through the leading edge is compressed then completely relaxes when leaving the contact zone. So the deformation is symmetric. For a viscoelastic material, the compression and relaxation process are no longer instantaneous but requires a finite time to complete. In addition, a certain amount of energy is lost during the compression-relaxation cycle. The deformation is not reversible and consequently non-symmetric, which is the key reason for the viscoelasticity affecting the resultant normal and longitudinal forces.

Since the stress in a viscoelastic material is influenced not only by the strain but also the rate of strain, the deformation depends on the angular velocity of the rolling cylinder. In consequence, the resultant force becomes a function of the angular velocity. An illustration of the relationship between the resultant normal force and angular velocity is provided in Fig. 7.5. Keep in mind that the foundation surface is

Table 7.2: Parameter set of Oden's cylinder model used in current numerical study

Parameter	Value	Parameter	Value
Outside radius of cylinder, R_o	2.0 [in]	RUBBER: long-term elastic modulus, Mooney-Rivilin C_{10}^0, C_{01}^0	80, 20 [psi]
Inner radius of cylinder, R_i	1.0[in]	Shear relaxation coefficient, g_1^P	0.2
Deflection, Δ	0.3[in]	Relaxation time, τ	0.1 [sec]
Angular velocity of AXLE, ω	varying	Friction coefficient, μ	0
		Mass density, ρ	0.036[lbf-s^2/in^4]

frictionless in order to isolate the effect of viscoelasticity. When the angular velocity is small, the deformation is almost symmetric and the normal reaction force acts along the centerline. If the angular velocity increases beyond a certain value, the asymmetric deformation is of a scale to significantly affect the normal reaction force which shifts a distance e from the centerline. Therefore, an additional moment around the spinning axle is generated accordingly. When the angular velocity achieves high level, the time period of one revolution is much less than the relaxation time constants of the viscoelastic material. In this case, material has no time to respond to the sudden change of state during the compression-release cycle. Then the deformed shape approaches symmetry again, and the rolling moment decreases. As the angular velocity increases, the viscoelastic material exercised by the deformation cycle gets more and more stiff. So the normal reaction force increases gradually if the amount of vertical deflection remains the same. On contrast, if the cylinder is made of pure elastic material, its deformation and resultant force are independent of the angular velocity. A numerical simulation using Oden's cylinder model was carried out to examine the trend of resultant normal force in Fig. 7.6(a) and rolling moment in Fig. 7.6(b) when the angular velocity changes from zero to $100 rad/s$.

Through these simulations based on Oden's model, one can find how viscoelastic material causes asymmetric deformation mode of a rolling body then influences the resultant force. For the in-plane response of the rolling tire, the mechanism caused by the viscoelasticity still holds. The time-dependent material property causes the asymmetric deformation of the tire in addition to the frictional effect. The unsymmetric deformation affects the resultant longitudinal force which is observed in Fig. 7.3 and has been explained. However, for the cornering performance the slip angle sweeping speed is much smaller than the rolling speed. So the viscoelasticity does not affect the resultant force in the lateral direction much. This is a possible explanation of the phenomenon observed in Fig. 7.2.

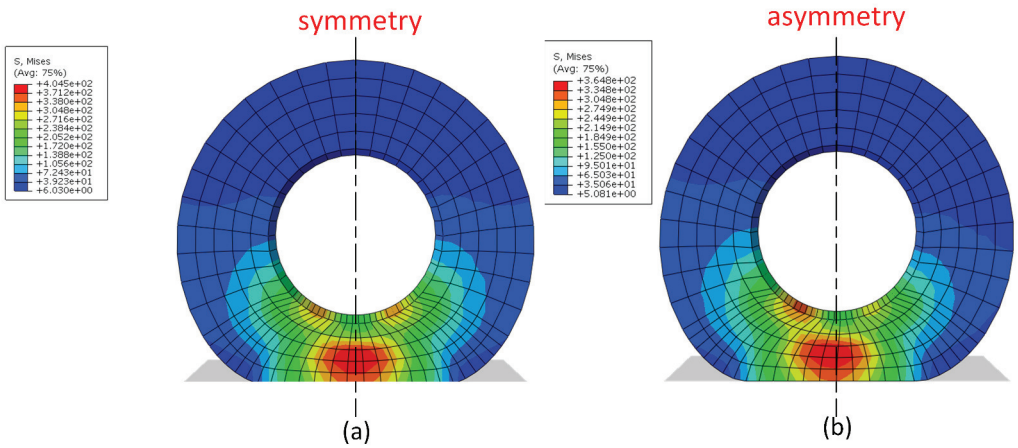

Figure 7.4: Elastic (a) and viscoelastic (b) material property effect on a deformable cylinder spinning at a constant angular velocity on a frictionless rigid surface

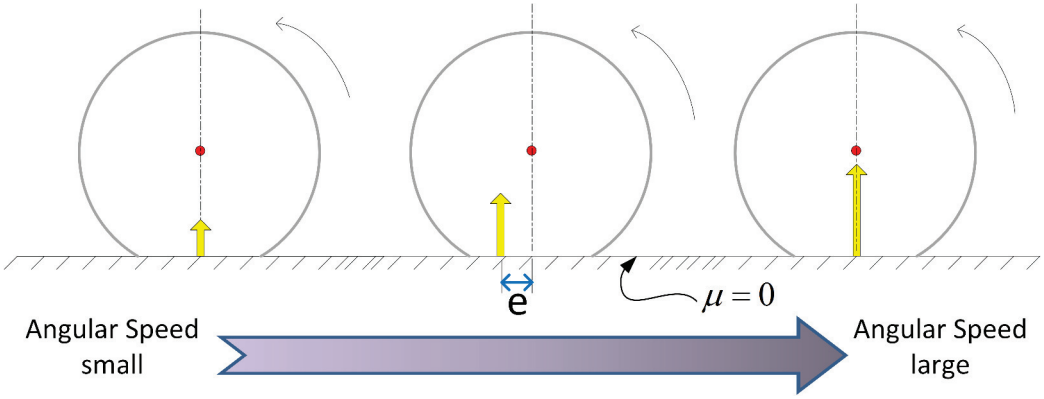

Figure 7.5: Illustration of normal reaction force varying with angular velocity for a cylinder made of viscoelastic material. Both the magnitude and action line of reaction normal force change.

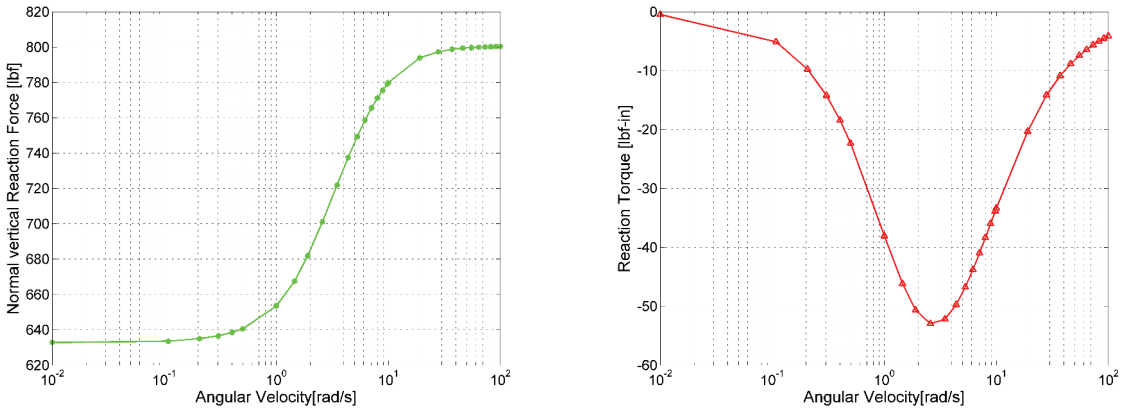

(a) (b)

Figure 7.6: Reaction force (a) and moment (b) as a function of angular velocity

Chapter 8

Summary and Future Work

8.1 Summary

The primary effort for this research was on developing the methodology of tire modeling by finite element method for full vehicle simulation from an existing tire product. The model's application domain (vehicle dynamics) requires that evaluating the model's outputs, i.e. tire forces and moments, on the wheel-hub level is the first priority. The local stresses and strains in the tire structure are not an immediate pursuit. A finite element (FE) approach is used because 1) for a given tire product, the parameters associated with a lumped-parameter tire model requires a series of full tire tests which are costly. The building of an FE tire model relies more on small-scale constitutive material tests and reduces the number of full tire tests. 2) the model becomes physical-based and more capable of describing the generation of tire forces and moments from a contact patch. The proposed finite element approach differs from the conventional FE method widely used for the purpose of tire design in its modeling concept and focus. The proposed approach is NOT mirroring each detailed structural component of a tire into a 3D numerical model in the computer. Instead, the core idea is to represent the stiffness, mass, and damping distribution of a tire in a particular "resolution" as long as the model's global responses can be satisfied. For example, the detailed FE model for the purpose of tire design reflects the real tire structure in the scale of $mm \times mm$ or even finer; while the proposed model reflects the real tire structure in the scale of $cm \times cm$. In consequence, the proposed tire structure model has reduced details with less the number of nodes and elements and is referred to as a "simplified" FE model. This is a key feature to enable a tire model being able to use for a full-vehicle simulation.

The material properties of various tire functional components are commonly inaccessible and proprietary to the tire producer. The difficulties of obtaining the material properties cause only a few research studies taking the FEM approach for the tire modeling for the vehicle simulation. The proposed way of model parameterization depends on a functional decomposition of the different tire components based on the purpose of each component. In practice, since the modeling work starts from a existing tire, not every component can be extracted. In other words, the parameterization is constrained by practical considerations. Some properties can be directly measured, other properties have to be estimated by solving the inverse problem. The model design and model parameterization are two aspects of modeling mutually influenced by each other, which is a key challenge and at the same time the value of the present work.

As a justification of the concept, a finite element model was developed for an existing bias-ply Hoosier LC0 18.0/6.0-10 racing tire without any data provided by the tire company. In Chapter 3, the concept of model abstraction and modeling considerations by FEM were explained. In Chapter 4, the modeling and parameterization were expanded in detail for both the tire structure model and the tire-road contact model. In Chapter 5, the FE tire structure model was validated through the quasi-static load vs. deflection tests which were carried out at Virginia Tech. The Chapter 6 is the validations of the developed model for steady-state responses. The test data was provided by the Tire Test Consortium (TTC) who contracted the Calspan Tire Research Facility (TIRF) to collect the Hoosier LC0 18.0/6.0-10 tire data in 2012. The specific accomplishments are outlined as below.

- Verified the axisymmetric model for quasi-static inflation response;
- Validated the full 3D model under varying static vertical load and inflation pressure to examine the load vs. deflection response within a 6% difference compared to the test data. The strain occurred on the sidewall of the deflected tire also matched the measurement with Digital Image Correlation (DIC) data;
- Validated the steady-state dynamic response of corning for slip angles between -10 and $+10$ under varying vertical loads within 5% difference compared to the test data;
- Validated the steady-state dynamic response of drive/brake for longitudinal slip ratios between -0.12 and $+0.1$ (slip ratio defined by Calspan) under varying vertical loads with about 10% difference compared to the test data.

It is noted that the full-tire test data was only for model validation, not for "calibrating" the model. The effectiveness of the model of the full-tire performance was demonstrated through a series of validations. The Chapter 7 analyzed the dominant mechanics of various responses by exploring the developed model through a several numerical experiments.

In Appendix A, the simulation techniques were discussed for a simple case to explore transient dynamics rolling studies. Since no experimental data, such as the classic cleat test, is available, the FE model was not validated up to the level of transient response. The emphasis is put on the study of simulation techniques required for the future full-vehicle dynamics simulation which involves four tire models simultaneously.

The present work is a first step to extend the FEM into the vehicle dynamics simulation beyond the rigid multi-body dynamics domain. Only a limited number of similar works have been published to date in the public domain. The significance of the developed simplified FE tire model are

- An approach has been used to develop material models independent of any tire supplier
- Model parameterization relies on small scale tests, and far less number of full tire tests are required than other vehicle simulation oriented commercial tire models;
- The simplified FE tire model approach is expandable to include more advanced thermal model and friction model besides the basic force and moment feature;
- Low cost. As an example, FTire/core solver (academic, network) license is available at 10,500 EUR (11,300 US dollars) and tire testing service for model parameterization is about 30,000 EUR (32,500 US dollars)

8.2 Conclusions and Results

The demands of a moderate-scale tire model to support full-vehicle simulation are emerging in the vehicle industry because the interaction between the tire and chassis is to be studied. It is not easy for the vehicle companies to acquire detailed tire properties which are proprietary information from the tire companies. One solution may be seeking the help from third-party tire model vendors e.g. FTire. Since the third-party model is of MBD-type, users have to pay not only the license but also the service for a series of full-tire tests to calibrate the model for a given tire product. The cost is high. This fact stimulates the present research to provide alternative solution approaches to build a tire model by the Finite Element Method which much loosely relies on the full-tire tests for model validation, not model development. So the cost becomes low. In addition, the model developed by the FEM is physical-based which provides more physical insights to the tire-chassis interaction. The main difficulty of adopting the finite element approach is what parameters are required and how to acquire the required material parameters. The first question is associated with the modeling approach, and the second question is associated with the method of

parameterization. The proposed methodology is to solve the problems of modeling and parameterization of a given tire product for the purpose of vehicle simulation.

The conclusion of this research is that the proposed methodology can be successfully applied to the modeling of the Hoosier LC0 18.0/6.0-10 tire and more generally bias-ply slick tires. The proposed approach has also demonstrated its utility in a practical sense. The proposed methodology mathematically represents the tire structure into the stiffness, mass, and damping matrices in the dynamic equation. The model has the potential for various application cases e.g. vehicle dynamics simulation and vehicle durability studies as long as the loads and boundary conditions are properly described.

8.2.1 General procedure of modeling a given bias-ply slick tire

As a result of the proposed methodology, the approach to modeling a given tire product are outlined:

8.2.1.1 Sample preparation

1. Prepare two tires of the same type. One is going to be decomposed and the other one is for further validation.

2. Cut one tire into two equal half sectors and make the cutting edge as clean as possible. The half sector is used to obtain the geometry and construction information from the exposed cross-section of the tire (e.g. Fig. 4.1)

3. Decompose the half tire sector into three major parts; the tread section, the sidewall section, and the bead section. (e.g. Fig. 4.6)

4. Peel off the carcass layers from the tread section and leave the pure tread rubber. The dog-bone shaped samples of the pure tread rubber can be obtained using ASTM standard dies. These samples will undergo the uniaxial tensile test which is the most common procedure (e.g. Fig. 4.8). If the biaxial or planar tensile test is allowed, the additional deformation mode test data can enhance the rubber material characterization.

8.2.1.2 Material Testing for estimation of material model parameters

1. Identify the appropriate hyperelastic model to describe the rubber material ("system identification", refer to Section 4.4.1). If uniaxial tensile test data is the only available data, Yeoh model is usually preferred but not necessary.

2. Examine the separated carcass-plies and understand the arrangement of reinforcement fiber. Some reinforcement fiber properties can be directly measured e.g. the spacing between the parallel fibers, the average diameter of each fiber, and the stack angles. If additional belt exists, the belt fiber/cord geometric parameters can be obtained in the same way. (e.g. Fig. 4.7 and Fig. 4.15)

3. The elastic property of the reinforcement fiber usually can not be directly measured because it is impractical to separate the single fiber to prepare a useful sample for testing. The elastic property of the fiber can be inferred by solving the inverse problem (e.g. Fig. 4.16) if the overall behaviors of the composites which contain the reinforcement layers are known. Several types of composites samples can be extracted from the tread section with different orientations e.g lateral or longitudinal (e.g. Fig. 4.14).

4. Study the structure of the sidewall according to the stiffness distribution. The sidewall rubber usually is just a thin layer of rubber which does not contribute much to the stiffness. While the turn-up carcass layers play a role in enhancing the stiffness of the root of the sidewall (e.g. Fig. 4.7). Modeling the extra reinforcement layers in the sidewall is a key to achieve the right stiffness.

5. The non-standard samples can be extracted from the bead section or bead-sidewall adjoint section. The test of those samples are not for accuracy but a rough estimation of the stiffness in that region which contains the effect of bead filler rubber. (e.g. Fig. 4.24 and Fig. 4.26)

6. The density of rubber can be measured and assumed to be uniformly distributed. If the reinforcement fiber is natural fiber, its mass can be neglected. The remaining mass mainly comes from the steel bead cords. (refer to Section 4.5.1)

7. The time-dependent rubber material can be measured through the Dynamic Material Analysis test to obtain the viscoelasticity of rubber.

8. The validation of material model can be carried out at the sample level. The corresponding virtual sample tests are used to check the performance of the selected material model and estimated parameters. (e.g. Fig. 4.20 and Fig. 4.23)

8.2.1.3 Tire simulation and validation

1. The FE tire model is partitioned according to the same way of decomposition of the tire structure. Therefore, the estimated material properties can be fed into the model.

2. Weigh the full tire on a scale to compare the weight calculated from the FE model. It is a simple step to check the mass distribution is whether or not properly represented. (e.g. Table 4.5)

3. The standard load vs. deflection test of the full-tire is highly recommended to validate the stiffness distribution is whether or not properly represented. (refer to Chapter 5)

4. To validate the steady-state dynamic response of the full-tire, the standard cornering test which characterizes the out-of-plane response of the tire and drive/brake test which characterizes the in-plane response of the tire are required. (refer to Chapter 6)

5. To validate the transient response of the full-tire, the cleat test is required to highlight the damping effect of the tire.

It is noted that the tire structure modeling is only one aspect for full-vehicle simulation. The other aspect is the tire-road interaction modeling which may contain more advanced thermal model, which is beyond the scope of this research. The proposed approach of tire modeling technically does not require full-tire tests for calibrating the model parameters. The FE tire model validations by full-tire tests are for demonstrating the reliability of the developed model.

8.3 Original Contributions

The original contribution of this research are

- Developed a methodology of modeling a pneumatic bias-ply tire by the finite element method (FEM) for vehicle dynamics analysis starting from a given tire product.

- Designed and applied a process for extracting necessary material properties to feed into the proposed FE tire model independent of tire providers for evaluating the tire model's performance in

  - Quasi-static load vs. deflection response
  - Steady-state dynamic response which contains out-of-plane and in-plane modes
  - Simple transient dynamic response: straight-line acceleration

  The method is practical for those who want to build their own tire models

- Proposed the framework of vehicle simulation in the elastodynamics domain using FEM

8.4 Future Work and Recommendations

There are a few steps to be studied towards the full-vehicle simulation. This research mainly focus on the first step. The next step is studying how to link four tire models into a vehicle model. The final goal is conducting full-vehicle simulation in the same finite element environment. The scheme is illustrated in Fig. 8.1

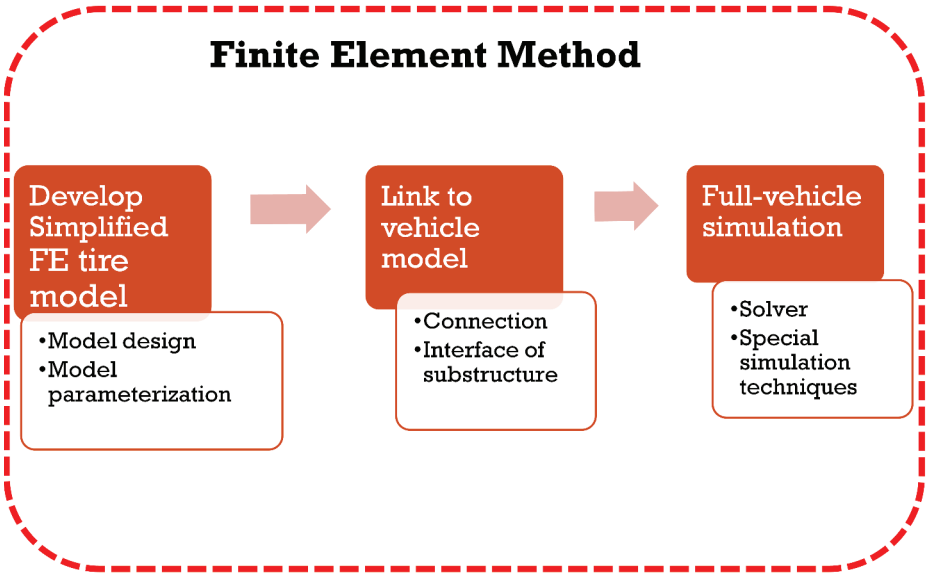

Figure 8.1: The FEM framework for vehicle simulation

Simulation of one rolling tire and four rolling tires are much different in terms of the simulation techniques. The solvers and simulation procedures have to be changed in Abaqus, which is discussed in Appendix A. When installing the tires into a vehicle model, the modeling approach to connecting the tire/wheel model to the suspension geometry needs to be considered. For example, in Abaqus a special kind of element called 'connector element' is right for this purpose, which is a much better way to model the wheel-hub connection than explicitly model the wheel hub joints. Initiate the full-vehicle dynamics simulation which may cover the straight line acceleration, deceleration as well as the cornering of the formula car model. Many advanced simulation techniques are required for these tasks. A possible solution to set a virtual environment for full vehicle simulation is to use explicit dynamic solver for both chassis and tire structures within the finite element framework. However, by this way it can never compete with MBD vehicle simulation in terms of computing speed. A better way can be implemented in Abaqus is utilizing 'Co-simulation' technique, which provides the capability of solving chassis dynamics by implicit solver with large time

increment and solving tire dynamics by explicit solver with smaller time increment. The 'Co-simulation' technique is quite new and needs much effort to be investigated for this application. Based on the virtual tire-suspension-chassis platform, one can study the interaction between the tire and chassis. Since the influences between the tire and chassis are mutual in real operation, the full-vehicle simulation will give out more realistic scenario and full performance of the tires than a traditional single tire simulation. Preliminary work toward modeling an integrated tire-suspension-chassis system by the finite element method has been started as shown in Fig. 8.2. The

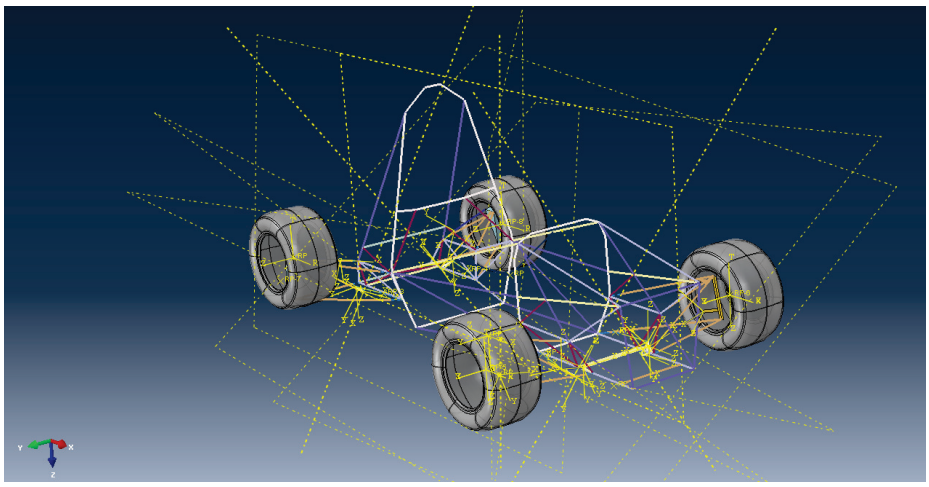

Figure 8.2: Finite element modeling of a VT FSAE 2012 vehicle including four tire models

future work toward this direction is more about vehicle dynamics, which includes but not limited to

- Develop a full-vehicle finite element model including tire models according to the VT FSAE formula car platform
- Establish the virtual environment for straight line acceleration and cornering simulation of the vehicle.
- Identify the load history and load transfer path from tire contact patch to suspension members

The other direction of future work is to enhance the model by bringing in more physics to expand the model's application range. The tire model developed by FEM can be expanded as illustrated in previous Fig. 3.1. The expansion mainly relies on adding or improving the constitutive relationships of materials or interactions. The current model did not consider any thermal effect. The thermal-induced stress itself does not much affect the global forces and moments. The thermal-coupled stress

analysis is still unnecessary for vehicle simulation. However, the temperature field in the contact patch will influence the frictional behavior between the tread and road. As a result, the tire forces will change with temperature. Therefore, incorporating a simple thermal model into the original Coulomb friction model might provide a meaningful improvement for the Hoosier tire model. This direction is more research oriented.

At the same time, studying how to save the computing time to improve the efficiency is also valuable. Adopting fast algorithm and keep decreasing the numbers of d.o.f of the model are possible ways to improve the computing speed.

It can be seen that many engineering efforts need to go into simulation, testing, and validation in this research area. The models are expected to be effective to enable operational analysis and design exploration for vehicle simulation in the future. A by-product of the developed model may be used to estimate parameters required by a MBD tire model through various virtual tire tests. This application is not novel and can be found in many published works.

Tire model users working in vehicle dynamics are still sticking to Pacejka's tire model and hesitate to accept the finite element method entering this area. The competitiveness of Pacejka's model comes from its magically simple form and capability in real-time applications. There is a trend that more physical-based tire models will be used for vehicle simulation because the demands of tire-vehicle interaction studies. The main reason to prevent the wide use of physical-based FE tire models is the time consuming computation. But keep in mind that Moore's Law is still alive. With further research in finite element modeling techniques and solution procedures coupled with advances in high performance computing software and hardware systems, the future for running full-vehicle simulations for vehicle dynamics and durability which incorporate elastodynamics tire structures is promising.

Bibliography

[1] Genta, G., and Morello, L., eds., 2009. *The Automotive Chassis Vol. 1: Components Design*. Springer Netherlands, Netherlands, Chap. 2.9, pp. 125–126.

[2] Heeps, G., 2015. Another Fine Mesh. Online artical in the digital magazine: www.tiretechnologyinternational.com, November.

[3] Committee, V. D. S., 2008. "Vehicle Dynamics Terminology". In SAE Standards, SAE International.

[4] Pacejka, H. B., 2012. *Tire and Vehicle Dynamics,third edition*. Butterworth–Heinemann, Oxford, UK.

[5] Hüsemann, T., and Wőhrmann, M., 2010. "The Impact of Tire Measurement Data on Tire Modeling and Vehicle Dynamics Analysis". *Tire Science and Technology,* **38**(2), pp. 155–180.

[6] Gipser, M., 2005. "FTire: A Physically Based Application-Oriented Tyre Model

for Use with Detailed MBS and Finite-element Suspension Models". *Vehicle System Dynamics,* **43**(1), pp. 76–91.

[7] Gipser, and Hofmann, 2017. *FTire - Flexible Structure Tire Model*, latest ed. Cosin Scientific Software, GERMANY. See also URL `http://www.cosin.eu/wp-content/uploads/ftire_model.pdf`.

[8] Gipser, and Hofmann, 2017. *FTire Parameterization*, latest ed. Cosin Scientific Software, GERMANY. See also URL `http://www.cosin.eu/wp-content/uploads/ftire_param.pdf`.

[9] Oertel, C., and Fandre, A., 1999. "Ride comfort simulations and steps towards life time calculations: RMOD-K tyre model and ADAMS". In Proceedings of the International ADAMS Users Conference 1999, ADAMS.

[10] Oertel, C., and Fandre, A., 2009. "Tire Model RMOD-K 7 and Misuse Load Cases". In SAE Technical Paper, SAE International.

[11] Oertel, C., 2011. *RMOD-K Formula Documentation*, latest ed. RMOD-K, GERMANY. See also URL `http://www.rmod-k.com/formula`.

[12] Pearson, M., Blanco-Hague, O., and Pawlowski, R., 2016. "TameTire: Introduction to the Model". *Tire Science and Technology,* **44**(2), pp. 102–119.

[13] IPG Automotive, 2014. *TameTire Powered by*

Michelin. Model Interface, latest ed. See also URL `http://ipg.de/simulationsolutions/tametire/model-interface/`.

[14] Bartolozzi, G., Danti, M., Nierop, G., and Camia, A., 2015. "Simplified FE Modeling of Rolling Tires for the Simulation of Dynamic Forces at Hub Level". In SAE Technical Paper, SAE International.

[15] ESTECO, 2014. *User Manual*, 2014 ed. ITALY. See also URL `http://www.esteco.com/modefrontier`.

[16] Olatunbosun, O. A., and Bolarinwa, O., 2004. "FE Simulation of the Effect of Tire Design Parameters on Lateral Forces and Moments". *Tire Science and Technology,* **32**(3), pp. 146–163.

[17] Hall, W., Mottram, J. T., and Jones, R. P., 2004. "Tire Modeling Methodology with the Explicit Finite Element Code LS-DYNA". *Tire Science and Technology,* **32**(4), pp. 236–261.

[18] Li, Z., Li, Z. R., and Xia, Y. M., 2012. "An Implicit to Explicit FEA Solving of Tire F&M with Detailed Tread Blocks". *Tire Science and Technology,* **40**(2), pp. 83–107.

[19] Surendranath, H., 2014. "Effectiveness of Tetrahedral Finite Elements in Modeling Tread Patterns for Rolling Simulations". *Tire Science and Technology,* **42**(2), pp. 101–114.

[20] Kao, B. G., and Muthukrishnan, M., 1997. "Tire Transient Analysis with an Explicit Finite Element Program". *Tire Science and Technology,* **25**(4), pp. 230–244.

[21] Olatunbosun, O. A., and Burke, A. M., 2002. "Finite Element Modeling of Rotating Tires in the Time Domain". *Tire Science and Technology,* **30**(1), pp. 19–33.

[22] Gall, R., Tabaddor, F., Robbins, D., Majors, P., Sheperd, W., and Johnson, S., 1995. "Some Notes on the Finite Element Analysis of Tires". *Tire Science and Technology,* **23**(3), pp. 175–188.

[23] Iwasaki, N., Hayashi, K., and Richard, S., 2004. Method of making finite element tire model, Feb. 17. US Patent 6,691,566.

[24] Koishi, M., Kabe, K., and Shiratori, M., 1998. "Tire Cornering Simulation Using an Explicit Finite Element Analysis Code". *Tire Science and Technology,* **26**(2), pp. 109–119.

[25] Adkins, J. E., and Rivlin, R. S., 1955. "Large Elastic Deformations of Isotropic Materials X. Reinforcement by Inextensible Cords". *Philosophical Transactions of the Royal Society of London A: Mathematical, Physical and Engineering Sciences,* **248**(944), pp. 201–223.

[26] Pósfalvi, H., 1976. "On the Mechanical Behavior of the Orthotropic Cord–Rubber Composite". *Tire Science and Technology,* **4**(4), pp. 219–232.

[27] P. Helnwein and C.H. Liu and G. Meschke and H.A. Mang, 1993. "A new 3-D finite element model for cord-reinforced rubber composites–Application to analysis of automobile tires". *Finite Elements in Analysis and Design,* **14**(1), pp. 1 – 16.

[28] Clark, S. K., Gent, A. N., and Walter, J. D., eds., 2006. *The Pneumatic Tire.* U.S. Department of Transportation, NHTSA, Washington, D.C. USA, Chap. 4, pp. 105–155.

[29] Abaqus, 2013. *Abaqus Example Problems Guide, section1.1.15*, Abaqus 6.13 ed. Dassault Systèmes Simulia Corp, Providence, RI, USA.

[30] Abaqus, 2013. *Abaqus Analysis User's Guide, Section36*, Abaqus 6.13 ed. Dassault Systèmes Simulia Corp, Providence, RI, USA.

[31] Clark, S. K., ed., 1971. *Mechanics of Pneumatic Tires (NBS MONOGRAPH 122).* National Bureau of Standards, Washington, D.C. USA, Chap. 7, pp. 604–605.

[32] Clark, S. K., ed., 1971. *Mechanics of Pneumatic Tires (NBS MONOGRAPH 122).* National Bureau of Standards, Washington, D.C. USA, Chap. 7, pp. 581–582.

[33] Bergstrőm, J., and Boyce, M., 1998. "Constitutive modeling of the large strain

time-dependent behavior of elastomers". *Journal of the Mechanics and Physics of Solids,* **46**(5), pp. 931 – 954.

[34] Dorfmann, A., and Ogden, R. W., 2004. "A constitutive model for the Mullins effect with permanent set in particle-reinforced rubber". *International Journal of Solids and Structures,* **41**(7), pp. 1855–1878.

[35] Treloar, L. R. G., Hopkins, H. G., Rivlin, R. S., and Ball, J. M., 1976. "The Mechanics of Rubber Elasticity [and Discussions]". *Proceedings of the Royal Society of London. Series A, Mathematical and Physical Sciences,* **351**(1666), pp. 301–330.

[36] O.H.Yeoh, 1993. "Some Forms of the Strain Energy Function for Rubber". *Rubber Chemistry and Technology,* **66**(5), pp. 754–771.

[37] Purdy, J. F., ed., 1963. *Mathematics Underlying the Design of Pneumatic Tires.* Edwards Brothers, Ann Arbor, Michigan, USA, Chap. 1, pp. 10–22.

[38] Clark, S. K., ed., 1971. *Mechanics of Pneumatic Tires (NBS MONOGRAPH 122).* National Bureau of Standards, Washington, D.C. USA, Chap. 4, pp. 406–420.

[39] Chae, S., 2006. "Nonlinear Finite Element Modeling and Analysis Of A Truck Tire". PhD Thesis, Pennsylvania State University, State College, PA, August.

[40] Oden, J., and Lin, T., 1986. "On the general rolling contact problem for finite

deformations of a viscoelastic cylinder". *Computer Methods in Applied Mechanics and Engineering,* **57**(3), pp. 297 – 367.

[41] Abaqus, 2011. *An Integrated Approach for Transient Rolling of Tires*, Abaqus Technology Brief-January ed. Dassault Systèmes Simulia Corp.

Appendix A

Modeling Techniques for Transient Response

The Lagrangian description has to be adopted for the formulation of transient rolling. Direct integration of the system must be used when a nonlinear dynamic problem is involved. The implicit direct integration solver is provided in Abaqus/Standard; and the explicit direct integration solver is provided in Abaqus/Explicit. There is no strict rule to force users to choose an implicit or explicit solver; However, if the model involves severe nonlinearity and large number of degrees-of-freedom, the explicit solver is commonly used. The choice of implicit and explicit solvers is briefly discussed in section A.1.

The cleat test data is usually required to validate the model's damping behavior for transient response of a rolling tire. However, no experimental data is available due to the lack of test facilities to carry out transient tests in Virginia Tech. This research is not going to validate the transient response of the model. Instead, the focus is only put on the modeling techniques required for the future full-vehicle simulation. It is noted that the simulation of one tire is much different from of four tires in Abaqus because of the constraint by Abaqus solvers. The alternative simulation method which can handle four rolling tires simultaneously needs to be investigated, which is briefly discussed in section A.2.

A.1 Choose the Solver for Dynamic Rolling Problem

A.1.1 Dynamic Rolling using Implicit Solver

The implicit dynamic solver in Abaqus is powerful to study the responses involving nonlinearity, contact, and moderate energy dissipation. The direct-integration dynamic implicit solver in Abaqus offers several choices of the implicit operators for integration of the equations of motion, which includes the Hilber-Hughes-Taylor time integration operator and the backward Euler operator. The choosing of time integration operators depends on the application type. Typical dynamic applications fall into three categories.

- Transient fidelity applications which require minimal energy dissipation.
- Moderate dissipation applications which encompass a more general range of dynamic.
- Quasi-static applications are primarily interested in determining a final static response

The dynamic rolling tire simulation belongs to the second category. The backward Euler operator is used for special applications belonging to the third category and not suitable for our dynamic rolling simulation. So the Hilber-Hughes-Taylor time integration, which is an extension of the Newmark $\beta-$method, should be adopted. Numerical parameters associated with the Hilber-Hughes-Taylor operator are tuned differently for transient fidelity and moderate dissipation applications. In most cases, users are only required to specify the application type to the dynamic implicit solver, and Abaqus will assign values accordingly to the operator parameters; however, advanced users have the freedom to control the operator values directly.

The Hilber-Hughes-Taylor and backward Euler time integration operators are implicit which means that the operator matrix must be inverted and a set of nonlinear dynamic equilibrium equations must be solved simultaneously at each time increment. For a nonlinear problem, each increment typically requires several iterations to obtain a solution within the prescribed tolerances for a . The principal advantage of these operators is that they are unconditionally stable for linear systems. The time integration scheme is said to be stable if numerical errors do not grow unbounded with the time marching. The disadvantage is the set of equations has to be solved iteratively using Newton's method, therefore computationally expensive. If a model contains highly discontinuous processes, such as contact and frictional sliding, a large number of iterations may be required or even the solution can NOT converge; the equilibrium conditions are not satisfied at the current increment.

A.1.2 Dynamic Rolling using Explicit Solver

The explicit dynamic solver is based upon the implementation of an explicit integration rule together with the use of diagonal ("lumped") element mass matrices. The equations of motion for the body are integrated using the explicit central-difference integration rule. Assuming there are no damping forces, at the beginning of the $(n+1)^{th}$ increment the program tries to solve for dynamic equilibrium:

$$\mathbf{M}\ddot{\mathbf{u}}_{n+1} + \mathbf{K}\mathbf{u}_{n+1} = \mathbf{F}^{ext}_{n+1} \tag{A.1}$$

where $\mathbf{M}$ is the mass matrix, $\mathbf{K}$ is the stiffness matrix, and $\mathbf{u}$ is the nodal displacement vector. $\ddot{\mathbf{u}}$ becomes the nodal acceleration. $\mathbf{F}^{ext}$ is the external applied force vector. The subscript $(n+1)$ means the quantities being evaluated at the $(n+1)^{th}$ time increment. The velocity at the $(n+1)^{th}$ increment, $\dot{\mathbf{u}}_{n+1}$, can be calculated by adding the change in velocity, which assumes that the acceleration is constant through the time interval Δt to the velocity at the n^{th} increment $\dot{\mathbf{u}}_n$,

$$\dot{\mathbf{u}}_{n+1} = \dot{\mathbf{u}}_n + \Delta t \frac{\ddot{\mathbf{u}}_n + \ddot{\mathbf{u}}_{n+1}}{2} \tag{A.2}$$

The velocity is then integrated through time and added to the displacement at the n^{th} increment to determine the displacement at the $(n+1)^{th}$ increment,

$$\mathbf{u}_{n+1} = \mathbf{u}_n + \Delta t\dot{\mathbf{u}}_n + \frac{(\Delta t)^2}{2}(\ddot{\mathbf{u}}_n + \ddot{\mathbf{u}}_{n+1}) \tag{A.3}$$

Substitute Eqn.A.2 and Eqn.A.3 back into the dynamic equilibrium equation Eqn.A.1 then solve $\ddot{\mathbf{u}}_{n+1}$

$$\ddot{\mathbf{u}}_{n+1} = \mathbf{M}^{-1}(\mathbf{F}^{ext}_{n+1} - \mathbf{K}\mathbf{u}_{n+1}) \tag{A.4}$$

The key to the computational efficiency of the explicit solver is using diagonal element mass matrices to make the inverse of the mass matrix easily.

The central-difference operator is conditionally stable. The stability limit for the operator (with no damping) is constrained by the highest frequency ω_{max} of the system as (Courant–Friedrichs–Lewy condition)

$$\Delta t \leq \frac{2}{\omega_{max}} \tag{A.5}$$

The physical interpretation of Δt in Eqn.A.5 is the time required for a stress wave to cross the smallest element dimension in the model. Thus, the time increment in an explicit dynamic analysis can be very short if the mesh contains small elements or if the stress wave speed in the material is very high. The explicit solver allows the solution to proceed without iterations and without requiring tangential stiffness matrices to be formed comparing to the implicit procedure. Since the state of the

Table A.1: Tire simulation steps and corresponding preferred solvers used

Step	Solver	Note
Mounting	Abaqus/Standard, General Static	
Inflation	Abaqus/Standard, General Static	The analysis in Abaqus/Standard
Load-deflection	Abaqus/Standard, General Static	cannot be followed by the analysis
Steady-state rolling	Abaqus/Standard, Steady-State Transport	in Abaqus/Explicit directly.
Dynamic rolling	Abaqus/Standard, Dynamic Implicit	Special techniques required.
	Abaqus/Explicit, Dynamic Explicit	

model is advanced explicitly, iterations and tolerances are not required. But the very small time increment and no numerical accuracy check are drawbacks.

It is noted that in Abaqus/explicit some formulations of element and treatment of contact differs from in Abaqus/implicit, which needs a special attention to the compatibility.

A.1.3 Summary of using Implicit and Explicit solver

In implicit dynamic analysis the integration operator matrix must be inverted and a set of nonlinear equilibrium equations must be solved at each time increment. In explicit dynamic analysis, the global mass and stiffness matrices do not need to be reformed and inverted because the use of diagonal mass matrices, which is the key to improve the computational efficiency; displacements and velocities are calculated in terms of quantities that are known at the beginning of an increment in the explicit procedure. In addition, the Abaqus explicit solver does not do iteration to obtain the solution in an increment but the Abaqus implicit solver does. Therefore, each increment in a explicit integration is relatively inexpensive compared to the increment in an implicit integration. The size of the time increment causes conditional stability for the explicit solver; whereas the implicit solver is unconditionally stable. The time increment size of the explicit procedure depends solely on the highest natural frequencies of the model (Courant–Friedrichs–Lewy condition) and is independent of the loading. The time increment size of the implicit procedure is generally governed by the accuracy and convergence of solutions.

A.2 Result Transfer from Implicit to Explicit Solver

The necessity of employing the result transfer technique in Abaqus is discussed first. For dynamic rolling analysis of a finite element tire model, a series of simulations

such as mounting, inflation, load-deflection and dynamic rolling steps need to be executed in sequence. Some steps are suitable for solving by Abaqus/Standard; while the other steps are preferably solved by Abaqus/Explicit. Table A.1 summaries the preferred solver for each simulation step. However, an analysis from Abaqus/Standard cannot be directly followed by an analysis from Abaqus/Explicit and vice versa, because the formulation of element type, contact, and constraints are different. If one insisted on using only one type of solver through all simulation steps for ease, e.g. using the implicit dynamic solver for inflation and load-deflection steps, the solutions cost exceptional long time for static response. It urges the emerging of a technique to establish connections among sorts of analysis. The "result transfer" technique in Abaqus is a solution to the addressed issue. It provides the capability to import a deformed mesh and its associated material state from Abaqus/Standard to Abaqus/Explicit. In addition, the "result transfer" technique has to be accompanied by the "restart" technique to changing the analysis from one kind to another kind.

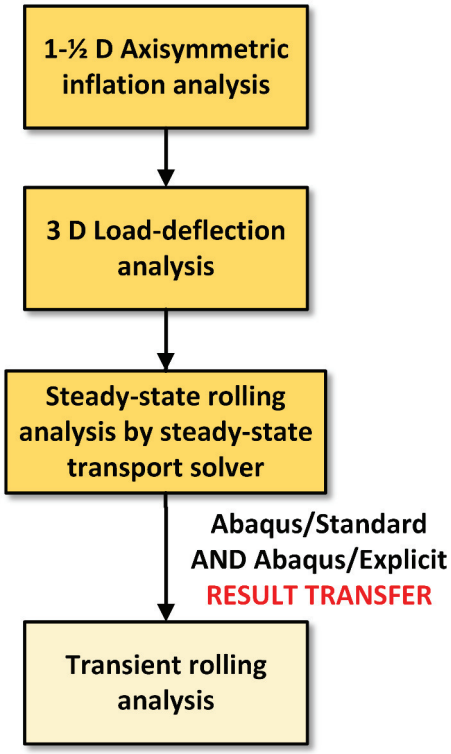

Figure A.1: The work-flow of modeling ONE dynamic rolling tire for transient response in Abaqus. The result transfer technique from Abaqus/Standard to Abaqus/Explicit has to be applied. The first three modeling steps are the same as Fig. 6.6

If only one rolling tire is considered, it is a good choice to import the steady-state rolling solution as an initial state into Abaqus/Explicit for further transient analysis

Table A.2: Simulation scheme to exercise the implicit/explicit solver and result transfer technique of Abaqus

Step	Description	Solver	Note
Mounting & Inflation	inflation pressure 10 psi	Abaqus/Standard, General Static	
Load-deflection	vertical load 150 lbf	Abaqus/Standard, General Static	
Straightline rolling,	t=0 s to t=1 s; accelerate from ω=0 to ω=6 rad/s	Abaqus/Standard, Dynamic Implicit	
road-section 1	t=1 s to t=3 s; rolling at constant speed ω=6 rad/s		
Straightline rolling	t=3 s to t=5 s; rolling at constant speed ω=6 rad/s	Abaqus/Standard, Dynamic Implicit	restart technique
road-section 2			applied
		Abaqus/Explicit, Dynamic Explicit	results import&transfer
			technique applied

as the work-flow illustrated in Fig. A.1. The cost to obtain a steady-state rolling simulation in Abaqus/Explicit increases with rolling speed, whereas the cost of using the steady-state transport solver is independent of the magnitude of the rolling speed. The result transfer technique has been widely used in tire industry [41]. However, the steady-state transport solver can only handle one deformable body to be analyzed. The limitation prevents the use of steady-state transport analysis for a full-vehicle simulation because four tires are going to be analyzed simultaneously. Not to mention each tire is in a different steady-state rolling state when a vehicle is in steady-state cornering.

For a full-vehicle (with four tires) dynamic simulation, the work-flow proposed in Fig. A.1 does not work any more. The modeling procedure should avoid the reliance on the steady-state transport solver. The steady-state response of the suspension and chassis can not be obtained through the steady-state transport solver either. Therefore, the full-vehicle simulation has to rely only on the static and dynamic (implicit or explicit) solvers. A possible modeling procedure, which does not use the steady-state transport solver, is demonstrated through an example of one tire in straight-line dynamic rolling for ease instead of running a full-vehicle simulation. The example is to show how the result transfer and restart technique can be applied. The proposed procedure can be generalized to the full-vehicle simulation. In the example, the simulation scheme is designed in Table A.2. The tire inflation and load-deflection process(the first and second simulation steps in Table. A.2) are still solved by the static-general solver. The dynamic rolling analysis requires to import and transfer the static results from Abaqus/Standard into Abaqus/Explicit. The tire dynamic rolling simulation can use implicit or explicit solver depending on the specific operational condition of the tire and vehicle. For example, if a constant acceleration of a vehicle is studied, both implicit and explicit solver are good for the problem; while if a tire cleat test is simulated, the explicit solver is a better choice because severe nonlinearity and damping involved. In this example, the tire model is then set to roll straightly along two consecutive road-sections using both implicit and explicit dynamic solvers.

- In the first road-section (the third simulation step in Table. A.2), the tire

accelerated from stationary to the revolution speed, $\omega = 6rad/s$ in one second then kept at a constant rolling for two more seconds. The dynamic rolling in the first road-section was solved by the dynamic implicit solver.

- In the second road-section(the fourth simulation step in Table. A.2), the tire continued rolling at the constant revolution speed $\omega = 6rad/s$ for extra two seconds. The dynamic implicit and explicit solver were both used to simulate the same process. The results obtained through different solvers were expected to be the same.

- When the implicit solver was employed during the second road-section to follow the simulation in the first road-section, the restart technique had to be used; When the explicit solver was employed during the second road-section to continue the simulation in the first road-section, the result import and transfer techniques became necessary.

The traveled distances shown in Fig. A.2 were checked for both solutions. The difference between the results obtained by the implicit and explicit solver was 0.1%. The contact pressure solved by the implicit solver and the explicit solver at the end

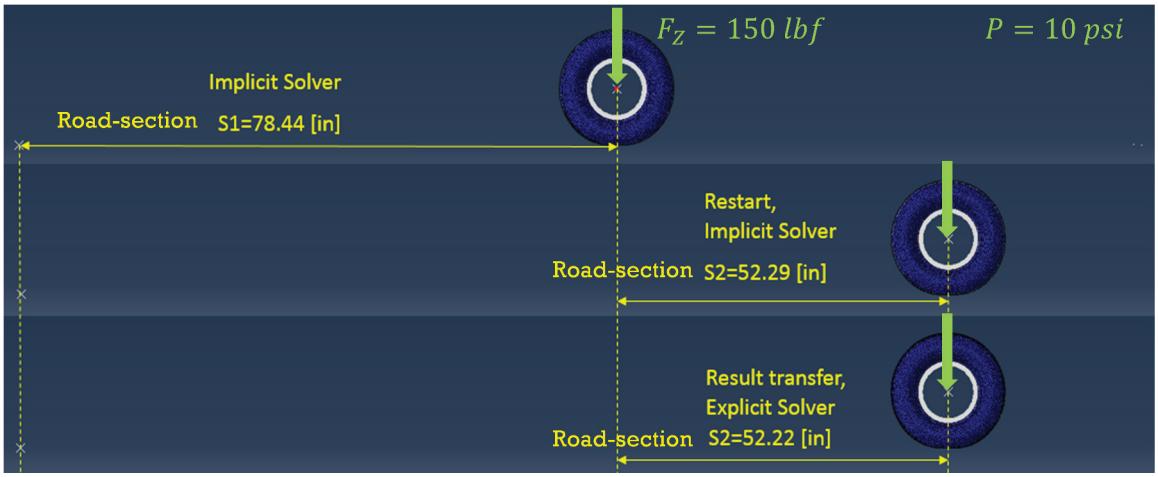

Figure A.2: Applying the import and result transfer techniques through a straight line dynamic rolling simulation; (side view)The traveled distance solved by the implicit and explicit solver are compared

of road-section $S2$ are further examined in Fig. A.3 (a) and (b). The contour plots show the similar distributions of the contact pressure and the similar contact area. The results demonstrated the effectiveness of using the results transfer technique and different type of solvers on solving a tire dynamic rolling problem.

The computing machine used for running the simulation was equipped with Intel® Core™i7-920 CPU and 24.0 GB RAM. The simulation environment was Abaqus 6.13-3, and four CPUs were used for running the simulation. It is noted that the total

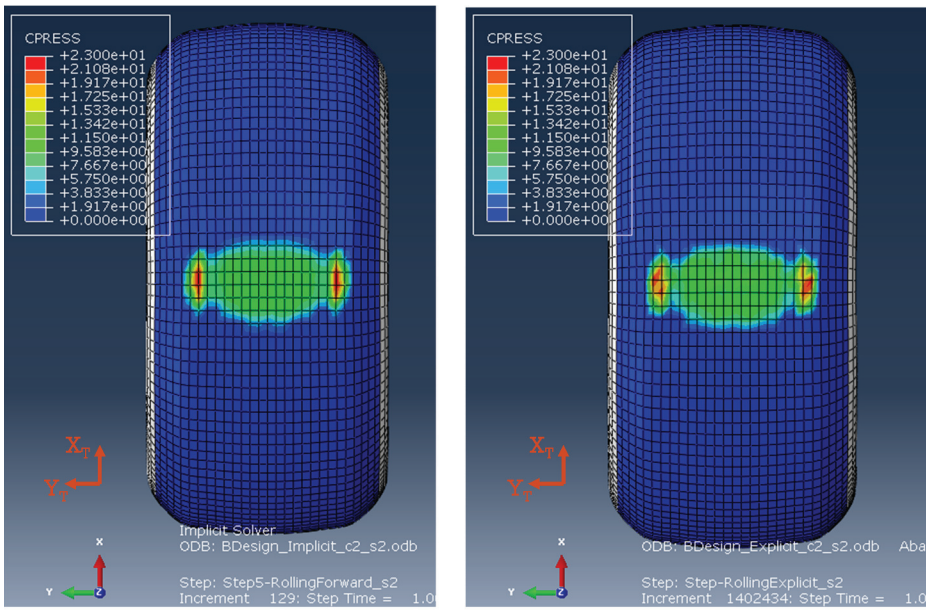

Figure A.3: Comparison of the contact pressure solved by the implicit solver (a) and the explicit (b) solver.

time increments were 129 for using the implicit solver, while the total increments were 1402434 for using the explicit solver. The explicit solver requires far larger increments than the implicit solver, but the cost per increment for the explicit solver is smaller than the implicit solver. These are important characteristics of the two solvers as summarized in Section A.1.3.